Geovisualization of Boreal Peatland Architecture in a Three Dimensional Hydrogeological Framework using Ground Penetrating Radar and LiDAR at Mariana Lakes, Alberta, Canada

by

William Shulba, III P.Geo.

G.Cert. Learning and Teaching in Higher Education, University of Victoria, 2015

B.Sc. Environmental Earth Sciences, University of Alberta, 2007

B.Sc. Geology, University of Alberta, 2006

A Thesis Submitted in Partial Fulfilment

of the Requirements for the Degree

MASTER OF SCIENCE

in Department of Geography

Geovisualization of Boreal Peatland Architecture in a Three Dimensional Hydrogeological Framework using Ground Penetrating Radar and LiDAR at Mariana Lakes, Alberta, Canada

by

William Shulba, III P.Geo.

G.Cert. Learning and Teaching in Higher Education, University of Victoria, 2015

B.Sc. Environmental Earth Sciences, University of Alberta, 2007

B.Sc. Geology, University of Alberta, 2006

Supervisory Committee

Dr. David E. Atkinson (Chair Department of Geography, University of Victoria)

Supervisor

Dr. Eva Kwoll (Department of Geography, University of Victoria)

Co-Supervisor

Abstract

Communicating science in three-dimensional (3D) multimedia is an immersive and interactive way to explore scientific processes (Signals and Communication Technology, 2019). Geovisualization is an emerging 3D multimedia method for visual analysis, synthesis, and presentation of geospatial, geologic, and geophysical data (MacEachren & Kraak, 2001). There is an identified need to develop scientific communication tools to further understand boreal peatland evolution, hydrogeology, ecology, and geochemistry (Bubier et al., 2003) since the International Union of Conservation of Nature asserts that peatlands are among the most valuable ecosystems on Earth, critical for preserving global biodiversity, providing drinking water, minimising flood risk, preventing wildfire, and mitigating climate change (Hama et al., 2000).

The intention of this thesis is to communicate a novel approach to geovisualize boreal peatland architecture using Light Detection and Ranging (LiDAR) and Ground Penetrating Radar (GPR). GPR and LiDAR have been used to create 3D subsurface geovisualizations for archaeology (Kenady et al., 2018; Schultz & Martin, 2011) and resource geology (Corradini et al., 2020; Koyan & Tronicke, 2020) although application to peatland hydrogeology is uncommon.

Point-source hydrogeological and geochemical data were integrated with 3D geological models to estimate carbon and nitrogen storage in an archetypal boreal peatland near Mariana Lakes, Alberta. Peatland geometry resembled a shallow lake basin with depths greatest in fens (>10 m) and thinnest in bogs (<2 m). Hydraulic conductivity was only a few meters per year and vertical groundwater movement was limited. Sequestered carbon and nutrients increased with depth. The average concentration of dissolved ammonium was 3 grams per cubic metre of peat (g/m^3), $5g/m^3$of Total Kjeldahl Nitrogen, $60g/m^3$ of dissolved organic carbon and $200g/m^3$ of dissolved inorganic carbon. Tritium detection from atmospheric atomic weapons radionuclide fallout revealed that in deeper anaerobic peat (catotelm), tritium was absent, signifying groundwater was older than 50 years and not mixed with meteoric waters. Fen catotelm channels are likely acting as gravity-driven hydraulic traps (Tóth, 1999).

Table of Contents

List of Tables

List of Figures

Dedication

To the Shulba family, without you I would not be

Acknowledgements

I acknowledge with respect the Lekwungen peoples on whose traditional territory the University of Victoria stands and the Songhees, Esquimalt and WSÁNEĆ peoples whose historical relationships with the land continue to this day. I acknowledge that Mariana Lakes is located within Treaty 8 Territory on the traditional lands of the Heart Lake First Nation, the Fort Chipewyan First Nation, and Kikino Métis - who for generations hunted, trapped, harvested, and fished extensively in the region to satisfy a range of subsistence, livelihood, nutritional, social, cultural, spiritual, and other needs. I am grateful for the stories shared with me by traditional Knowledge Keepers and Elders throughout my Masters of Science journey. I offer this thesis as an act of reconciliation to those who may benefit from conservation arising from this research.

Thank you to the faculty and administration staff of the Department of Geography who supported this research and for the opportunity to explore my passion for teaching as specialist instructor. My wholehearted appreciation to Dr. David Atkinson for accepting the challenge of my supervisor. Your patience and guidance steadily reassured me that the path from academic ashes to completing this thesis was not unsurmountable. Большое спасибо за вашу помощь!
I am thankful for the support and thesis review from co-supervisor Dr. Eva Kwoll, danke schön!
Thank you to external examiner Dr. Edwin Nissen from the School of Earth and Ocean Sciences.
Thank you to my colleagues and research leads of the Cumulative Environmental Management Association and Alberta Innovates Technology Futures at the Vancouver Island Technology Park for project funding and supporting resources provided throughout this research. Special thanks to Mikaela Cherry, Amy Vallarino, Caren Küsel, and Pacific Northwest Tree Stewards for data, technical advice, hope, and fieldwork adventures.

To my friends and family, I love you. I am forever indebted to my Mom, Dad, and aunt Betty Shulba for financial, emotional, ancestral, and editing support - I could not have done this without you. To my best friend Kikino Myster Shulba, thank you for reminding me to take walks and love life.

Epigraph

water…
the single pillar foundation of life.

1. INTRODUCTION

Peatlands occur in most climates on Earth, inhabiting approximately 400 million hectares, an estimated one-third of the world's wetlands (Silvius, 2007). 80% of peatlands are found in the boreal forest (Joosten & Clarke, 2002) and cover approximately 12% of the Canadian landscape (Halsey & Vitt, 2000). In Canada, boreal peatlands are geologically young landscape features initiated by the retreat of the continental Laurentide ice sheet during the Younger Dryas stadial in the Late Pleistocene (12900 to 11700 years before present). Sphagnum-dominated peatlands proliferated throughout the Holocene Epoch in the boreal (Gorham et al., 2007).

Peatlands encompass a family of wetland types, including bogs and fens, with a defining characteristic that primary biological production annually exceeds decomposition resulting in net accumulation of incompletely decomposed organic material (Wieder & Vitt, 2006). Peatlands rely on a consistent supply of water; where its geochemistry and hydraulics form the function of the flora and fauna that inhabit them. In the Clymo (1992) peat model, water table depth divides peat profile into a shallow oxic vadose zone (acrotelm) where aerobic decomposition occurs and a deeper anoxic phreatic zone (catotelm) where slower anaerobic decomposition occurs.

Long-term carbon storage is disproportionally higher in peatlands than any other ecosystem, ranging from 500-600 billion tonnes of organic carbon worldwide with half sequestered in the boreal (Gorham et al., 2012). When damaged, peatlands release stored organic carbon into the environment as carbon dioxide (CO_2), emitting approximately one-tenth of annual global anthropogenic CO_2 greenhouse gas emissions (Kurz et al., 2013). Annual sequestration of atmospheric CO_2 by peatlands is sensitive to hydrological-climatic changes (Tuittila et al., 2004). Sphagnum-dominated peatlands are efficient at storing water, sequestering carbon, and governing nutrient movement (Li & Vitt, 1997) through hydrogeological controls (Danielle et al., 2017).

The International Union of Conservation of Nature asserts that peatlands are among the most valuable ecosystems on Earth, critical for preserving global biodiversity, providing safe drinking water, minimising flood risk, contributing to food security, and addressing climate change (Hama et al., 2000). Due to the global significance of carbon storage in peatlands, countries are encouraged to include peatland protection and restoration in their international climate mitigation commitments including those of the United Nations Climate Change Paris Agreement (Minasny et al., 2019).

Alberta Environment and Sustainable Resource Development (AESRD) assessed boreal peatlands in the Athabasca Oil Sands Region (AOSR) as a significant carbon store that are highly sensitive to landscape change and acidic deposition from industrial activity (Alberta Environment and Parks, 2017). Peatland health in the AOSR is at the nexus of preserving wetland hydrological function and resource extraction (Volik et al., 2020). Industrial development of the AOSR is raising concerns over increased impact on boreal peatland ecosystems and plant communities from industrial nitrogen deposition (Gibson et al., 2015; Hyvönen et al., 2013; Kennedy et al., 2018; Philibert et al., 2003; Saari et al., 2013; Stuart et al., 2018; Vitt & Bhatti, 2012; Westbrook et al., 2006; Wieder et al., 2019). In response to this, the Cumulative Environmental Management Association (CEMA) funded a peatland assessment and critical nitrogen deposition study near Mariana Lakes in Alberta to understand ecological impacts from increasing atmospheric nitrogen deposition on the region (Wieder et al., 2019).

An important objective of peatland assessment is to gain insight into the three-dimensional (3D) form. Determining landscape architecture of peatlands contributes to foundational understanding of wetland type, subsurface geometry, water sources, hydrology, geochemical accumulation, and principles of superposition. 3D geovisualization inherently constrains surficial and subsurface geomorphological properties that contribute to uncertainty (Poggio et al., 2020). When extrapolated to geomorphological extents in 3D; spatial data coupled with subsurface data can correlate landscape units to subsurface stratigraphic units (Dallaire & Garneau, 2008).

In-situ geological, hydrological, and geochemical data is inherently difficult and costly to acquire in boreal peatlands. Peatland cores, drive-point piezometers, pressure transducers, test pits, boreholes, drilling, and water sampling require expensive remote field campaigns and can damage peatlands during collection (Stephenson et al., 2020). When available, leveraging these data types in a logical data framework for wetland analysis is highly valuable (Bayer et al., 2011). A need exists for less intrusive remote sensing methods to facilitate analysis of the extent, character, and composition of peatlands, such as light detection and ranging (LiDAR) technology (Grayson et al., 2012), synthetic aperture radar (Chasmer et al., 2020; Minasny et al., 2019), gamma-ray spectrometry (Gatis et al., 2019), and ground penetrating radar (GPR).

LiDAR is a remote-sensing technology that uses optical wavelengths to acquire detailed information about topography for use in terrain analysis (Gatziolis & Andersen, 2008). In a LiDAR system, short pulses of light energy are emitted and a sensor measures the return time to range or "echo-locate" a reflecting object or surface providing elevation information (Krasowski, 2019; Mossa et al., 2019). LiDAR is acquired from a variety of platforms including aircraft (Russell et al., 2020), unmanned aircraft (Chasmer et al., 2020), balloons (Kaifler et al., 2020), low-earth orbit satellites (Di Girolamo et al., 2018), and terrestrial stations. Terrestrial LiDAR is gaining popularity due to portability (Walker et al., 2013), reliability in forests (Russell et al., 2020), and resolution for determining microtopography to reveal ecological variations (Stovall et al., 2019).

GPR is a non-intrusive geophysical method based on propagation and reflection of high-frequency electromagnetic waves in the subsurface (Proulx-McInnis et al., 2013). GPR provides useful information of the depth of buried objects and subsurface structures. GPR has been used for decades to investigate peatland depth (Comas et al., 2005; Dallaire & Garneau, 2008; Proulx-McInnis et al., 2013), carbon storage (Comas et al., 2017), water storage capacity (Valois et al., 2020), impacts to oilfield pipeline construction (Jol & Smith, 1995), and geo-electrical properties for geophysical analysis (Theimer et al., 1994).

Basic 3D representations of peatlands have been limited to topographical visualizations (Poggio et al., 2020) and wetland delineation based on terrain (Maxa & Bolstad, 2009). Recently, GPR and LiDAR have been integrated to create 3D subsurface geovisualizations for archaeology (Kenady et al., 2018; Schultz & Martin, 2011) and subsurface geology (Corradini et al., 2020; Koyan & Tronicke, 2020), although application to peatlands in this way is uncommon.

The extent to which anthropogenic impacts influence wetlands depends on the wetland type as well as the type of influence (Volik et al., 2020). The inherent physical properties of peat regulate important controls on the water table configuration and overall wetland water balance that can provide resiliency or vulnerability to the ecosystem (Price et al., 2003). The intention of this research was to develop a novel approach of geovisualizing peatlands by using geological modelling software (*LeapFrogGeo*) using LiDAR, GPR, and hydrogeological data.

Science assists in predicting the natural world using rule-governed processes (National Academies of Sciences Engineering and Medicine, 2017) and 3D multimedia is an immersive and interactive method for scientific exploration using these rule-governed processes (Signals and Communication Technology, 2019). Geovisualization is an emerging 3D multimedia approach that provides theory, methods, and tools for visual exploration, analysis, synthesis, and presentation of geospatial, geologic, and geophysical data (MacEachren & Kraak, 2001). Geovisual environments stimulate thinking on the relationships of geospatial patterns using dynamic deliverables not bound by traditional techniques, rules, and well-worn paradigms (Andrienko et al., 2008; Jung, 2015; Kraak, 2003; Kubíček et al., 2019; Kwan, 2000; MacEachren & Kraak, 2001; Mitsova et al., 2013). The exponential growth of spatial and temporal geoscientific data is enriching the use of geovisualization tools in composite learning and scientific analysis (Andrienko et al., 2008). In response to advancements in high-resolution sensor systems and sophisticated geovisualization software, disciplines such as molecular biology (Joppe et al., 2020), optical astronomy (Hurtley, 2018), geomorphology (Johnson et al., 2015), and groundwater hydrology (Minasny et al., 2019) are claiming a "*High Resolution Revolution*" era.

The goals of this research were to integrate existing hydrological and geochemical data with geo-spatial data to determine volumetric amounts of stored carbon and nitrogen, as well as, improve upon early conceptualizations of peatland architecture in the boreal forest (Figure 1.1).

The main analytical objectives of this thesis were to:

i. integrate existing in-situ hydrological and geochemical data with geo-spatial data in a 3D hydrogeological framework,
ii. improve upon early conceptualizations of peatland architecture (Figure 1.1).
iii. investigate peatland groundwater hydrology with respect to tritium concentrations, and
iv. determine volumetric amounts of stored carbon and nitrogen.

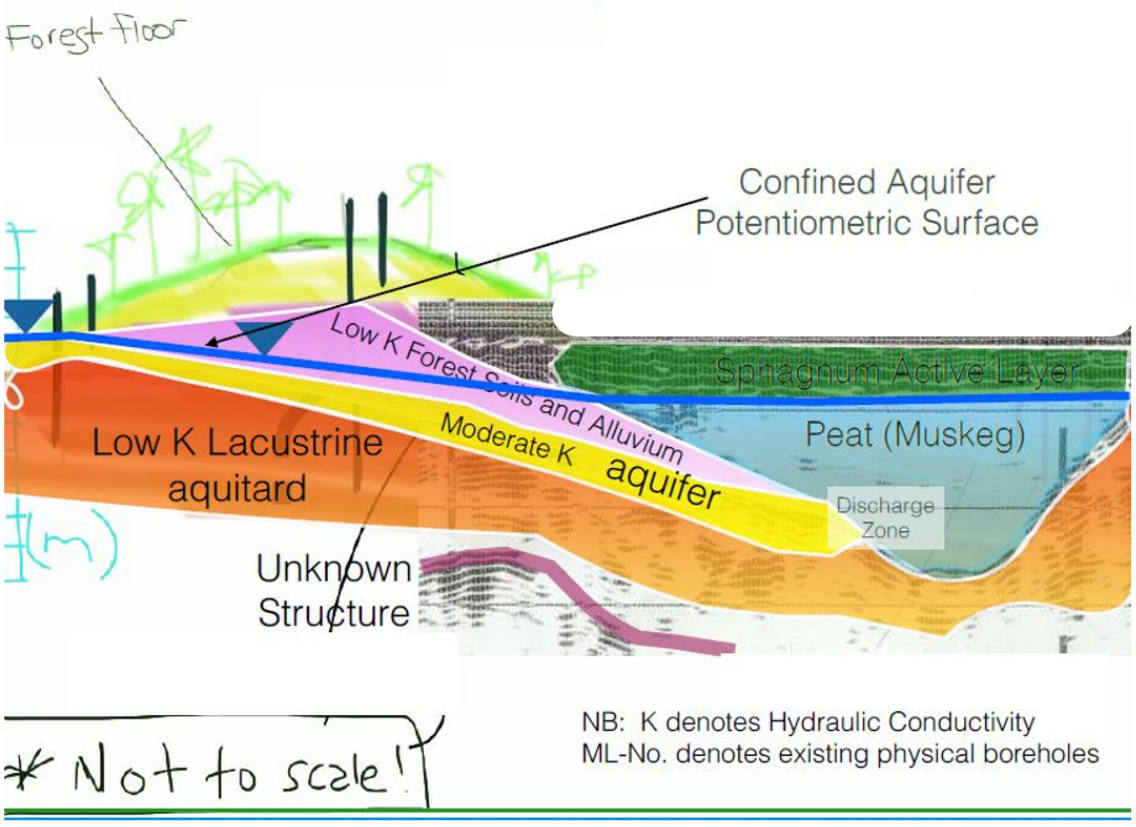

Figure 1.1 Early conceptualization of peatland architecture and hydrogeology at a peatland near Mariana Lakes in Alberta. This conceptualization was sketched using approximate peat depth from the advancement refusal during drive-point piezometer installation and a hypothetical peatland radargram.

2. RESEARCH SETTING

2.1 Geography

Canada's boreal forest is a mosaic of terrestrial ecoregions with complex ecotones dominated by coniferous forests and vast wetlands. The boreal forest region of Canada covers 5.8 million square kilometres (Cheskey et al., 2011), representing a quarter of global boreal ecosystems and 8% of the world's forests (Kurz et al., 2013). The boreal forest is a circumpolar, subarctic forest situated in higher northern latitudes that is bound to the north by tundra and to the south by temperate broad-leaved deciduous forest, steppe, or semi-desert (Johnston, 2017). Annual precipitation in the boreal forest nearly equals annual evapotranspiration (Devito et al., 1996). The word boreal is derived from Boreas (Βορεας), the Greek god of the north wind, envisioned as a bearded, curly-haired, winged god with a blistery temperament, a tunic for protection from the cold, and a spiral conch to herald the winds on command and beckon his daughter, Chione, the goddess of snow (Wieder & Vitt, 2006).

The regional terrain of the boreal is a landscape of uplands, wetlands, and low lying plains that developed since continental ice sheet retreat in the Late Wisconsin glaciation period (15,000 - 10,000 years before present, Attig et al., 1989). Peatlands and glacio-fluvial sediments blanket the landscape and are underlain by glacial till, lacustrine clay, and peri-glacial sands and gravels, known as "drift" deposits, that can be as thin as a few metres to over 100 metres thick (Birks et al., 2017; Dyke et al., 2019; Fenton et al., 2003; Paulen & McClenaghan, 2014).

2.2 Study Area

The study area is near Mariana Lakes, Alberta, Canada, located in the Athabasca Oilsands Region (AOSR, Figure 2.1) approximately 100 kilometres from the city of Fort McMurray. LiDAR acquisition defines the *study area* covering approximately 23 square kilometres (Figure 2.2). The area of detailed investigation is approximately 250 hectares, commonly referred to as *Mariana Fen,* which is adjacent to the east of Highway 63 and ASOR transportation and utilities corridor (Figure 2.3).

Figure 2.1 The study area is located in Western Canada in the northern region of the province of Alberta. The area is contained within the boreal forest and its distribution is displayed in green. The region has considerable amount of extractable bitumen in the Athabasca Deposit displayed in light brown.

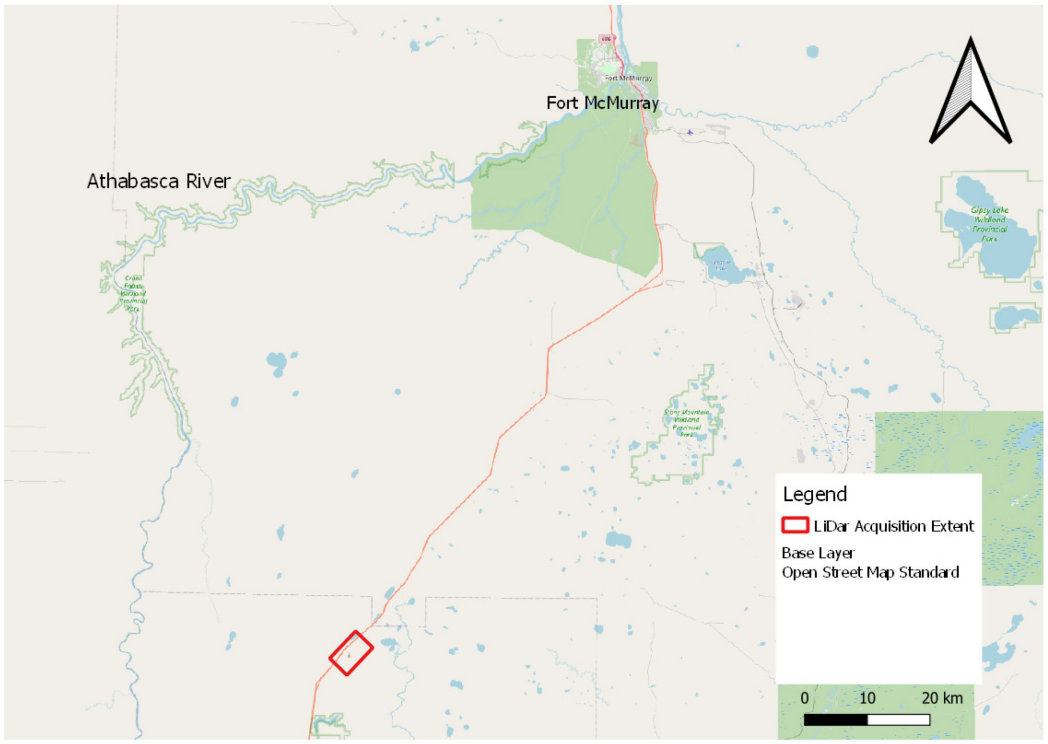

Figure 2.2 Regional View of the area whereby the study area is indicated in the red bounding box that delineates the LiDAR Acquisition Extent, approximately 100 km south of Fort McMurray.

Figure 2.3 Plan View of Study Area.

The study area is located at the southern extent of the Stoney Mountain Upland on a localized topographic highland referred to as the West Leismer Uplands ranging from 500 to 700 metres above mean sea level (mASL). The study area is likely underlain by the Lea Park geological formation on a regional bedrock high with a bedrock surface at approximately 100 metres below ground level (mBGL) at 600 mASL (Figure 2.4). Andraishek (2003) identified that glacial drift is regionally thinnest in the Athabasca River area of the Wabasca Lowlands and thickens over the Stoney Mountain Uplands. Glacial drift known as the "House River Till" blankets the region with marginal moraines and lacustrine deposits (Andraishek, 2003). The study area is in a localized thinning of glacial drift (<30 m thickness) in comparison to other areas of the Stoney Mountain Uplands where drift thicknesses can be greater than 100 m (Figure 2.5).

The region is a sphagnum moss-dominated peatland complex mainly containing bog and fen wetland types exhibiting minimal standing water during most of the wet season (Gibson et al., 2019). The upland areas are dominated by Jack pine (*pinus banksiana* Lamb.) with showings of black spruce (*picea mariana* (Mill.) Britton, Sterns & Poggenburg), white spruce (*picea glauca* (Moench) Voss), trembling aspen (*populus tremuloides* Michx.), balsam poplar (*populus balsamifera* L.), and white birch (*betula papyrifera* Marshall).

2.3 Climate

Alberta Sustainable Resource Development installed and operates several weather stations in the region. Bovine Creek Weather Station (3060756) is located in the House River Watershed at latitude 56.1100 and longitude -112.5500 at elevation 518.00 mASL. The reported annual precipitation is approximately 500 mm and an average monthly temperature of 0.9°C. Algar Weather Station (unknown number) is located at latitude 56.1608 and longitude -111.7198 at an elevation of 750 mASL that reported an annual precipitation average of 550 mm and an average monthly temperature of 0.8°C (Figure 2.6). This data was retrieved by Alberta Agriculture and Forestry, Alberta Climate Information Service (ACIS) at https://acis.alberta.ca (September, 2020).

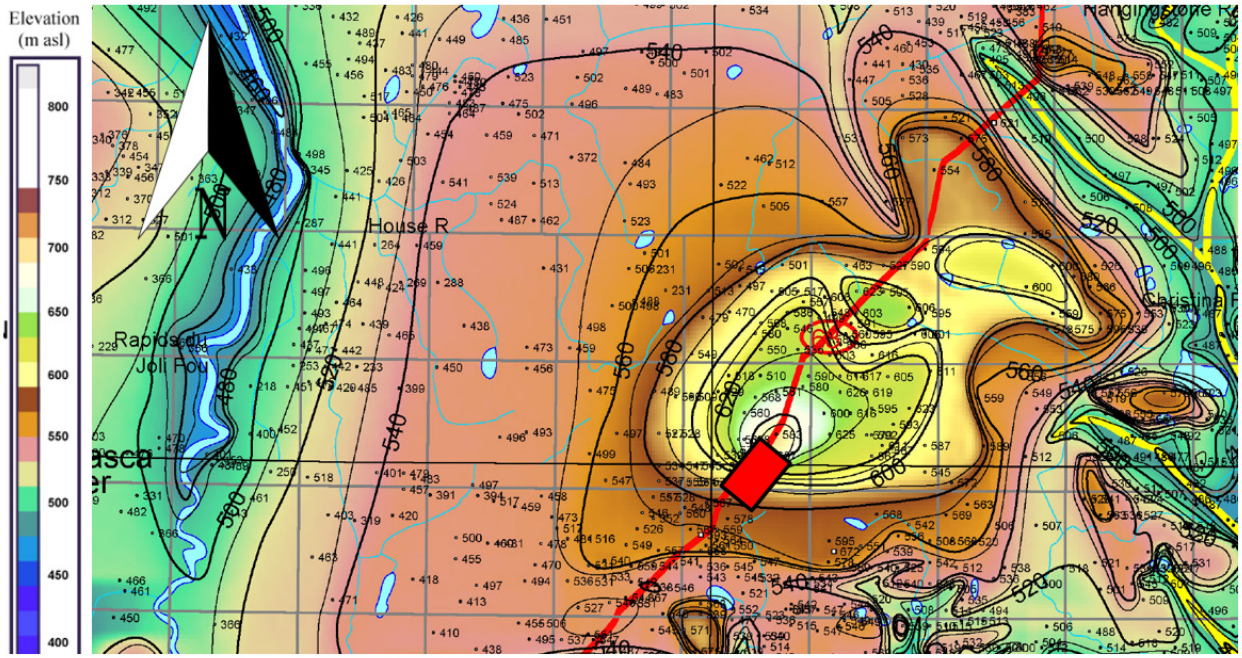

Figure 2.4 Regional bedrock surface elevation in the region showing study area in red bounding box (Andriashek, 2003).

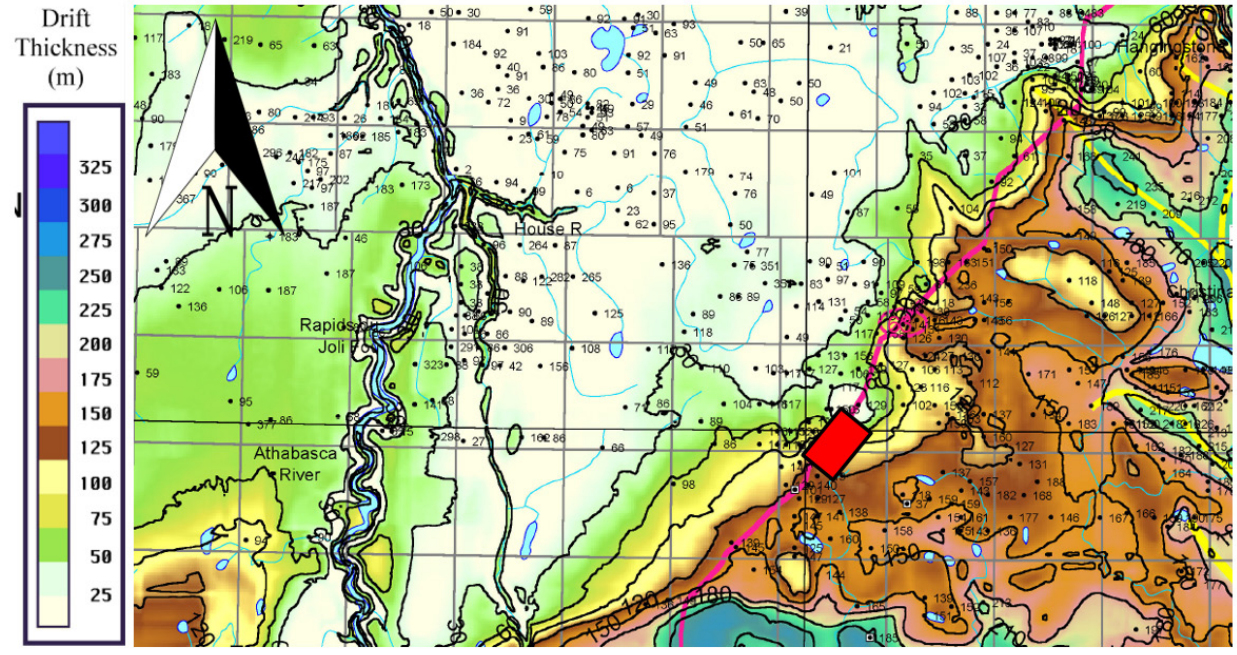

Figure 2.5 Contour map of glacial drift thickness showing the study area in red bounding box (Andriashek, 2003).

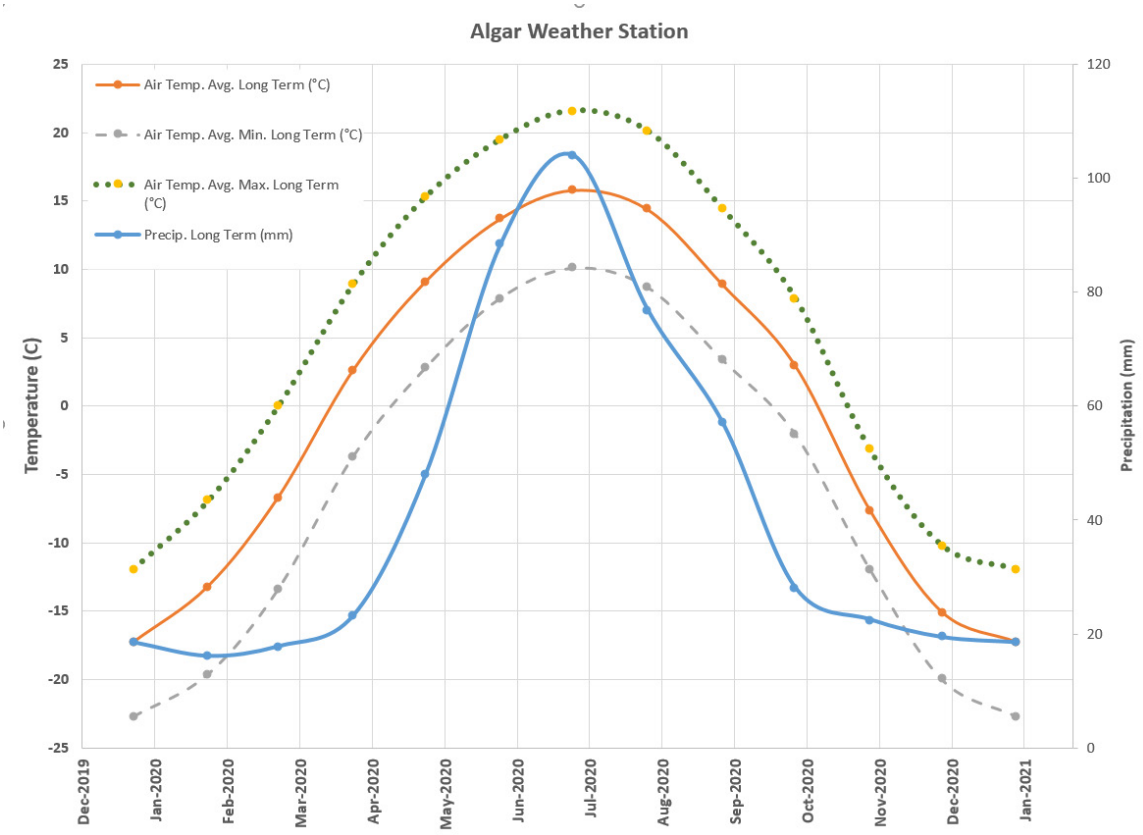

Figure 2.6 Monthly climate averages from Algar Weather Station from 2020.

2.4 Watershed Hydrology

Watersheds in Alberta are classified using the hydrologic unit code (HUC) system originally developed by the United States Geological Survey (USGS). The HUC is an alphanumeric coding methodology that uses four nested hierarchically structured drainage basin feature classes to determine successively smaller sub-watersheds that nest into larger watersheds (Seaber et al., 1987). The study area is in the headwaters of the House River Watershed (HUC 8 # 17050205, WSC 07CB) in the Athabasca River Middle Basin (HUC 4 #1705), part of the Great Slave River Watershed (Table 2.1, Figure 2.7). The House River Watershed is approximately 2800 km^2 (Figure 2.8). The House River hydrological station (08CB002) at Highway 63 has an average discharge volume of 5.58 m^3/s from 2000-2020. Smaller sub-watersheds with hydrologic unit code 10 (HUC 10) were not previously delineated for the region by Government of Alberta. Sub-watersheds were delineated for the study area using LiDAR-derived digital elevation model in System for Automated Geoscientific Analyses (SAGA) software (Figure 2.9).

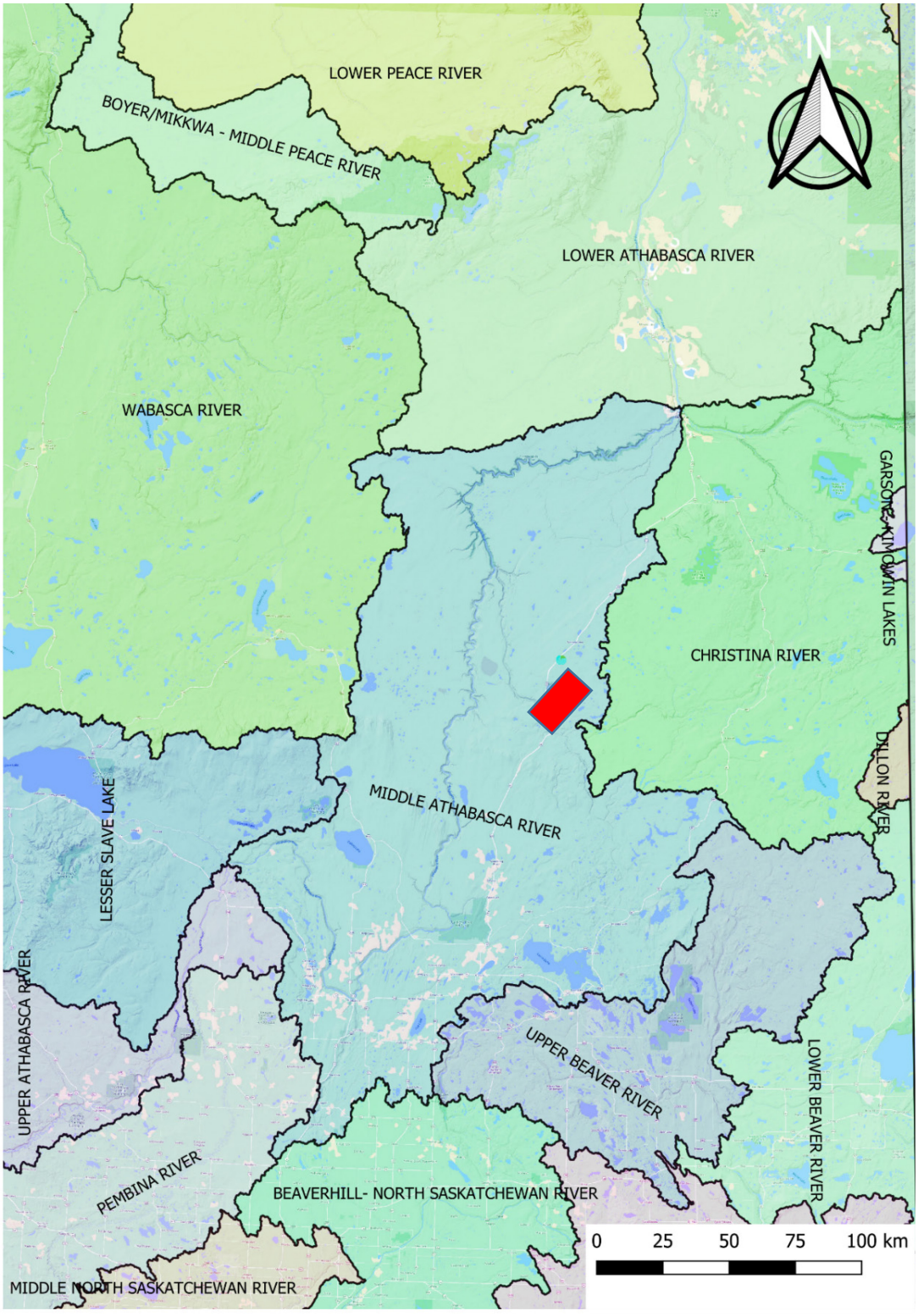

Figure 2.7 The Middle Athabasca River Watershed (Hydrologic Unit Code 06) delineated from data acquired from GeoDiscover Alberta. The study area is approximately labelled by the red box.

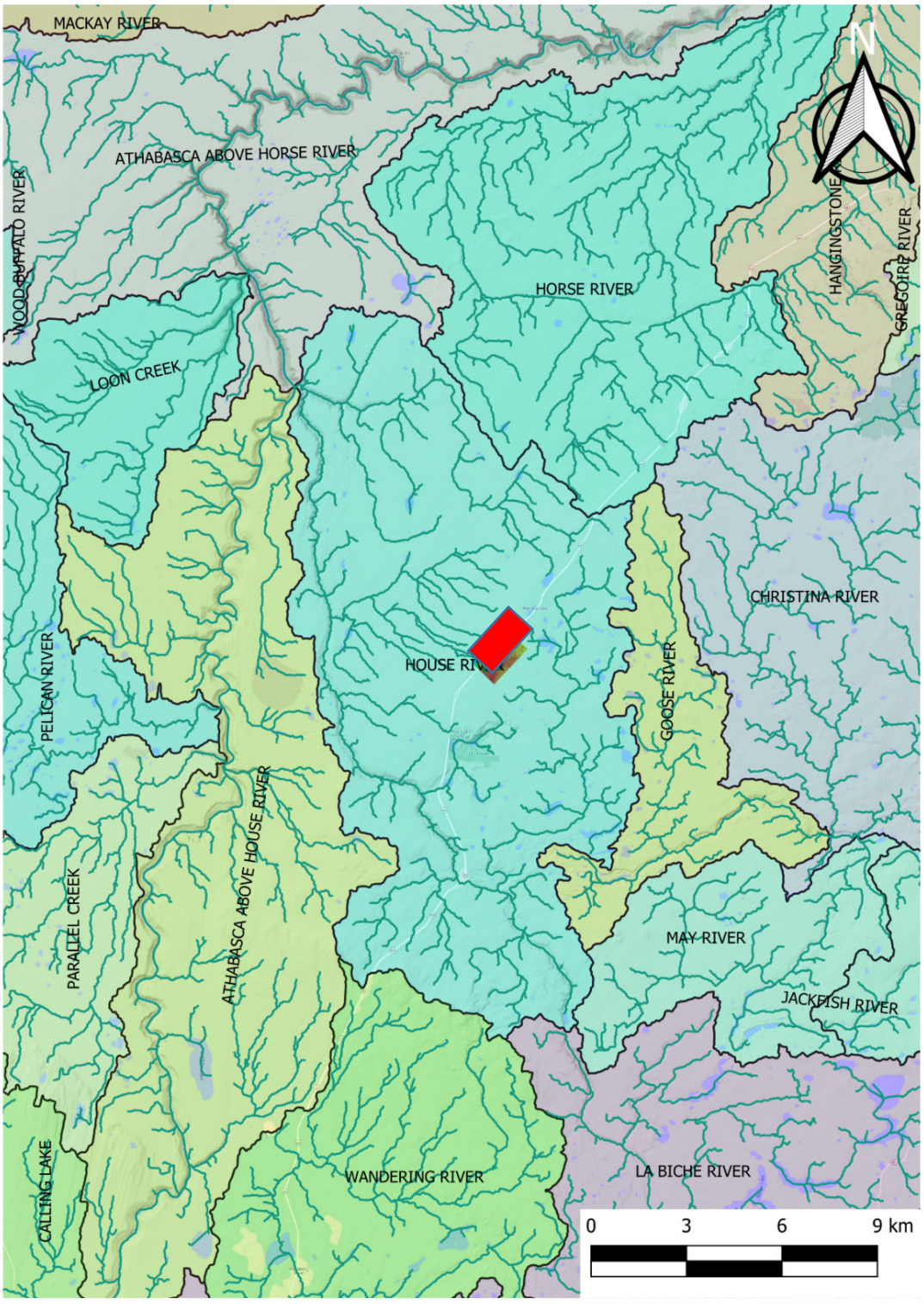

Figure 2.8 The House River Watershed (Hydrologic Unit Code 08) delineated from data acquired from GeoDiscover Alberta. The study area is approximately labelled by the red box.

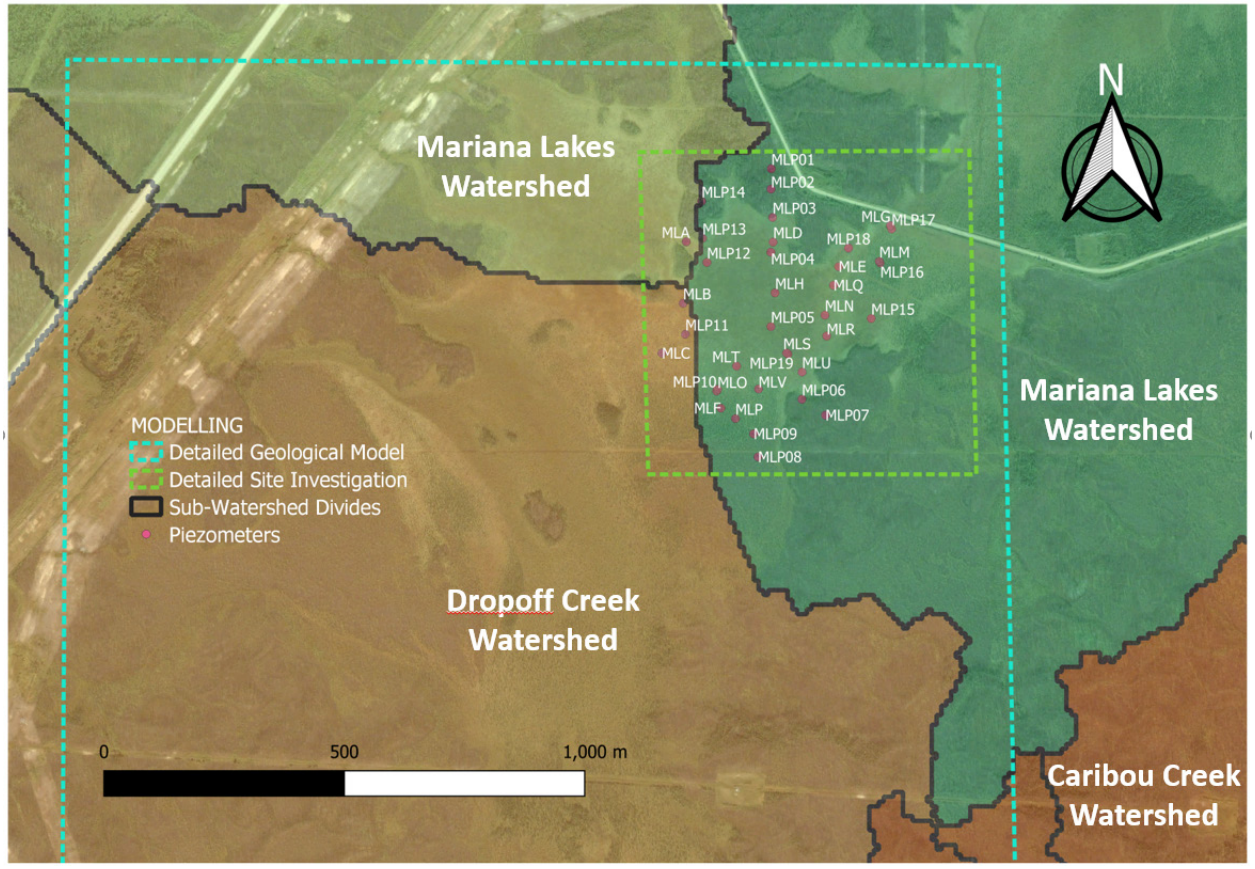

Figure 2.9 Sub Watersheds of within the study area delineated using the Wang Liu fill sinks module in System for Automated Geoscientific Analyses software package using LiDAR derived digital elevation models.

Table 2.1 Watersheds in the study region with associated Hydraulic Unit Code (HUC)

Hydrologic Unit Class	Hydrologic Unit Code	Name
HUC 2	17	Athabasca River Basin
HUC 4	1705	Middle Athabasca River
HUC 6	170502	Calling Lake – House River
HUC 8	17050205	House River

2.5 Peatland Ecohydrology

The Alberta Wetland Classification System (Alberta Environment and Sustainable Resource Development, 2015) states the major factor that differentiates bogs and fens in peatlands is water source. Bogs are ombrogenous and lentic wetlands that receive water almost exclusively from precipitation and maintain moisture levels through capillary action of sphagnum moss (Wieder & Vitt, 2006). Bogs are acidic environments because rainwater is typically acidic from interactions with carbon dioxide in the atmosphere creating weak carbonic acid (Danielopol & Griebler, 1918; Mitsch & Gosselink, 2015). Sphagnum moss dominated the bogs in area and comprised the majority of the surficial active layer (Figure 2.10). Fens are minerogenous and lotic as they receive water from a variety of sources including shallow and deep groundwater. Groundwater is characteristically alkaline; therefore, fens are likely less acidic than bogs within the same peatland complex (Bridgham et al., 1999). Although water table levels fluctuate throughout the seasons, peatlands typically have permanently saturated soils with sluggish rates of decomposition (Comas et al., 2005). Fens are groundwater dependant ecosystems where flora and fauna are vulnerable to hydrological changes from climatic and land-use impacts (Drexler et al., 2013).

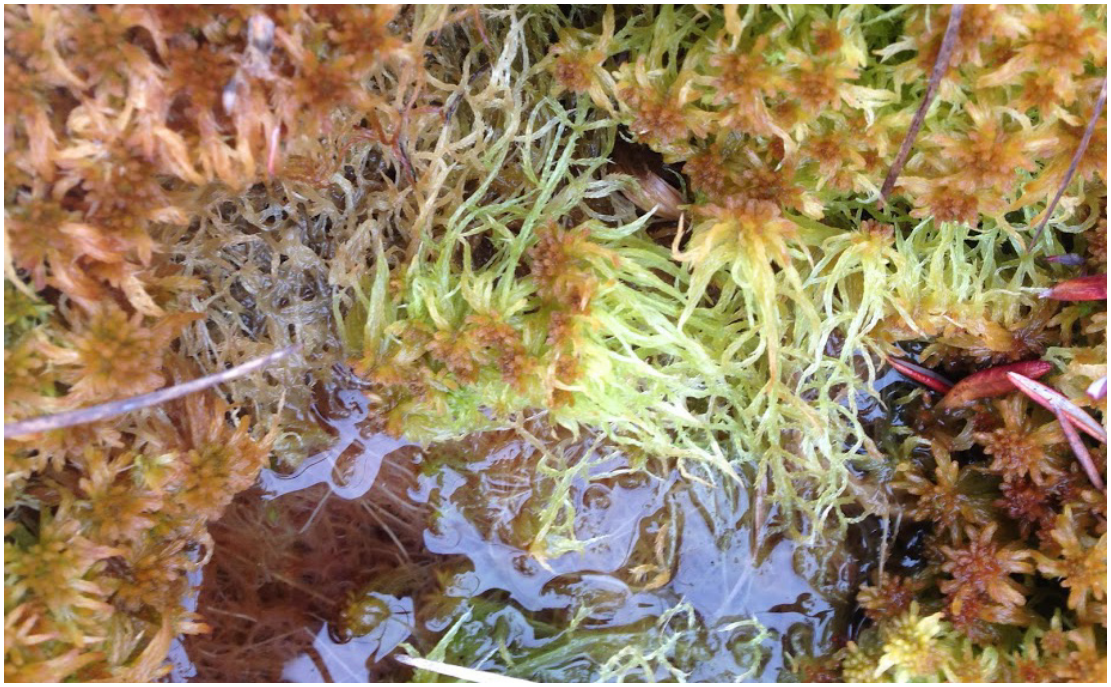

Figure 2.10 Sphagnum Moss at Well Location MLP-19, Photo by Wm.Shulba, Oct 2014

2.6 Regional Hydrogeology

The *Regional Geochemistry Study for the Southern Athabasca Oil Sands (SAOS) Area* (Birks et al., 2017) describes the regional hydrogeology and geochemistry of the study region. The area is generally mixed with glaciogenic waters and dominated regionally by bicarbonate-type waters (Birks et al., 2017; Gibson et al., 2015). Total dissolved solids increase to the southwest of the Wiau Channel and the Leismer Uplands. Considering Andriashek (2003) and other Alberta Geological Survey (AGS) mapping; it is likely that general flow direction of the regional hydrogeology is west-northwest in a radial flow shedding off the Stoney Mountain Uplands towards the Athabasca River area. The Leismer and Wiau buried channels are unique hydrogeological features that are comprised of quaternary sands and gravels of the Empress Formation that fill eroded bedrock channels. The thickest sediments are up to 70 m in the thalweg of the channel. The general flow of the channels is to the south down the thalweg in the Leismer Channel and to the west in the Wiau Channel (Figure 2.11).

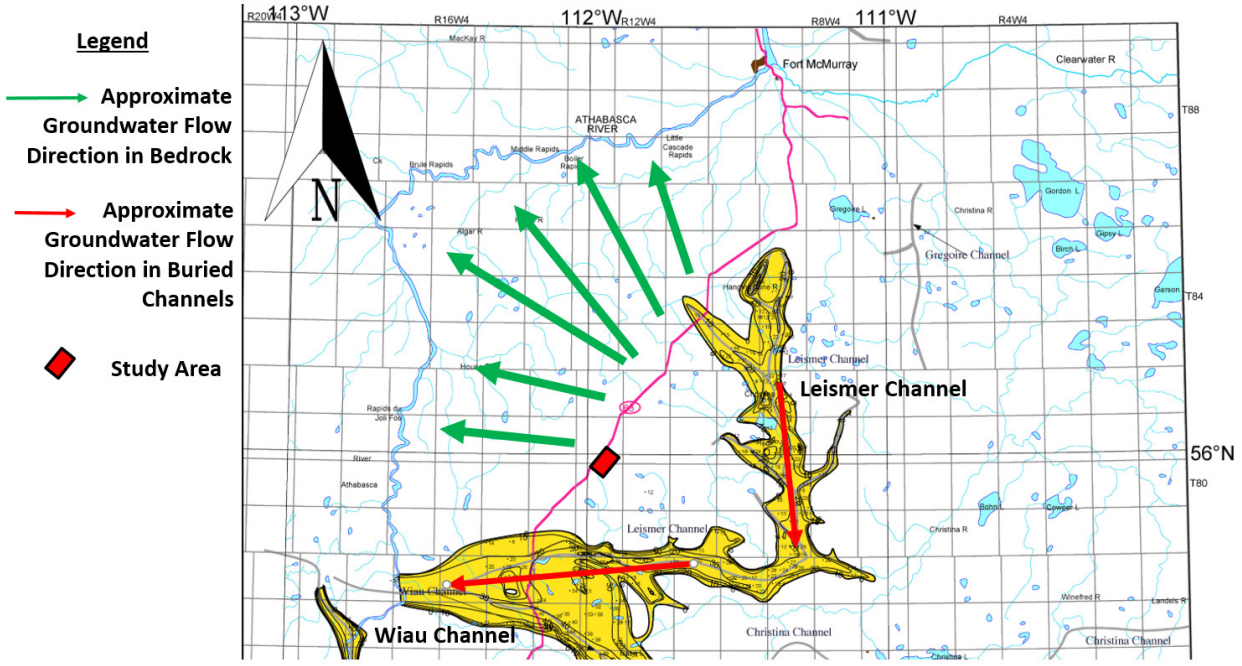

Figure 2.11 Regional groundwater flow of the Southern Athabasca Oilsands Region, where green arrows indicate general trend of groundwater flow direction in bedrock, cascading away from the Stoney Mountain Uplands. The red arrows indicate groundwater flow in the Quaternary channels of the Leismer and Wiau, where localized topography allows groundwater to flow against the regional flow in the Leismer and directly to the west in the Wiau that terminates at the Athabasca River.

3. DATA ACQUISITION

Data acquisition for this project was collected for the purposes of creating a 3D hydrogeological framework to geovisualize peatland volumes and geometry in *Seequent LeapFrogGeo (LeapFrogGeo)* modelling software. High-resolution LiDAR digital elevation data and satellite images were the primary data source for geovisualization and were used to georeference geophysical and hydrological field data. Spatial data were obtained from a variety of sources with varying coordinate systems, resolutions, and quality. These data were organized and processed into a common projected coordinate system within an open source GIS software, QGIS (Nielsen et al., 2017). Pre-processing data in QGIS was an essential initial procedure prior to importing into *LeapFrogGeo* for the purposes of data management, geospatial co-registration, consistent metadata, eliminating erroneous outliers, defining no-data values, and general data filtering.

3.1 Satellite Imagery

Free imagery is available from Google Earth and Google makes available their Google Earth 3D engine, allowing for the development of 3D photo-realistic models of natural landscapes (Horota et al., 2020). The QGIS XYZ tiles function was used to import Google Earth layers (Table 3.1).

Table 3.1 Google satellite imagery uniform resource locator codes

Google Roadmap	*http://mt0.google.com/vt/lyrs=m&hl=en&x={x}&y={y}&z={z}*
Google Terrain:	*http://mt0.google.com/vt/lyrs=p&hl=en&x={x}&y={y}&z={z}*
Google Satellite:	*http://mt0.google.com/vt/lyrs=s&hl=en&x={x}&y={y}&z={z}*
Google DEM:	*http://mt0.google.com/vt/lyrs=t&hl=en&x={x}&y={y}&z={z}*

3.2 LiDAR

For this project LiDAR data were acquired on June 22, 2011 by project-specific flights by a company called *DigitalWorld Mapping* of Calgary, Alberta. The total area surveyed for the study area was approximately 23 km^2 (2300 ha). A two-hour terrestrial kinematic survey was conducted to calibrate aerial acquisition to custom ground control point (latitude 55°53’57.05422, longitude -112°05’31.8473) and Alberta Survey Control Marker ASCM382754 (latitude 55°56’43.06231, longitude -112 01 44.16259).

A kinematic survey was used to increase precision of small changes in flight altimetry during LiDAR acquisition by processing fixed ground-based base-stations with georeferenced positioning system (GPS) coordinates collected from the aerial LiDAR device. The flight altitude was approximately 400 m above mean elevation of the site, the laser scanning frequency was 160 Hz, and the laser firing rate was 200 kHz. The data were processed to an elevation vertical accuracy of 0.044 m and a horizontal resolution of 1 m by 1 m. *DigitalWorld* provided thirty-three elevation grids as *Golden Surfer Grid* format files (grd), which is an ASCII format containing XYZ (easting, northing, and elevation) attributes for bare-earth elevations and first return layers (Figure 3.1).

The data were supplied in Universal Transverse Mercator (UTM) Zone 12 (UTM Z12) grid coordinate system using the horizontal North American Datum 83 (NAD83) in Geodetic Reference System ellipsoid and gravity field model of 1980 (GRS80). Elevation grids formed the primary topographical mesh in *LeapFrogGeo*. Elevation contours and colourized heat maps were created in *LeapFrogGeo* and exported for cartographic projection in QGIS (Figure 3.2, Figure 3.3).

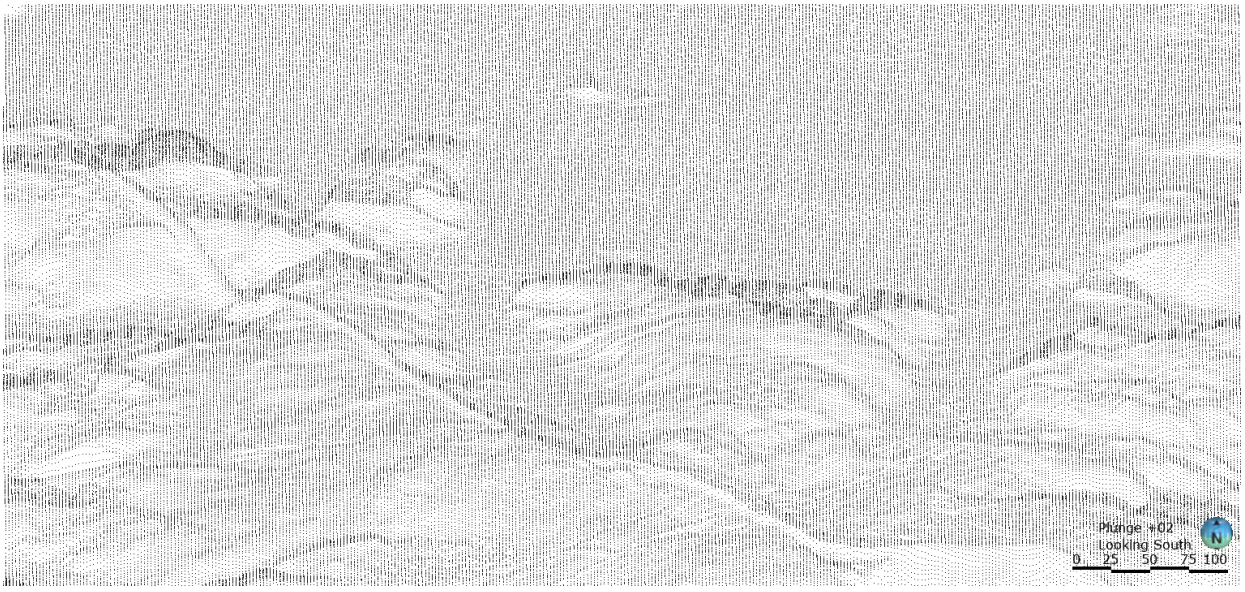

Figure 3.1 Unclassified LiDAR derived bare-earth digital elevation model point cloud of Mariana Fen looking south at an oblique view of plunge of 1° with a vertical exaggeration of 10 times greater than the horizontal.

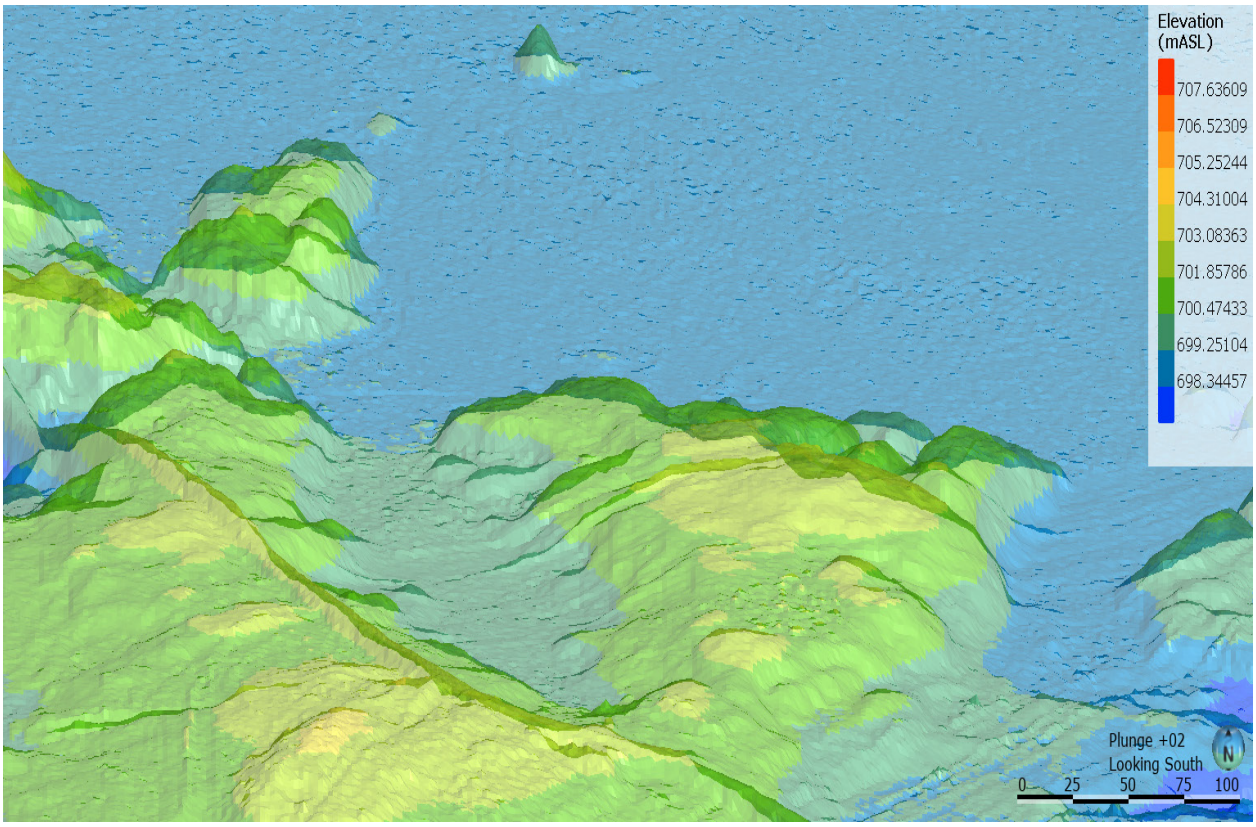

Figure 3.2 Classified LiDAR-derived bare earth digital elevation model (DEM) in an oblique view looking south at a plunge of 1° and a vertical exaggeration of 10 times greater than the horizontal.

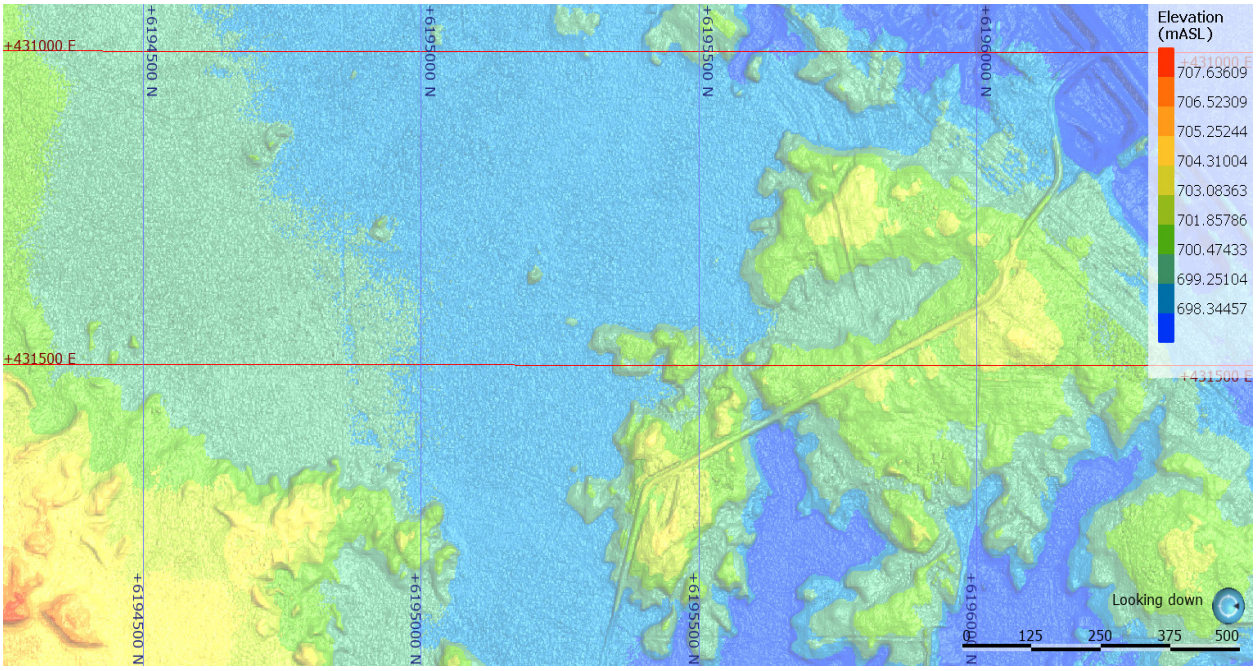

Figure 3.3 LiDAR-derived bare earth digital elevation model in plan view in LeapFrogGeo looking down

3.3 Geological Mapping

Regional geological data of the study area were downloaded from the Alberta Geological Survey (AGS) from their 3D Geological Framework project. The AGS Geological Framework is a detailed set of multi-scale 3D models of Alberta's geology covering over 600,000 km^2 in 12 geological models (Figure 3.4). These models are comprised of geological "units", which are related to the stratigraphic age that include quaternary sediments and older bedrock deposits. The Lower Athabasca Regional Model is derived from detailed subsurface stratigraphic research from the AER and AGS that covers approximately 12% of the Province (80,000 km^2). The Lower Athabasca Regional Model is comprised of 12 geological sub-models from 35 geological units from the quaternary deposits at the ground surface to the Precambrian basement. ASCII files for each model in addition to geospatial data (lines, points, and polygons) were accessed from the AGS geological database.

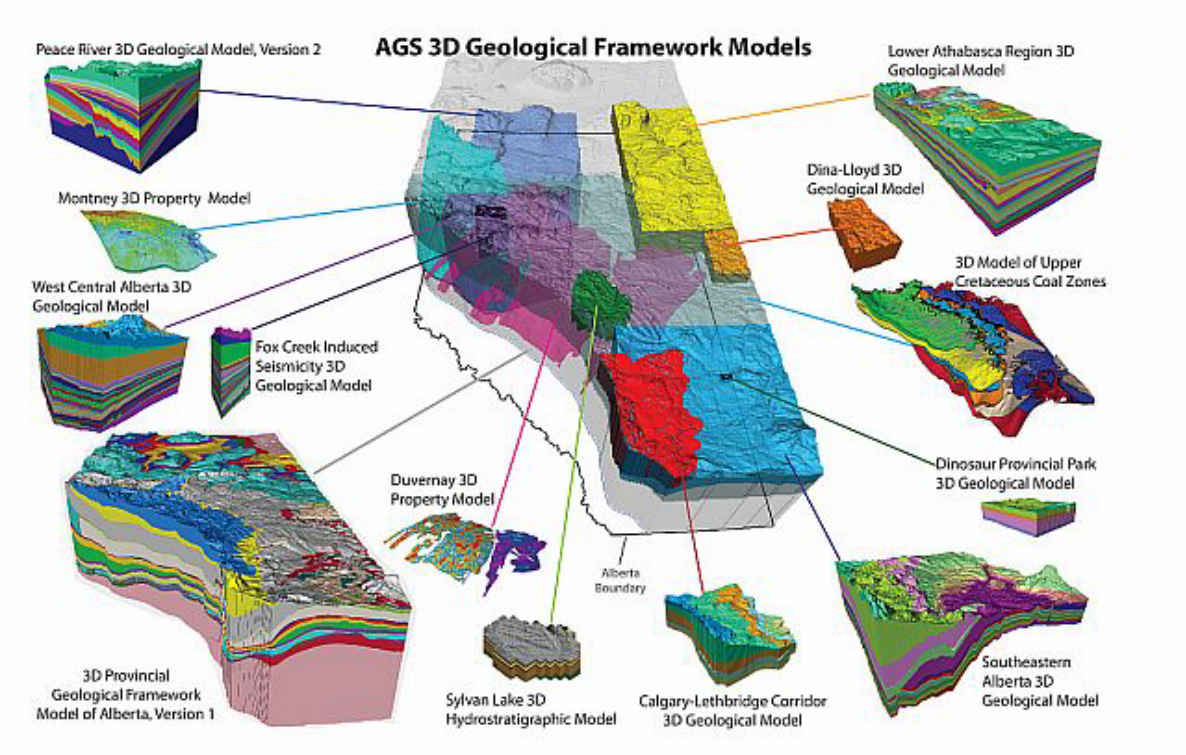

Figure 3.4 Alberta Geological Survey 3D Geological Framework Models of the Province

3.4 Wetland Ecology Mapping

Wetland landscape unit delineation in the study area was established in the 1980s (Constible et al., 2001; Hutton et al., 1994; B. J. Nicholson, 1989; Barbara J. Nicholson, 1987; Barbara J. Nicholson & Vitt, 1990; Wieder et al., 2019). The landscape units for the study area were updated by Küsel (2014) and Vallarino (2014) and again by Cherry (2015) using aerial imagery and vegetation mapping and classified into wet-fen, dry-fen, bog, and uplands. The boundaries were re-digitized in this project using QGIS from existing maps (Figure 3.5).

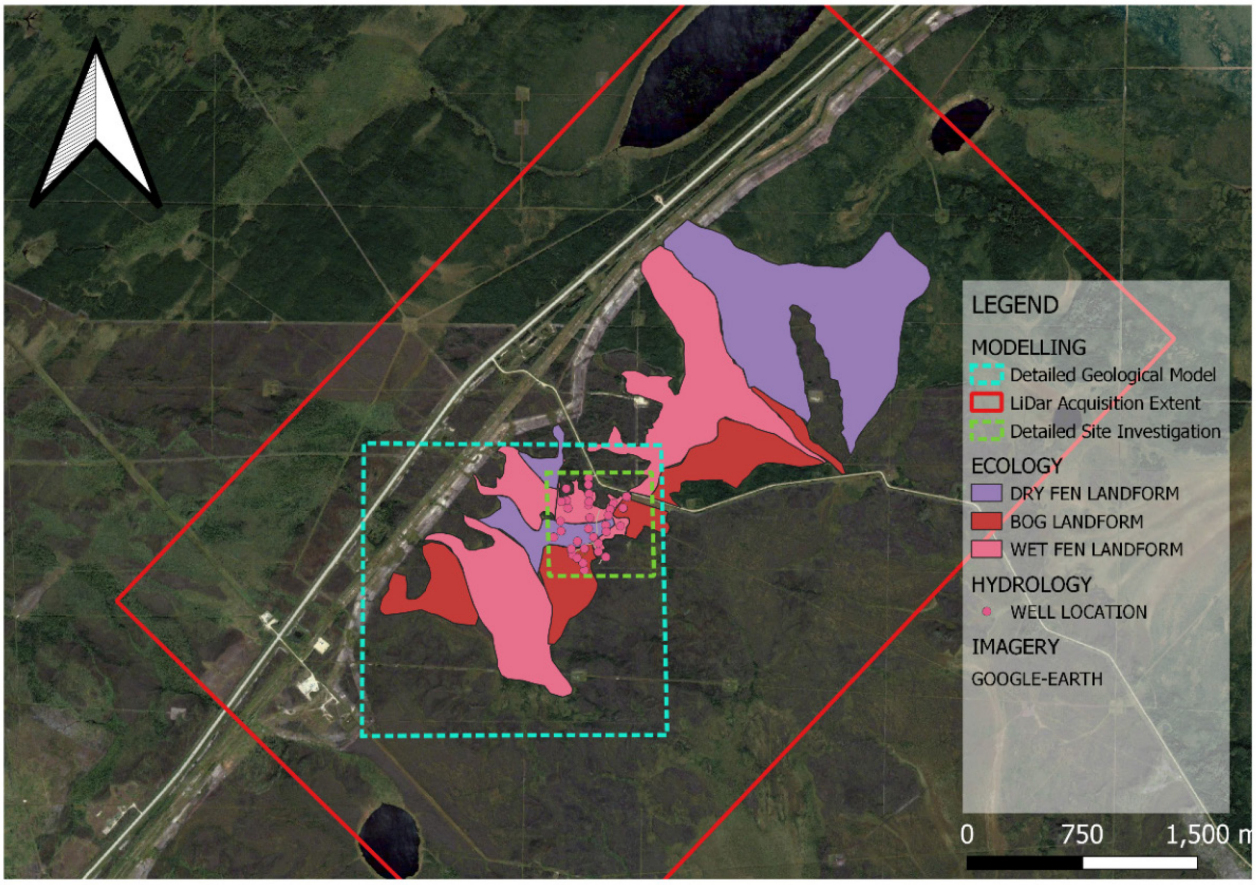

Figure 3.5 Plan view of ecological landforms within the detailed site investigation area of the study area were defined by existing research as part of the CEMA nitrogen amendment program and those data were digitized for this project in QGIS and overlain with Google Earth imagery. The ecology adjacent to the detailed site investigation area were estimated using imagery and LiDAR derived topography.

3.5 Trails and Infrastructure Mapping

Trails, instrumentation, and other infrastructure relating to the project were located using *Bad Elf™ Surveyor Pro+* Global Navigation Satellite System (GNSS) device connected with Bluetooth to Garafa GIS application Apple© iPhone™ iOS (Figure 3.6). Typical horizontal resolution is less than 1-metre radius of the target with maximum error set to 10 m radius.

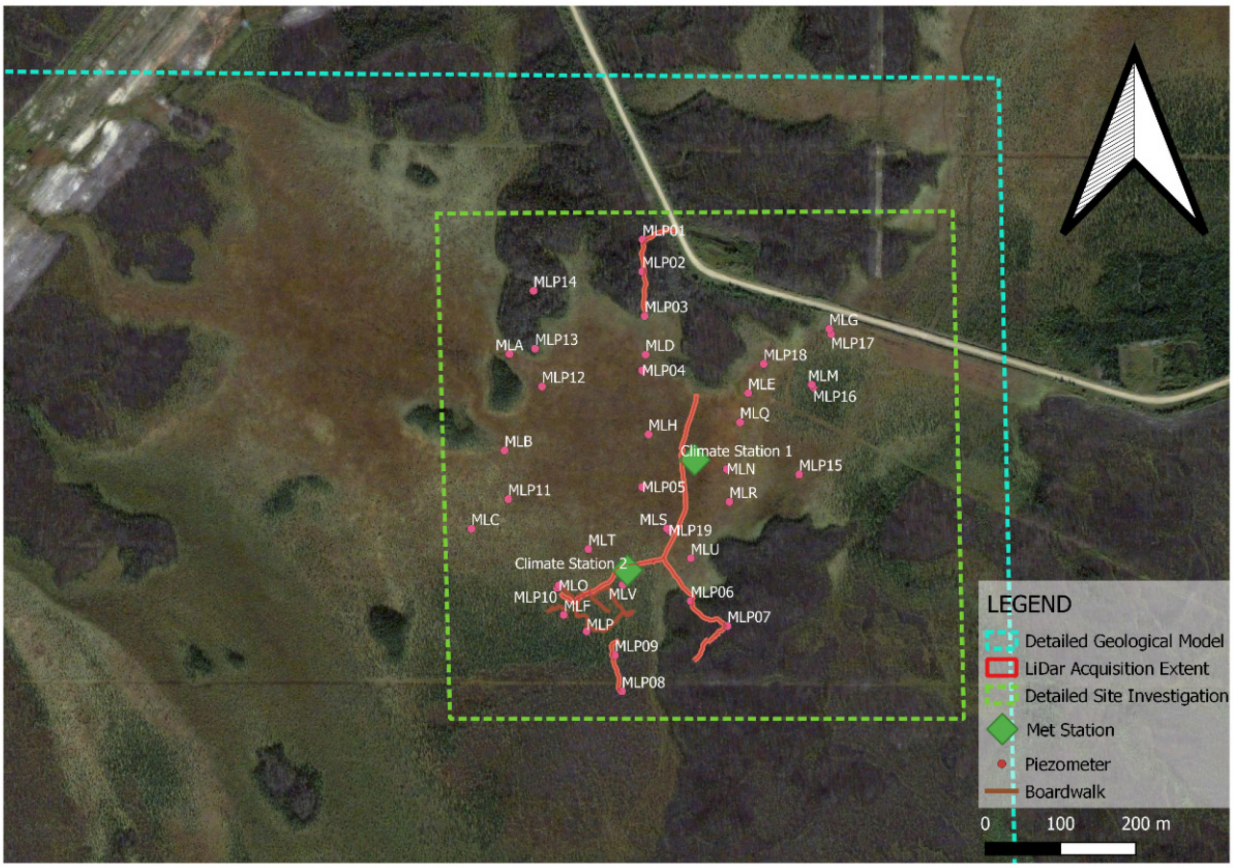

Figure 3.6 Plan view of boardwalk trail network within the detailed site investigation area with piezometer locations and met station. The access road is visible in the north-eastern section of the detailed site investigation. See 3.9 Drive-point Piezometer Monitoring Stations for discussion of the piezometer network and depth, location, and lithology information at Appendix D: Piezometer and Water Table Well Details.

3.6 Open Government Data

Open Government Data Series *CanVec* was accessed using the Geogratis Geospatial Data Extraction Tool (Natural Resources Canada, 2017).

Table 3.2 Open Government CanVec geospatial data.

Hydrographic Features	Watercourses, water linear flow segments, hydrographic obstacles (falls, rapids, etc.), waterbodies (lakes, watercourses, etc.), permanent snow and ice features, water wells and springs.
Transport Features	National Road Network (NRN) and the National Railway Network (NRWN) that describes and provides attributes for roads, trails, bridges, railroads and related information.
Elevation Features	Elevation contours and elevation points used to describe the relief of landmass.
Administrative Features	Geopolitical regions (international, territorial and provincial) and populated place names and attributes.
Toponymic Features	Proper nouns designating places and representations of the territory from provincial, territorial and Canadian toponymic databases that are used for cartographic reference purposes.
Land Features	Islands, shoreline delineation, wooded areas, saturated soil features, landform features.
Manmade Features	Dams, protection structures (breakwater, dike/levees), liquid storage facilities (basin, swimming pool, etc.), tanks, buildings, delimiting structures (fence, walls, etc.), landmark features (cross, radar, crane, forts, etc.), chimneys, towers,...
Resource Management Features	Power lines, communication lines, pipelines, valves, petroleum wells, wind-operated devices, transformer stations, ore extraction sites, aggregate extraction sites, peat extraction sites and oil and gas sites.

3.7 Ground Penetrating Radar

This project used two Swedish-made GPR antenna systems, MALÅ Rough Terrain Antenna (Appendix A) and RadarTeam Subecho40 (Appendix B) to determine the peatland-substratum subsurface horizon (Figure 1.1). GPR instruments are low-powered electronic systems that produce and receive Ultra Wide Band (UWB) electromagnetic (EM) signals from one or more antennas containing transmitter (Tx) and receiver (Rx) devices. Known as time-interleaved systems, one sample is collected on the receiver each time the transmitter transmits an electromagnetic signal.

The GPR signal attenuates through differing materials. It was estimated that the GPR signal travelled through the peat at approximately 0.05 m per nanosecond or approximately 500,000,000 m/sec with an average of 400,000 transmissions every second. Variations in timing of signal return through the subsurface are converted to useful information by the GPR system to determine depth of a buried object or boundary. To address attenuation of EM signals by soils, subsurface materials, and groundwater, larger GPR waveforms are used (<10 MHz to approximately 1000 MHz) in geoscience applications. These antennas are usually unshielded and typically transmit signals at several hundred kilohertz (KHz).

For this project, GPR was collected in continuous mode, meaning that the antenna was transmitting and receiving electromagnetic signals in a set interval. This approach allowed operation of the GPR system by one person by foot. GPR data were collected in Winter 2014 with the GSSI Subecho40 Antenna System and in summer 2015 with the MALÅ Rough Terrain Antenna System. The acquisition process using the GSSI Subecho40 antenna system was marginally successful since there was significant amount of inherent noise from a subharmonic frequency within the antenna that was difficult to filter and process. The data were used for two-dimensional conceptualization to guide additional GPR acquisition but were not subject to extensive analysis.

GPR data acquisition using the MALÅ Rough Terrain Antennas (RTA) returned relatively clean data, providing resolution sufficient to define the subsurface boundary between peatland and the substratum as well as structures within the peatland, including the active layer, the anaerobic layers, and buried alluvial channels.

Over 100 GPR lines were attempted with the MALÅ RTA; nearly half of these were for calibration and testing purposes. Approximately 30 GPR lines were retained for detailed processing and 17 were used for detailed structural 3D modelling in *LeapFrogGeo* (Figure 3.7).

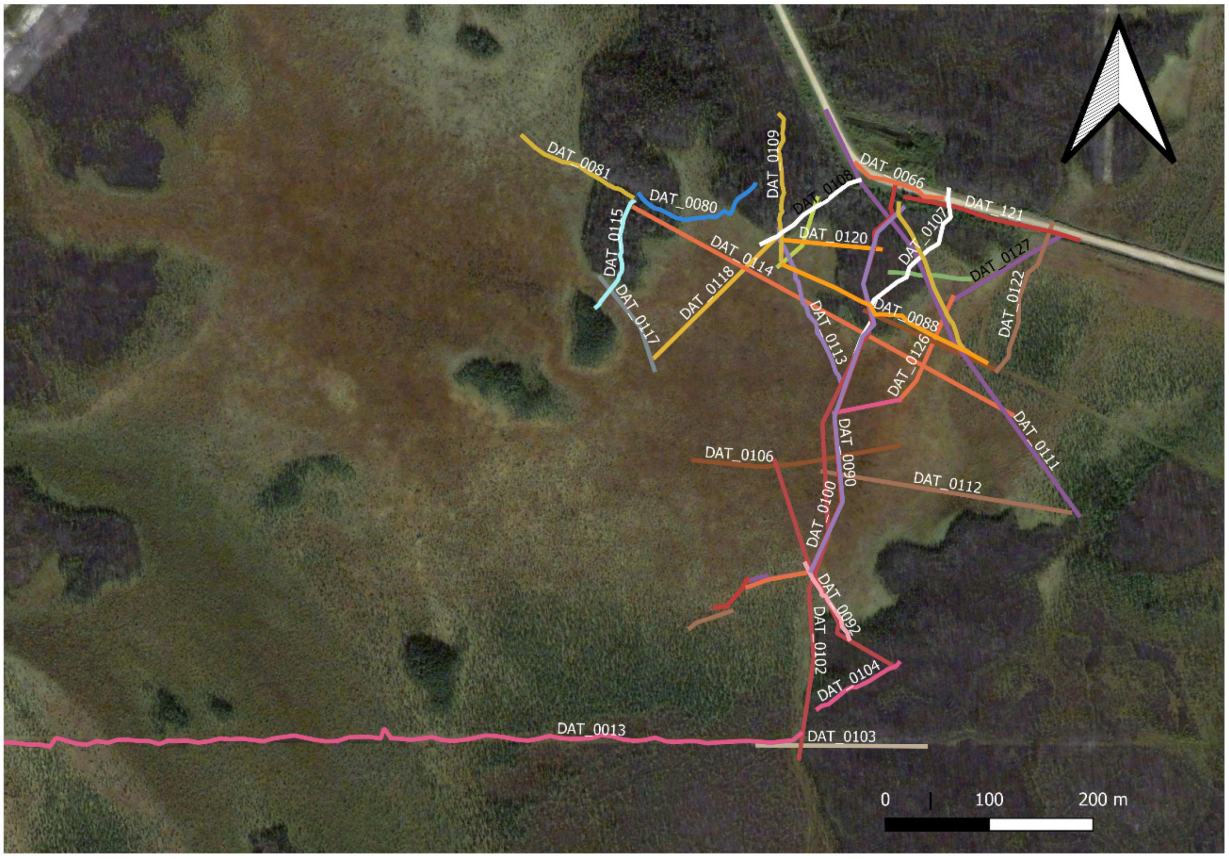

Figure 3.7 GPS data from GPR acquisition at study area.

3.8 Hydrometrics

The purpose of hydrometric surveys is to obtain high quality meteorological and hydrological data from integrated and non-integrated stations in the hydrometric network (Government of BC Ministry of Environment, 2009). Integrated stations are those that are contained within a larger managed network such as the Water Survey of Canada or the provincial observation well network. Non-integrated hydrometric station are project specific monitoring locations that are not connected to a larger network. Non-integrated hydrometric data were collected at the study area from two locations, in the bog and in the fen from Campbell Scientific weather stations installed by the research team. These stations, when operational, gathered ambient temperature, soil temperature, precipitation, relative humidity, and solar irradiance (Tattrie, 2011). Integrated hydrometric data were collected from weather stations managed by Alberta Agriculture and Forestry, Alberta Climate Information Service.

3.9 Drive-point Piezometer Monitoring Stations

Drive-point piezometers were used to monitor shallow groundwater and peatland vapour. Installation of the piezometers followed the methodology of Tattrie (2011) by driving stainless steel drive-point Solinst™ 615 piezometer tips attached to lengths of 0.75” diameter National Pipe Thread (NPT) galvanised steel pipe. Shallow piezometers and water-table wells have Solinst™ 601 drive-point tips attached to 1.25” diameter polyvinyl chloride (PVC) pipe. The piezometers were fitted with polyethylene (PE) tubing fed through the steel or PVC casing from bottom to the top for water sampling. Water table wells are perforated along their entire subsurface length and not fitted with sample tubing (Figure 3.8). Tattrie (2011), Küsel (2014), Vallarino (2014), and Cherry (2015) describe the method used for installing drive-point piezometers and shallow wells using a portable hammer drill, known as a *pionjar*. Lithological and sediment changes in the substrate provided resistance to installation. The installation of piezometer nests describes upland lithology (MLP01, MLP02, MLP07, MLP14) as till from surface to approximately 1.1 mBGL, sand from 1.1 to 1.65 mBGL and till at depths greater than 1.65 mBGL.

Piezometers installed in the edge sites at locations MLP03, MLP06, MLP13 consist of silty sand from surface to approximately 2 mBGL, silty clay from 2 to 4 mBGL, then refusal at a hard clay substratum at depths greater than 4 m. In peatland sites installations described peat in the shallowest horizons from surface to approximately 2.33 mBGL as soft, similar to the substrate for mid-depth installations, and hard till substrate refusal at the bottom of the deepest piezometers. The installation notes described that the deepest wells were installed at different total depths. Deepest wells were found in the areas identified as “wet-fen” by surface vegetation. In summer of 2015 upland locations, MLP02, MLP14, and MLP07 were reinvestigated using a handheld borehole digger and confirmed the original drilling notes from Tattrie (2011).

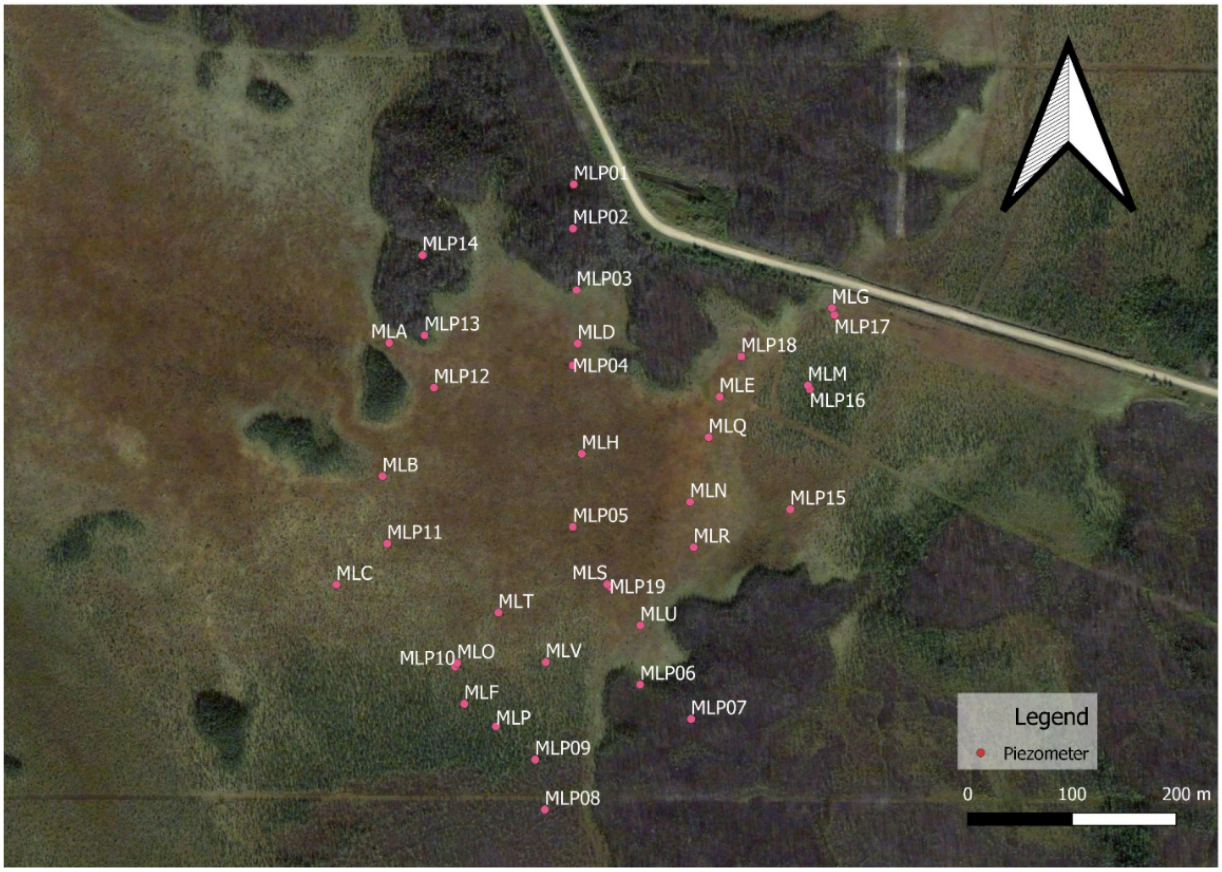

Figure 3.8: Drive-point piezometer nest locations and water-table locations.

3.10 Water-Table Level Monitoring Stations

Water table wells were installed to a maximum of 0.5 m in several areas of the peatland (Figure 3.9). These monitoring locations are made with slotted PVC and continuous monitoring of water-levels was attempted using Odyssey™ capacitance data loggers in hourly intervals during the winter and every ten minutes during the open-water season. These monitoring locations were also sampled for geochemistry. Details of piezometer installation locating in Appendix D.

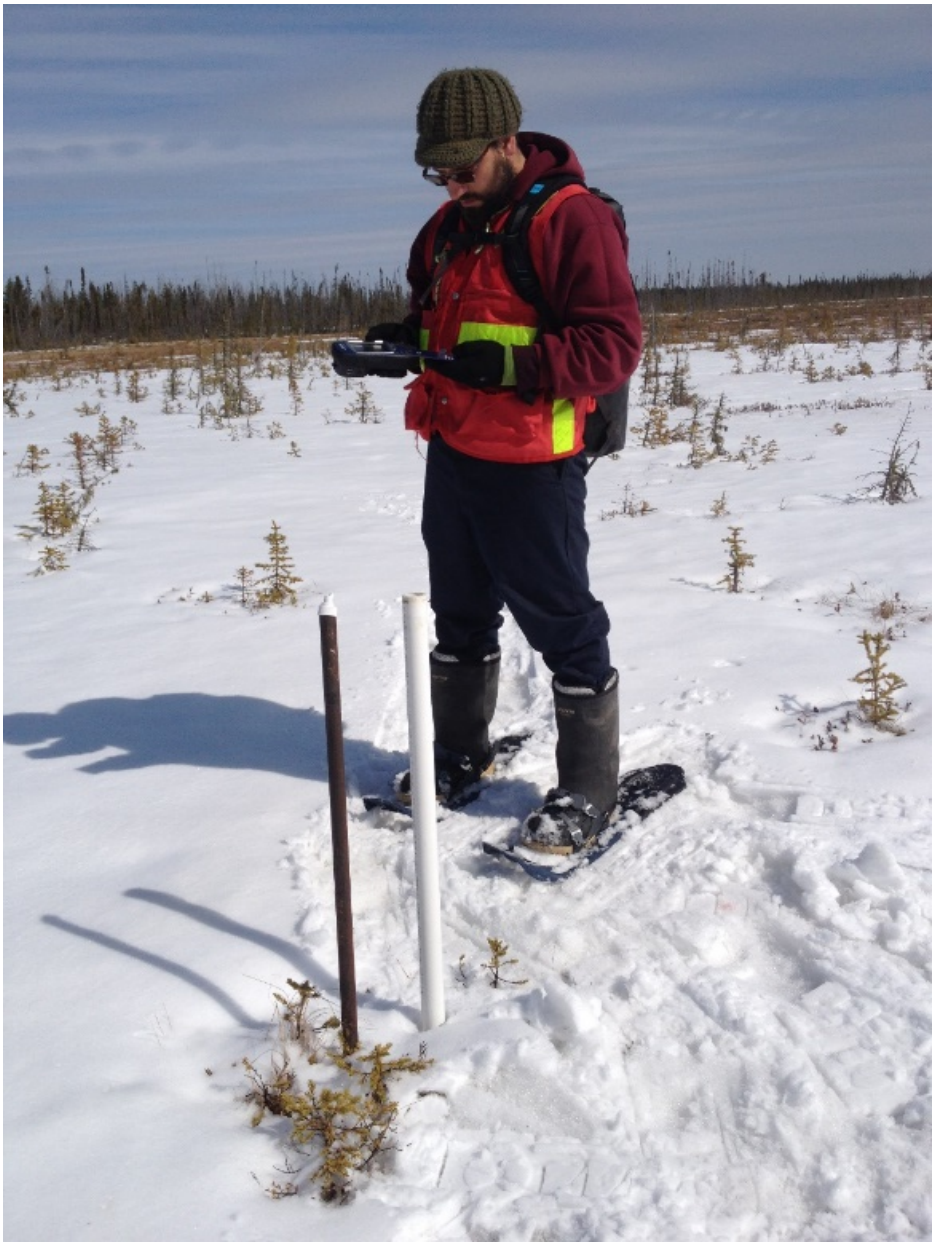

Figure 3.9 A wintery view of piezometers at the fen. Photo by Pacific Northwest Tree Stewards.

3.11 Hydrogeochemistry

Water quality sampling was completed in the summer and fall seasons in 2013, 2014, and 2015 at most water-table wells and piezometers. Water samples collected using the methodology established by Küsel (2014), Vallarino (2014), and Cherry (2015). Measured parameters include the isotopes of water (^{2}H, ^{18}O, ^{13}C, ^{15}N), dissolved organic carbon (DOC), dissolved organic nitrogen (DON), major ions, trace metals, and tritium (^{3}H) sampling was carried out only in 2014 (Figure 3.10) with methods described by Cherry (2015). Major ion concentrations, nitrate, nitrite, sulphur, iron, and phosphorus were measured in the field using a portable Hach colorimeter (Figure 3.10). Alkalinity was analysed in the field using a hand-held digital titrator. Cherry (2015) and Küsel (2014) describes that DOC and DON were analysed at Alberta Innovates in Vegreville, Alberta, using segmented flow analysis with acid and persulphate UV digestion methods. Cherry (2015) describes that stable isotopes of water (^{2}H and ^{18}O) and ^{13}C of dissolved inorganic carbon (DIC) were analysed at Alberta Innovates at the Vancouver Island Technology. Cherry (2015) also states that stable isotopes for ^{15}N and ^{13}C of particulate matter were also analysed at Alberta Innovates at the Vancouver Island Technology Park using an isotope ratio mass spectrometry and that enriched tritium samples were analysed at the University of Waterloo Environmental Isotopes Laboratory using an ICP-MS X.

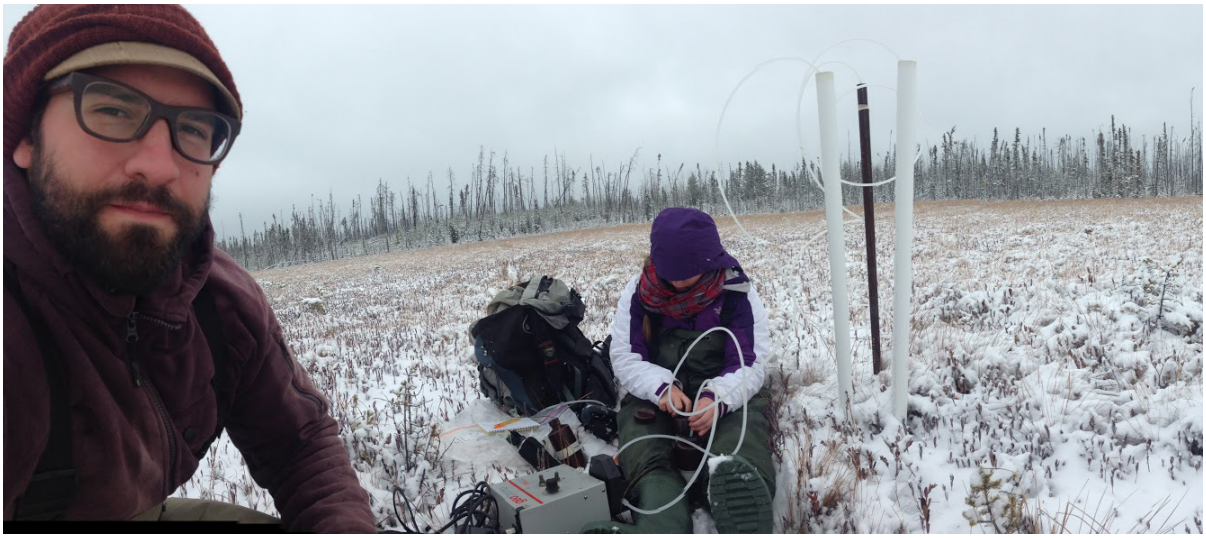

Figure 3.10 Panoramic photograph of Mikaela Cherry geochemical sampling and William Shulba on bear watch, Oct 2014, Photo by Wm. Shulba

4. THREE-DIMENSIONAL HYDROGEOLOGICAL FRAMEWORK

This chapter presents key elements of a hydrogeological framework used to organize geological and geospatial data in *LeapFrogGeo,* an implicit modelling software program (Seequent Limited, 2020) to geovisualize boreal peatland architecture in three dimensions. Organized to match the hydrogeological framework "project tree" in *LeapFrogGeo,* this chapter explores data types, analysis of those data, and multiple modelling outcomes. The project tree is a series of folders organized into categories of objects and features such as geological data, non-temporal hydrological data, temporal climatological and geochemical data, spatial information, imagery, and triangulated irregular network (TIN) surface meshes (Figure 4.1)

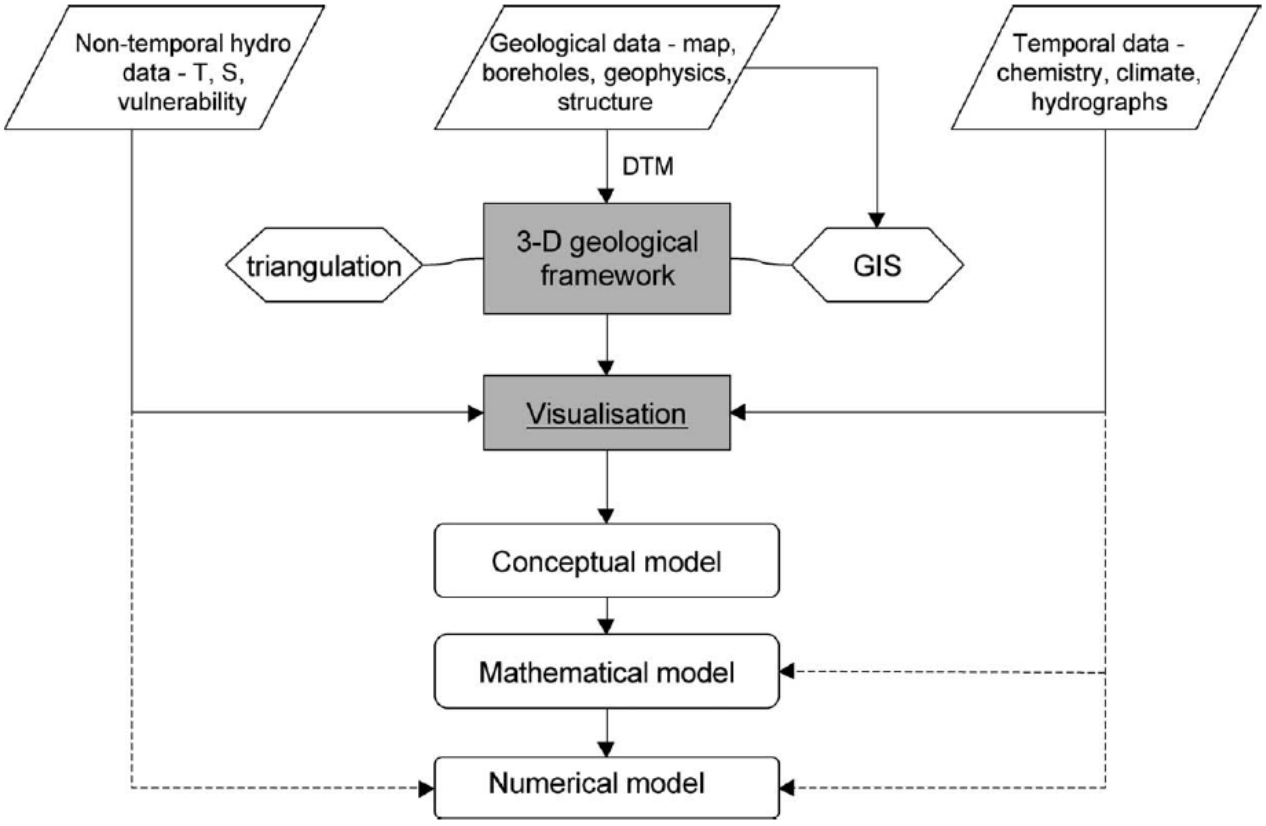

Figure 4.1 Process flow diagram for integrated conceptual, mathematical, and numerical models using a 3D hydro]geological framework.

4.1 Topographies

Topography is not a necessity in geological modelling however it was a central component of peatland architecture modelling for this project. LiDAR-derived topographic grids of bare-earth-reflections and first-reflections were created in *Golden Software Surfer* (*Surfer*) by collating 66 equiareal binary grid tiles supplied by *DigitalWorld*. Two contiguous topographic grids were imported into *LeapFrogGeo* and processed into digital elevation wireframe meshes; each mesh covered 27,384,000 m^2 resulting in over 11 million triangles with 5.8 million vertices for an overall grid spacing resolution of 1 m x 1 m with a maximum elevation of 711.65 mASL to a minimum elevation of 673.19 mASL (Figure 4.2). The topographic resolution is a resultant of the number and size of triangles used to address the vertices of the elevation grid files (Figure 4.3). High-resolution topographic mesh (1 m x 1 m) that required more triangles and longer processing times were retained for detailed visualizations. A coarser resolution (10 m x 10 m) downscaled topographic wireframe mesh was generated for use as the bounding mesh for geological modelling. Matching the topographic mesh to the desired resolution of geological modelling reduced the complexity of contact interpolation and calculated simpler resultant meshes, which resulted in significant processing time savings.

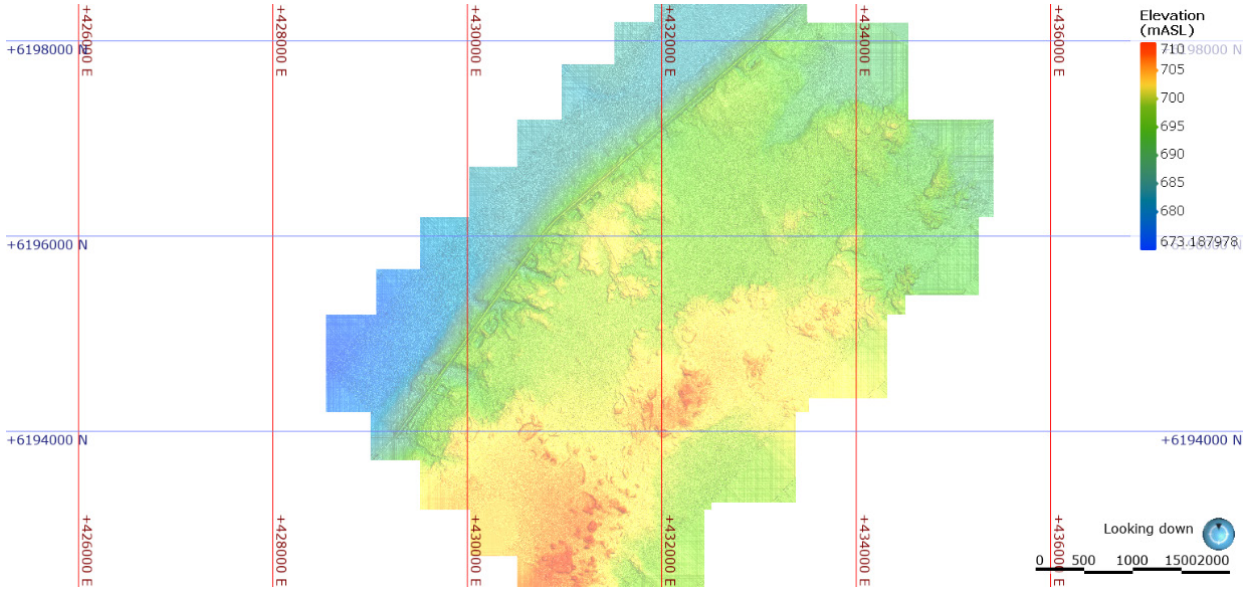

Figure 4.2 LiDAR- derived bare-earth digital elevation model of the study area.

Topographic display options were created by classifying the elevation data using a discrete algorithm, generating 10 progressive intervals of the RGB (red, green, blue) spectrum to be assigned between 673 and 711 mASL (Figure 4.3). In addition to colourmap, GIS data, maps, and images were displayed on topography. Lower resolution false colour Google Earth imagery was draped onto the digital elevation model allowing for basic navigation of the landscape and to observe large landscape features (Figure 4.4). A powerful application using digital elevation models in *LeapFrogGeo* was draping GIS and mapping elements like boardwalks, wells, meteorological stations, sample plots, and landscape features onto the topographic mesh surface to attribute accurate elevation information to those features. GPR was collected over a variety of terrain and calibrating the GPR signals to elevation is essential to determining depth reflectors. Real-time elevation collection using GPS devices during GPR acquisition to attribute elevation data to each trace had significant associated error, often greater than a meter. LiDAR derived digital elevation model has approximately 0.05 m vertical accuracy which is useful for attributing elevation data to GPR. Draping GPR traces on topographic meshes in *LeapFrogGeo* proved to be an efficient and ultimately an invaluable tool for attributing elevation to GPR traces (Figure 4.5).

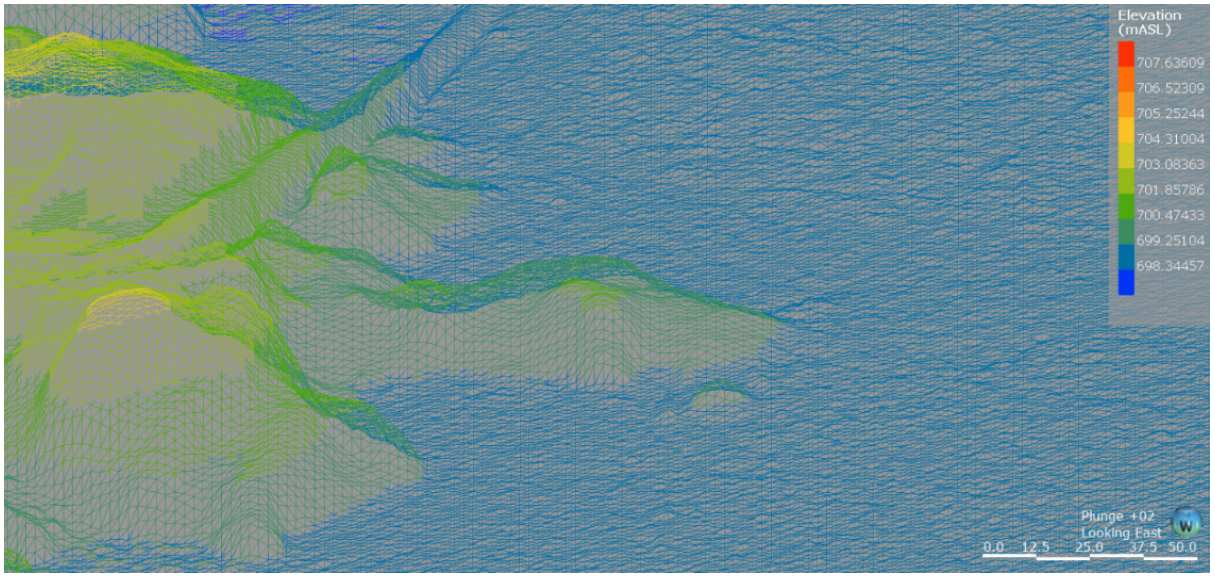

Figure 4.3 Digital elevation model grid triangles forming a topographic mesh, looking east at a plunge of 2 ° and a vertical exaggeration of 10x.

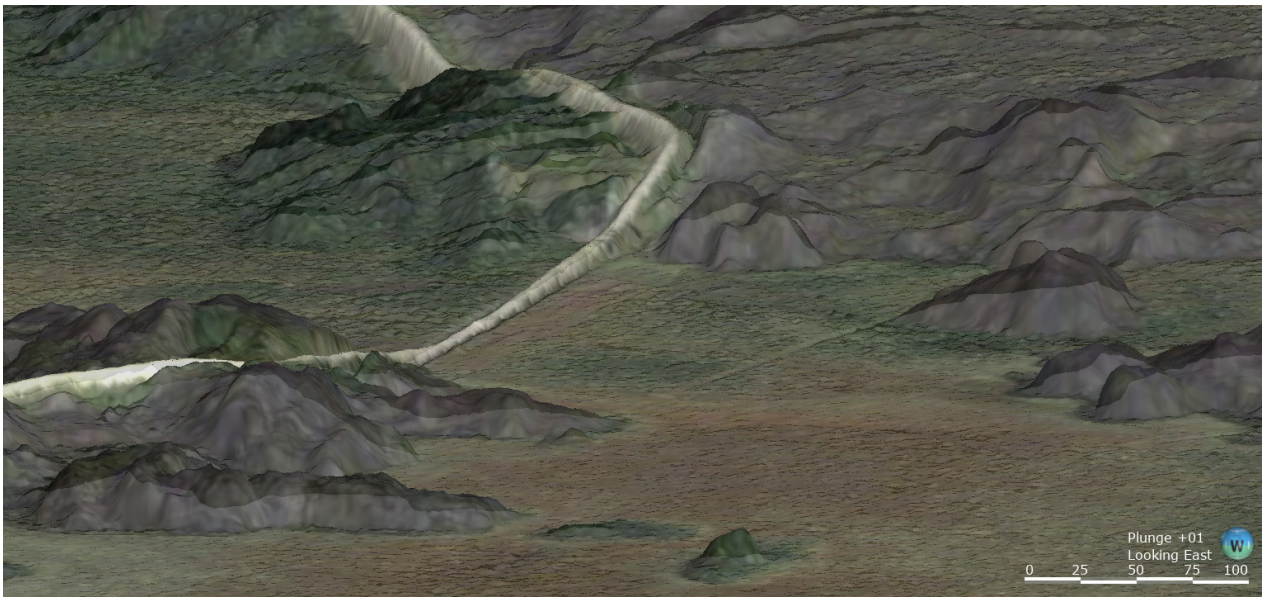

Figure 4.4 Google Earth imagery draped on digital elevation model wireframe mesh, looking east, vertical exaggeration 10x.

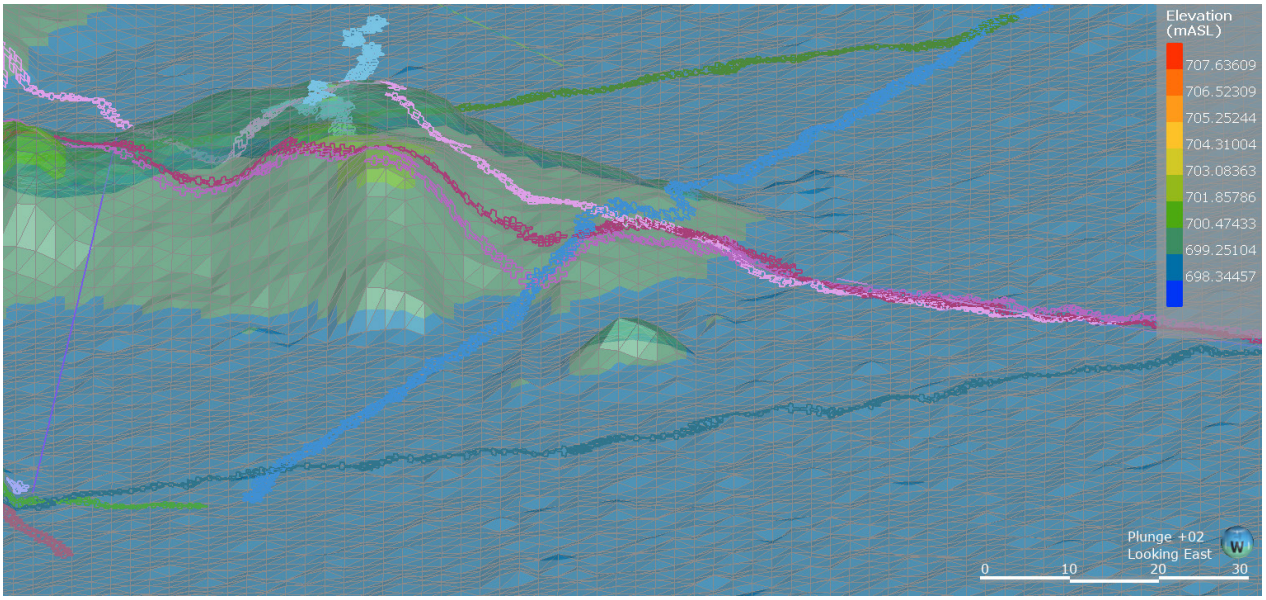

Figure 4.5 GPR lines draped on digital elevation wireframe mesh. GPS information was collected during GPR data acquisition which is denoted in the GPR lines as cross symbols. The GPS horizontal coordinates were coupled with the elevation information at each individual coordinate using the LiDAR derived digital elevation model.

4.2 GIS Data, Maps, and Photos

LiDAR-derived bare-earth and first reflection digital elevation surfaces were imported and Google Earth satellite imagery was draped onto those surfaces. Elevation data from Google Earth imagery was ignored as elevation was set by LiDAR-derived digital elevation surfaces.

4.3 Drill Hole Data

Drillhole data contained four interconnected referencing tables: (i) *collar table* with location of the drillhole, (ii) *survey table* containing information that describes the trend and depth of drillholes, (iii) *interval table* that contains supporting information such as lithology, and (iv) *screens table* that identifies where water enters the drillhole. Drillhole data was derived from 48 piezometers grouped in 18 piezometer nests.

Drive-point piezometers are not like traditional drilled boreholes as they are inherently limited in geological information due to the lack of soil returns to the surface during installation. However, the substratum provided significant resistance to drive-point installation (Cherry, 2015; Vallarino, 2014; Tattrie, 2011) giving lithological insight to the overall depth of peat as the deepest drive-point would not penetrate the substratum. The refusal depth is determined to be the bottom of the peatland. Although lithology was not directly observed, the depths were estimated in the drill hole locations and tabulated for entry into *LeapFrogGeo*.

All drive-point piezometers were considered to be vertical at a dipping angle of 90 degrees with an associated dipping direction of 360 degrees (due North) when imported into *LeapFrogGeo*. In complex geological investigations dedicated drilling and lithological coring programs allow for drillholes to have multiple angles which helps triangulate geological features such as faults, folds, pay zones, and complex geomorphology. Although drillhole data associated with this project is simplistic, the drillholes provided an essential role in geological modelling by determining the total depth of peat in several locations (Figure 4.6).

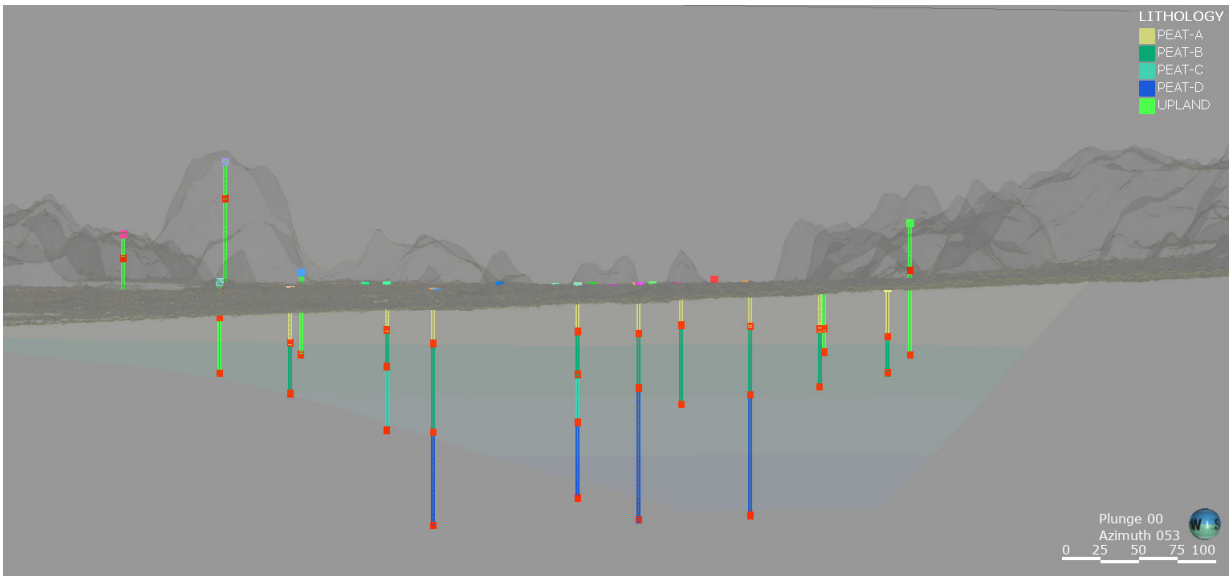

Figure 4.6 Nested drive point piezometers combined as single drill hole with segments assigned to lithological features with the bottom screen of the individual piezometer shown in red.

4.4 Points

LiDAR derived bare earth grid data was loaded into *LeapFrogGeo* as point data. Evaluations were completed on the dataset to define uplands in complex areas and remove erroneous elevations from shadowing at peatland edges. This was done by selecting the points in the scene view of *LeapFrogGeo* and performing filtering to select and smooth erroneous topographic elements (Figure 4.7).

4.5 Polylines

Polylines were created using vector GIS data and were drawn directly on objects in scene view. Polylines are special 3D elements made of line segments that are connected by nodes. Each polyline contains a surface ribbon with a midline and a positive (upward looking) and negative (downward looking) surface. Polylines were drawn on GPR radargram horizons to identify lithological unit contacts. Structural disc data was estimated from these polylines. (Figure 4.8)

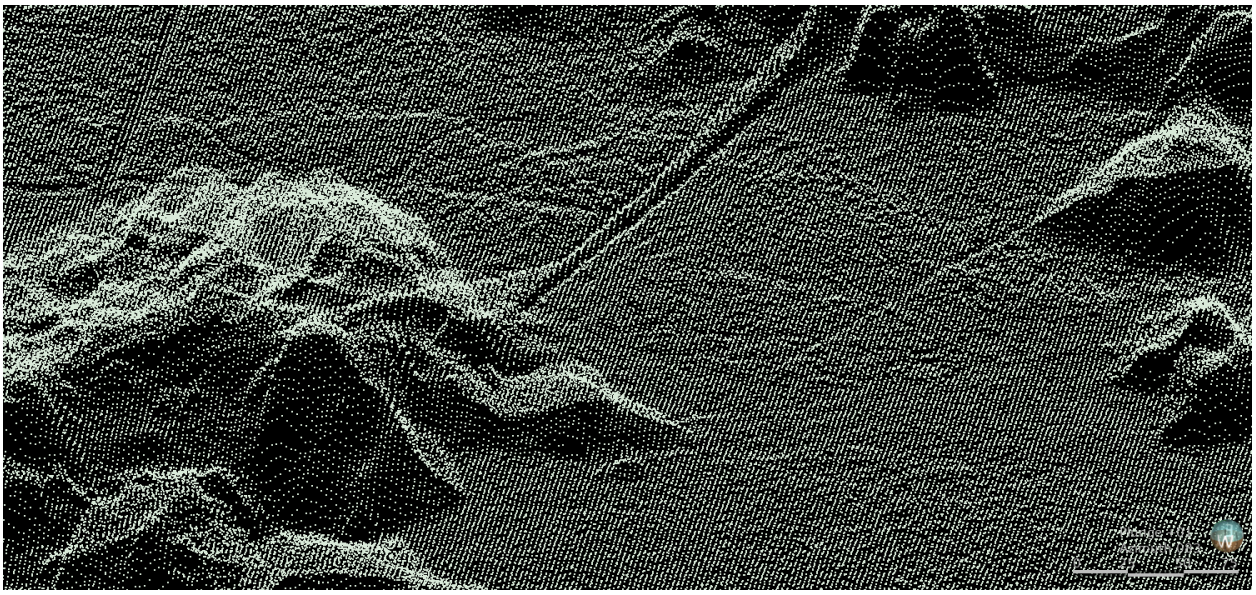

Figure 4.7 LiDAR derived digital elevation point cloud data visualized in LeapFrogGeo

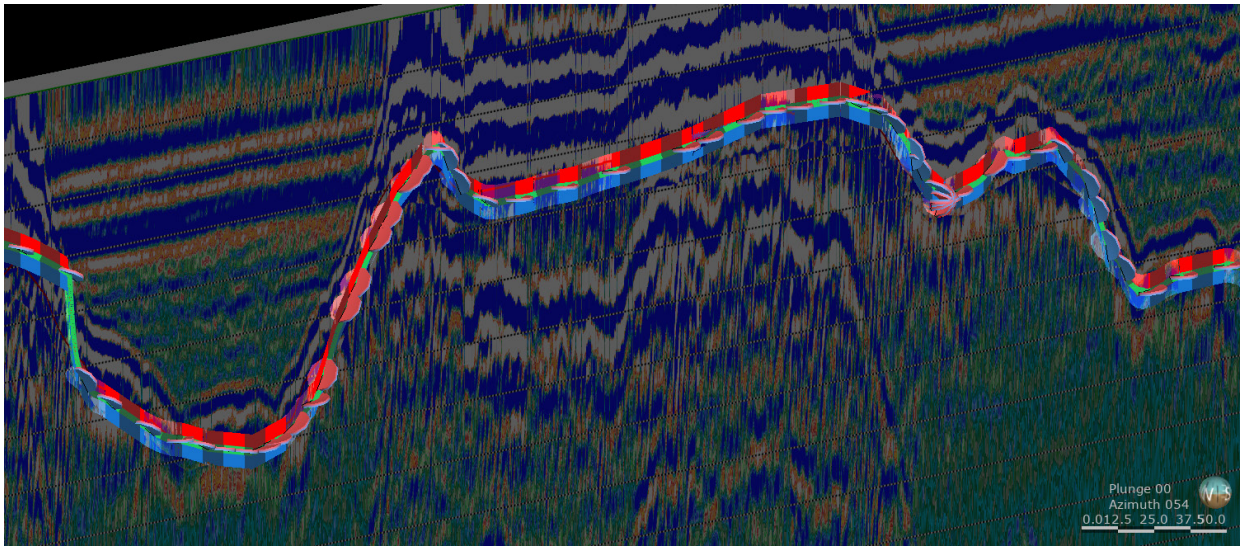

Figure 4.8 Polyline with associated structural data discs on GPR radargram in 3D space.

4.6 Geophysical Data

Geophysical data were uploaded as two-dimensional (2D) radargram cross section images under the *cross-sections and contours* section of the project tree. In total there were 17 GPR radargram cross-sections imported into *LeapFrogGeo (*Figure 4.9 *and* Figure 4.10*)*. Raw geophysical x, y, z data were imported from GPR processing as an ASCII into *LeapFrogGeo*.

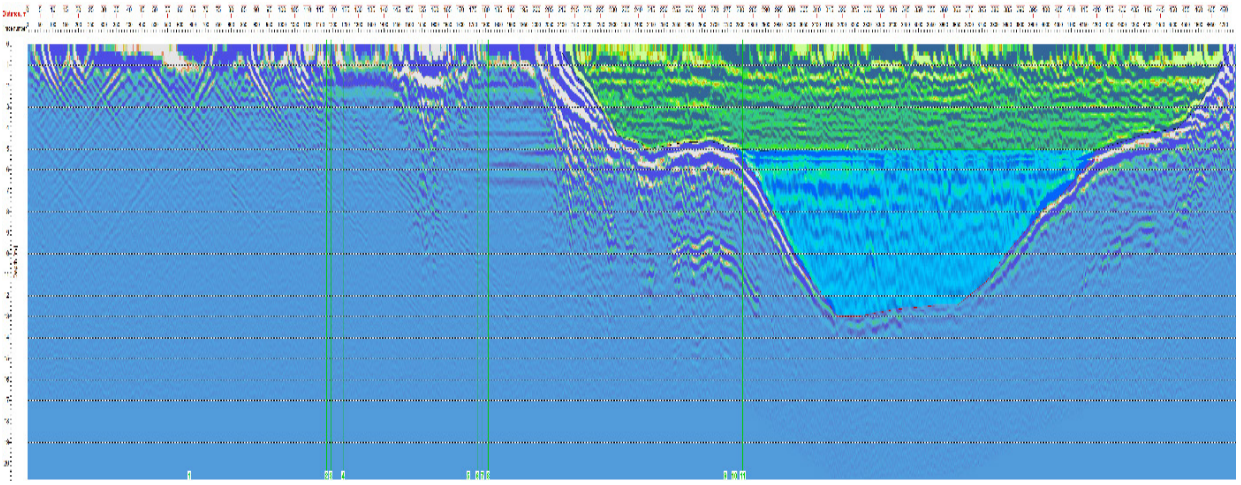

Figure 4.9 Long bitmap image of a GPR radargram at 20x vertical exaggeration cutting obliquely through a buried channel (DAT_0111).

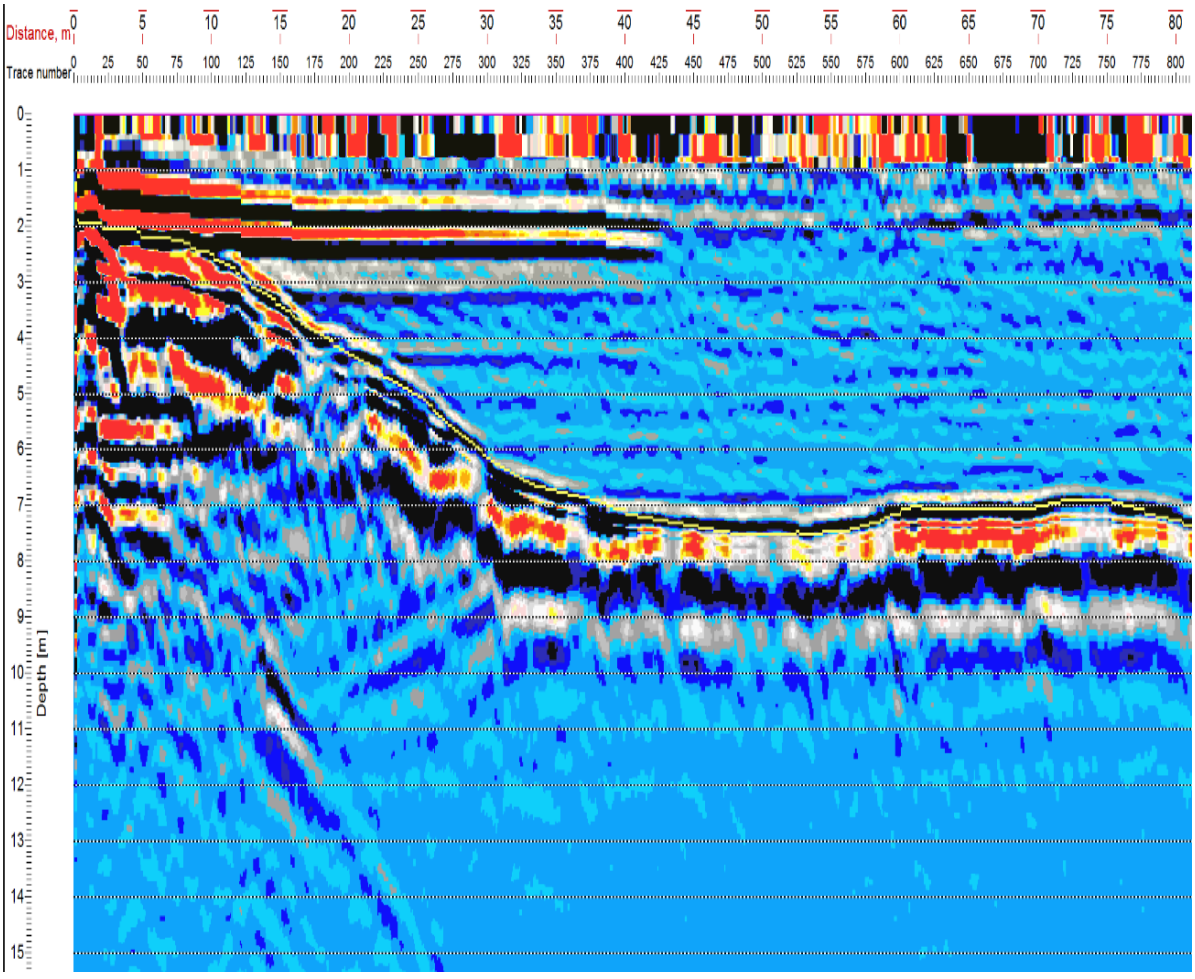

Figure 4.10 Close-up on bitmap of a GPR radargram cross section at 20x vertical exaggeration (DAT_0111).

4.7 Structural Modelling

Structural data was created in *LeapFrogGeo* from interpretation on GPR radargram cross-sections using structural planar discs (Figure 4.11). Structural planar discs use several elements of control including easting (x), northing (y), elevation (z), dip degree, and dip azimuth (Figure 4.12). Like traditional geological maps, structural data points are drawn along strike (the direction the intersecting line of a surface with a horizontal plane) in the appropriate orientation with a chosen dipping angle. Orienting the structural planes along strike of the GPR lines was intuitive as the cross-cutting of the GPR radargram to the reflecting structure (peatland bottom) was adequately displayed. However, determining the dip of the structural element was problematic since the GPR radargram inherently lacks dip information of the reflecting structure. The nature of implicit modelling aided to overcome this. First pass structural modelling was done with placing few structural disc points in selected locations along the GPR line and the modelling process was run to create a generalized block volume representation of the peat. The geometry of the volume was refined by placing more structural data points along the GPR cross-section and using the edges of the resulting volume as a guide to weave together structural points from different GPR lines in 3D space in an iterative way until a predictable geometry emerged (Figure 4.13). The interface between peatland, substratum, and uplands is a complex relationship. Interpolating the contact between these landscape units was not overly complex; however, due to the sinusoidal nature of surficial peatland boundaries manual delineation of the contacts were needed. A peatland extent shapefile was defined in *QGIS* using aerial imagery and imported into *LeapFrogGeo* as a polyline feature and converted to estimated structural data. Although efficient, this method generated many erroneous structural data points and did not consider the dip of the peatland boundary, assuming a vertical (90°) dip. Ultimately this method did not adequately define the peatland from the uplands resulting in open meshes and unclosed volumes. To overcome this, the polyline was used as a guideline and structural data points were placed manually at a dip of two to five degrees based on the uplands terrain (Figure 4.14). In areas with low relief a dipping angle of 2 degrees was used. In areas with higher topographic relief a dip angle of 4 or 5 degrees was used. This was informed by the lithological information from drive-point piezometers.

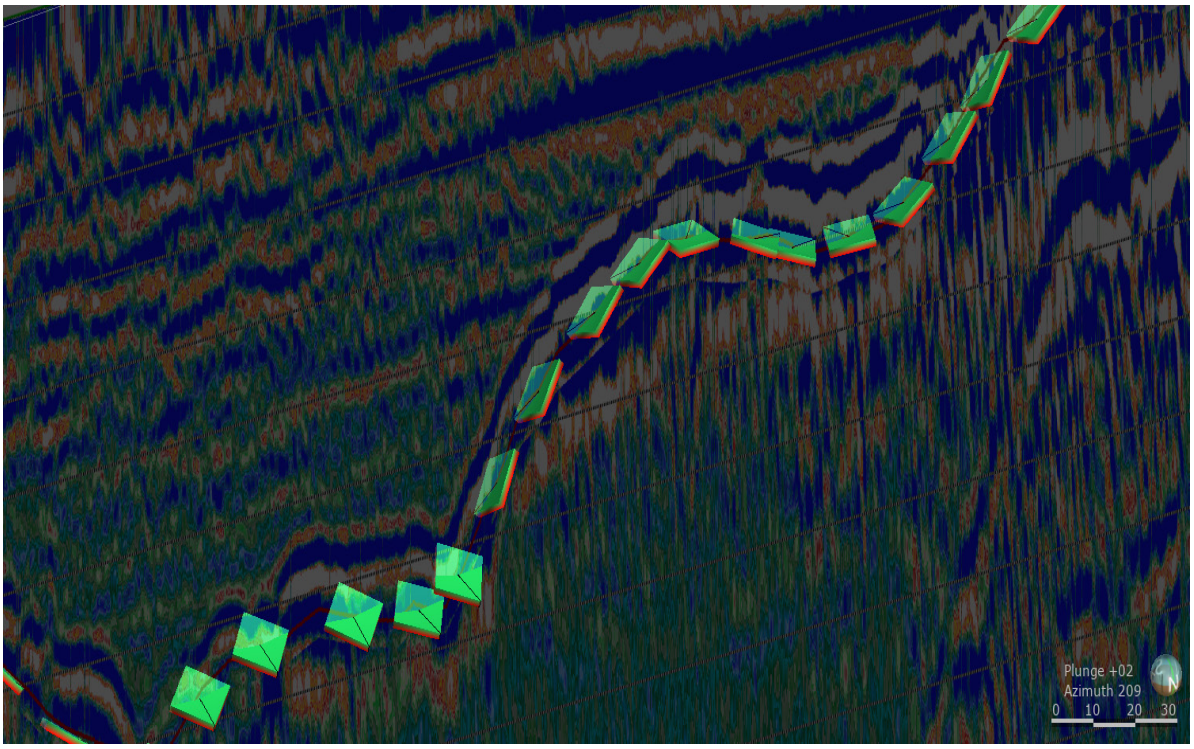

Figure 4.11 Structural data points on GPR cross section in 3D space.

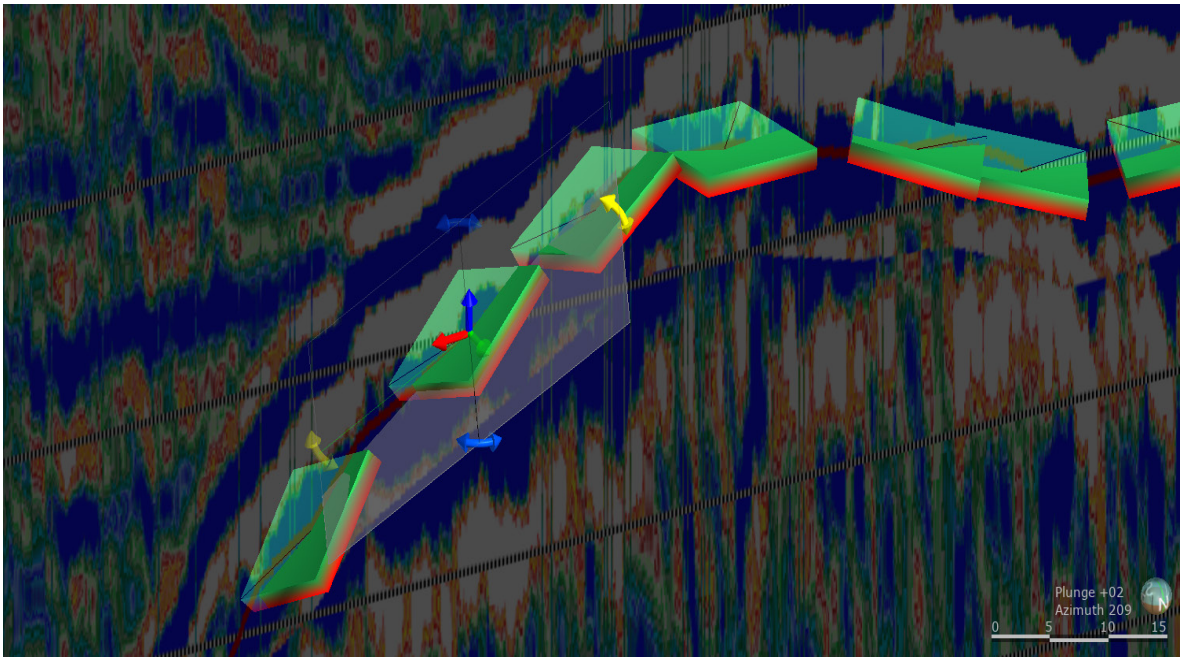

Figure 4.12 Structural data point controls on GPR cross section (yellow arrow - dipping angle, purple arrow - elevation, green arrow - northing, red arrow - easting, and blue arrow - azimuth).

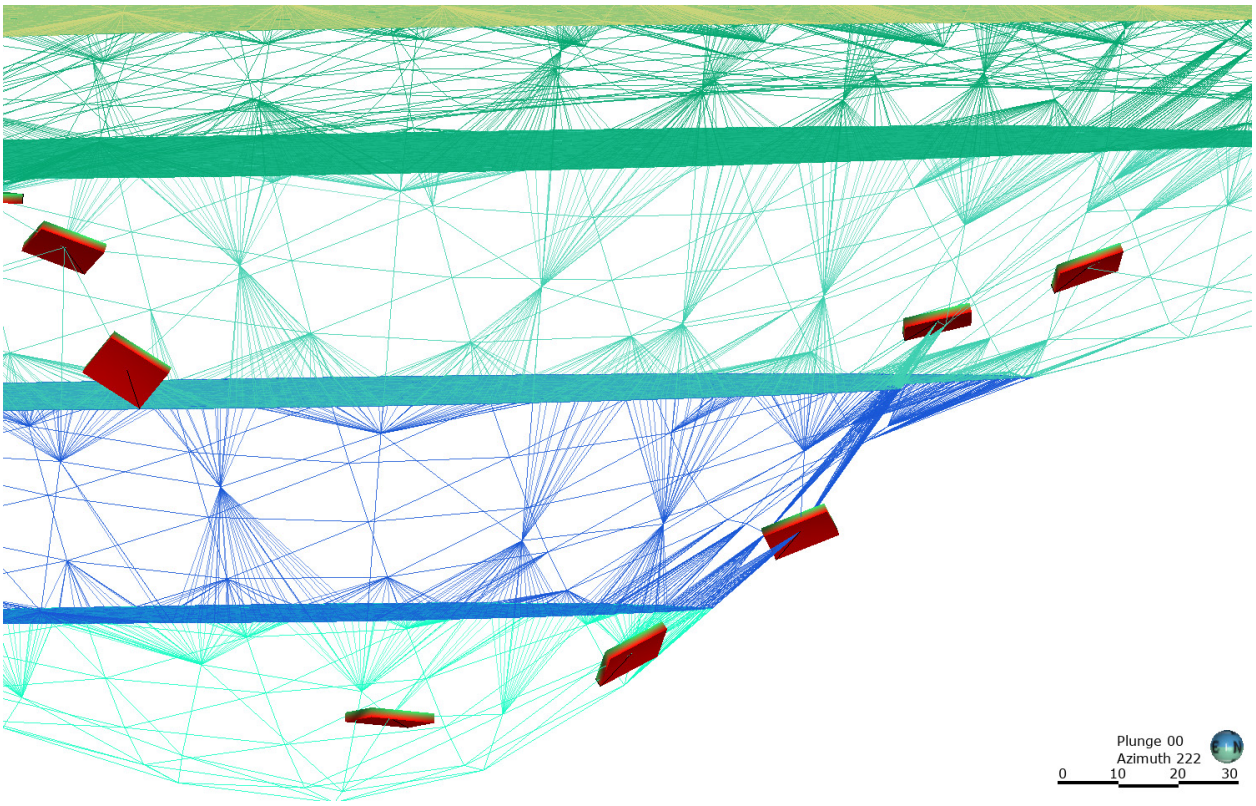

Figure 4.13 Structural data control points with resulting peatland volume face edges. Through a reiterative process control point dip was modulated to change the orientation of the face edges to tie structural points.

A *LeapFrogGeo* alternative method was used to triangulate a geological triple point contact by stacking structural data points at opposing dip direction and angles to define the upland from the substratum from the peatland. This was very labour intensive with over 100 upland control points and over 300 substratum peat boundary control points placed manually to create the peatland model boundaries (Figure 4.15 and Figure 4.16). The dipping directions were inserted manually and were primarily based on early conceptual models. As noted in Figure 4.17 the dipping directions were concentrated around similar values due to the similarity in the dip of subsurface peatland geometry. Compared to the peatland-upland interface the peatland-substratum interface had significantly more data from drillholes and GPR radargrams resulting in an abundance of associated structural modelling data. Statistical analysis of the structural data associated with the GPR radargrams show similarities between the mean dipping angles of the structural data points (Table 4.1).

Some outliers with steep dipping structural points were created to correct for complexities in the linear surficial intersection of the peatland and upland when creating meshes. This is a common method in *LeapFrogGeo* to fix shallow geological meshes with complex topographic constraints (pers. comms. Seequent, 2020). A maximum dip of greater than 20 degrees at GPR line DAT_0110 was needed to address modelling complexities in that area. The longest GPR line, DAT_0013, had the most structural data points (40) but a relatively lower co-efficient of variation and standard deviation compared to other shorter GPR lines. Shorter GPR lines like DAT_0105 and DAT_0117 needed more manual manipulation of the structural data points which increased the co-efficient of variation of those GPR lines.

Table 4.1 Statistics of structural data elements from peatland-substratum interface

GPR Line		***Count***	***Mean***	***Standard deviation***	***Coefficient of variation***	***Variance***	***Min***	***Lower quartile***	***Med***	***Upper quartile***	***Max***
0013	*dip*	*40*	*1.35*	*0.90*	*0.67*	*0.81*	*0.14*	*0.55*	*0.97*	*1.92*	*3.72*
0088	*dip*	*23*	*5.69*	*4.38*	*0.77*	*19.15*	*0.29*	*2.38*	*5.43*	*7.42*	*18.46*
0102	*dip*	*24*	*5.87*	*2.83*	*0.48*	*7.99*	*1.55*	*2.87*	*5.15*	*7.91*	*10.86*
0105	*dip*	*17*	*3.10*	*2.51*	*0.81*	*6.28*	*0.44*	*1.16*	*1.66*	*4.55*	*8.90*
0106	*dip*	*11*	*1.98*	*0.67*	*0.34*	*0.45*	*0.82*	*1.52*	*1.98*	*2.63*	*2.96*
0110	*dip*	*8*	*12.29*	*9.13*	*0.74*	*83.32*	*2.63*	*3.05*	*8.44*	*20.44*	*24.69*
0111	*dip*	*5*	*4.01*	*2.72*	*0.68*	*7.41*	*0.54*	*2.77*	*3.37*	*5.87*	*7.50*
0112	*dip*	*41*	*3.99*	*2.54*	*0.64*	*6.47*	*0.60*	*1.26*	*4.46*	*5.78*	*11.14*
0117	*dip*	*17*	*3.79*	*3.15*	*0.83*	*9.91*	*0.30*	*1.38*	*2.66*	*5.29*	*11.33*
0118	*dip*	*9*	*6.97*	*1.61*	*0.23*	*2.59*	*4.28*	*6.30*	*7.86*	*8.06*	*8.53*
0123	*dip*	*8*	*4.27*	*1.73*	*0.41*	*3.00*	*2.76*	*2.78*	*3.95*	*4.33*	*8.20*
0125	*dip*	*11*	*5.16*	*0.83*	*0.16*	*0.69*	*4.01*	*4.76*	*5.23*	*5.49*	*7.03*
0126	*dip*	*16*	*4.67*	*2.54*	*0.54*	*6.43*	*0.20*	*3.41*	*4.21*	*5.71*	*8.93*

Figure 4.14 Structural Data of the Upland-Substrate Interface (polyline in green/red and resultant structural points in blue)

Figure 4.15 Opposing Structural Data Points (Substratum, blue and Uplands, red)

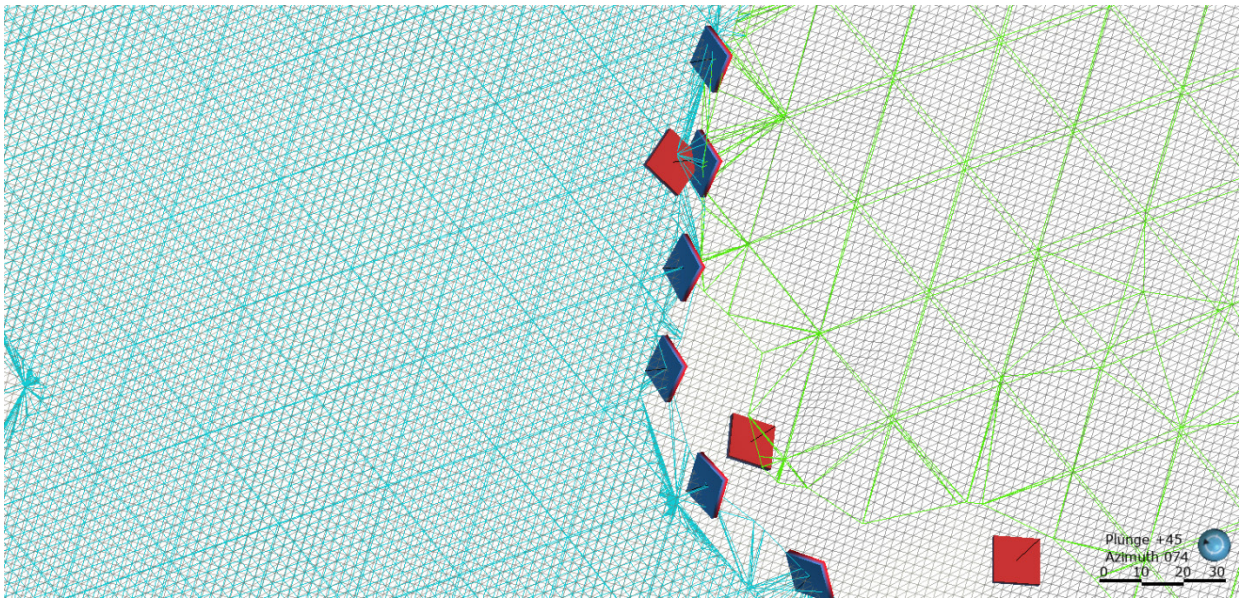

Figure 4.16 Delineating upland (green face-lines) from the peatland (blue face-lines) using structural data.

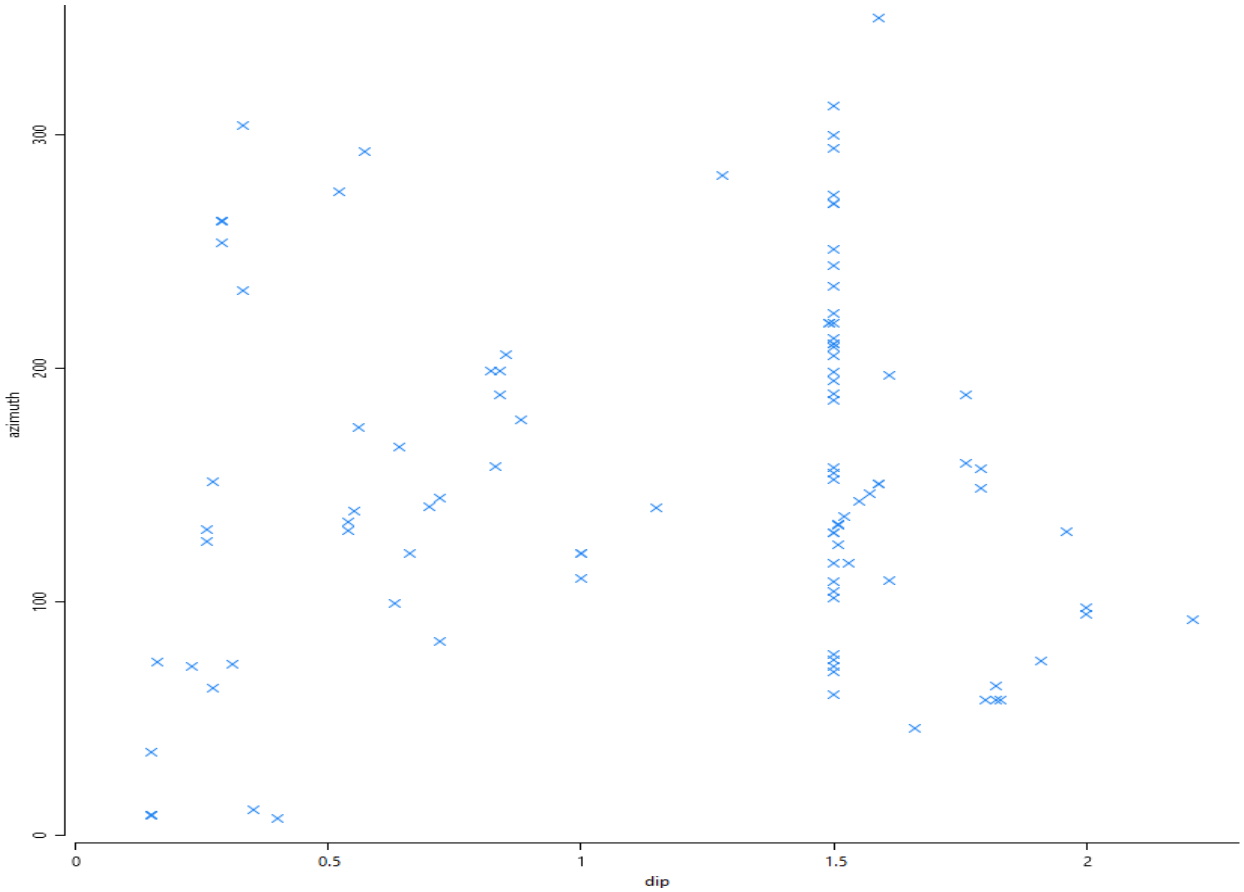

Figure 4.17 Dip and azimuth for Peatland-Upland interface structural control points

4.8 Meshes

Meshes are essential components in modelling to generate resulting geological volumes. They are used to define location, boundary, and geometry of surfaces that calculate the volumes, contours, and other gridded information. A mesh is a collection of vertices, edges, and faces, usually in the geometry of triangles or quadrilaterals (Figure 4.18).

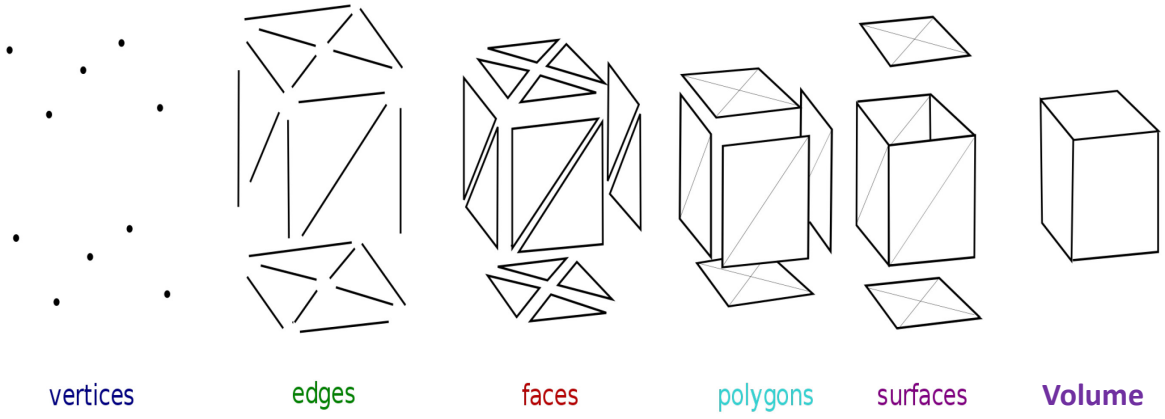

Figure 4.18 Elements of polygonal mesh modelling (accessed on Wikipedia under Creative Commons Attribution)

Meshes were created directly in *LeapFrogGeo* from gridded data imported from other programs such as *Golden Surfer software* and raster maps from QGIS The low-lying smooth areas are identified as wet fens, textured low lying areas are identified by dry fens, dense textured low lying areas are identified as bogs, and the conifer uplands abruptly define the low lying peatlands. Large flow lines are apparent in satellite imagery and are pronounced from the texture of the first reflections digital elevation mesh. These established flow lines are important elements of understanding peatland hydrology and the overall evolution of the peatland (Figure 4.19). Figure 4.20 shows a surface mesh created for the boundary between peatland and the substratum below, derived from structural modelling data, drive-point piezometers, and is clipped to the topography. Triangles are coloured by the dip of the triangle from zero to approximately 13 degrees. The areas of the highest dip angles are in the wet fen indicating a channelized system. Figure 4.21 shows the peatland and substratum boundary surface mesh is saddled in the upland mesh.

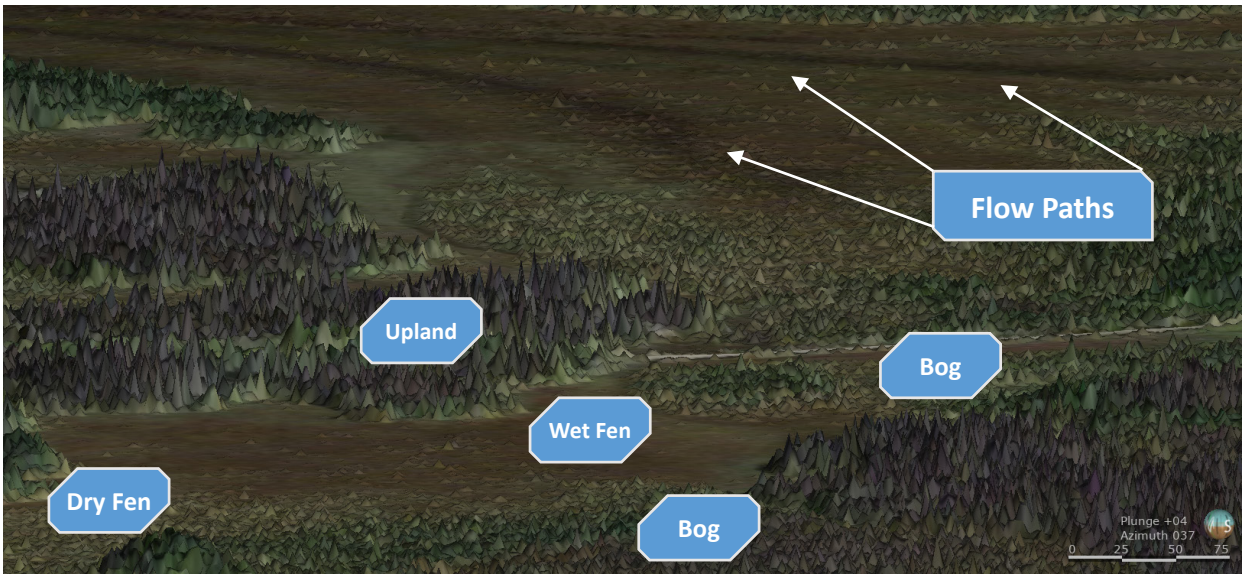

Figure 4.19 First reflection DEM with smooth faces showing hydrological features using imagery overlay. The texture of the DEM demonstrates ecosystem components of the study area, where wet fens have low surface roughness compared to dry fen and bogs which have the most surface roughness in low lying areas. Uplands are populated with conic features resulting from the conifer-dominated forest. Dark traces in the google satellite imagery are located in areas of less surface roughness indicating established shallow flow lines of mineralized groundwater and discharging away from the peatland area.

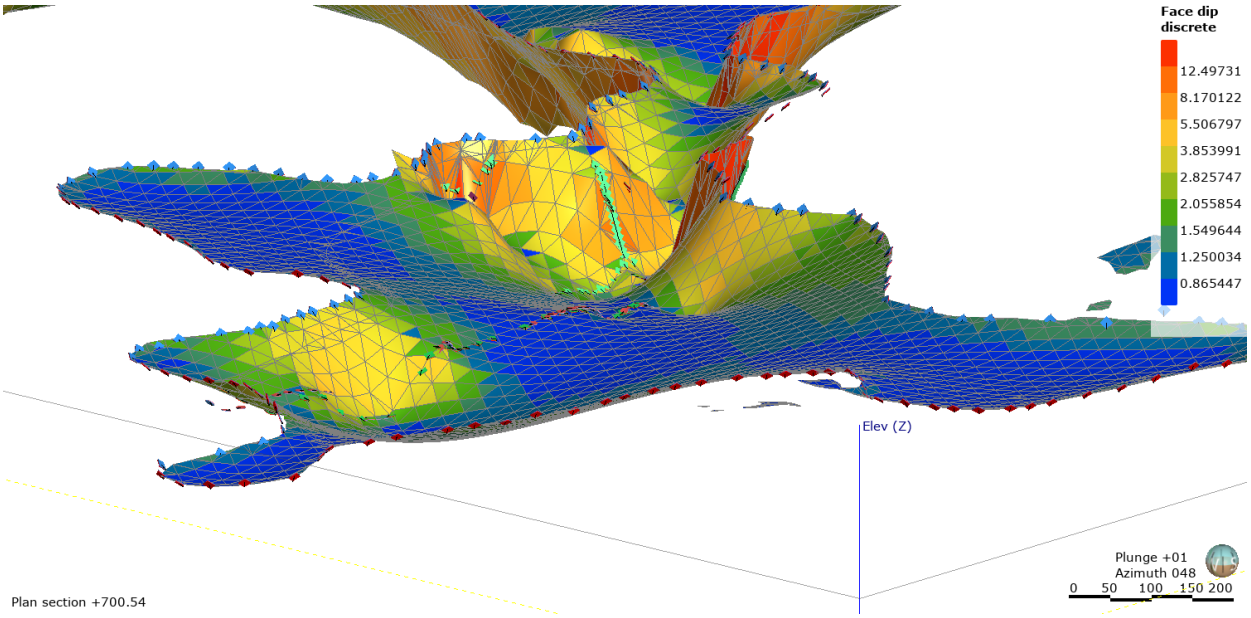

Figure 4.20 Surface mesh of peatland-substratum interface classified as dip direction in degrees with associated structural modelling elements displayed as diamonds with the blue side looking up and the red side looking down.

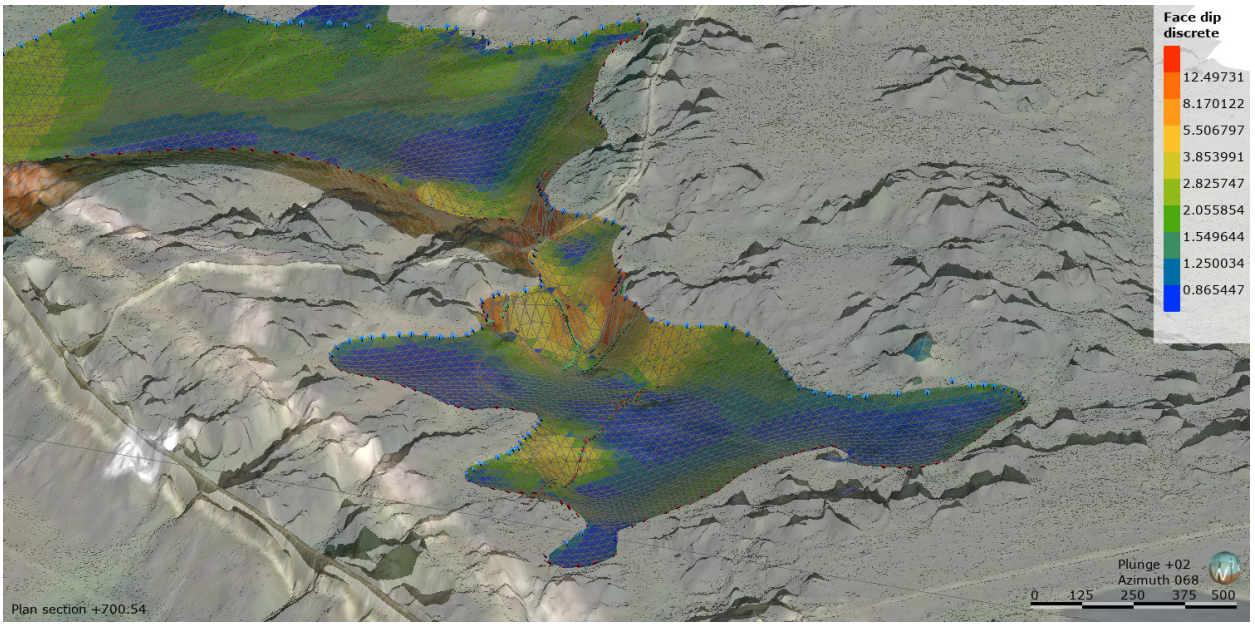

Figure 4.21 Surface mesh of boundary between peatland and substratum saddled in the uplands mesh

4.9 Geological Models

Geological models are outcomes from visualization of topography, lithological data, drillhole data, surface meshes, GPR data and GIS information serving as the foundation for future analysis.

Boundary

The limits of the geological model were defined by topography as the upper limit and a bounding box defining the maximum extents of latitude, longitude, and depth (Figure 4.22). The modelling boundary was chosen to capture the most important attributes of the study area and to avoid significant elevation change from the escarpment near the highway.

Lithologies

Lithology in the geological model was automatically generated from assigned lithology to drillhole data using depths determined in previous studies (Cherry, 2015; Küsel, 2014; Vallarino, 2014). The lithological units were generalized as upland, substratum, alluvium, and peatland. The peatland volume was categorized in 4 zones A through D, where A was the shallowest and D the deepest.

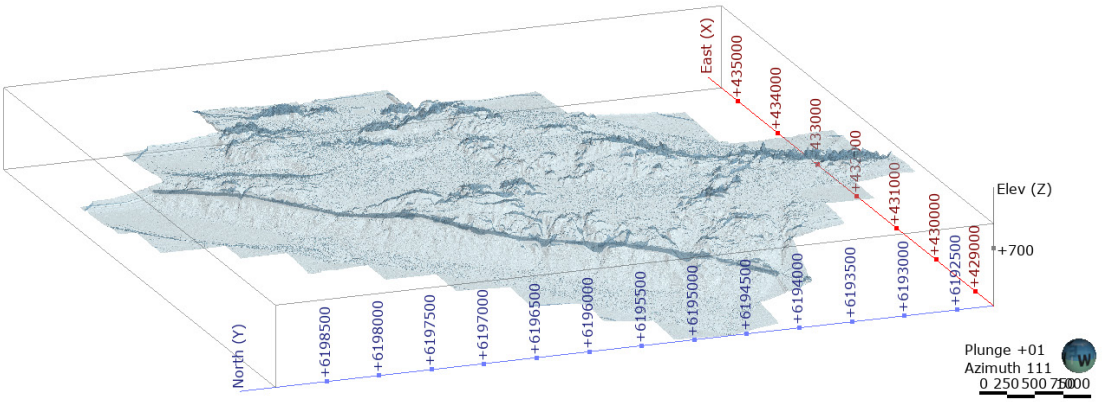

Figure 4.22 Geological model domain and bounding box shown in purple and LiDAR data acquisition extent shown in blue.

Surface Chronology

Surface chronology is the contact surfaces and the chronological stratigraphic order from youngest to oldest. A continuous peatland-substratum mesh was created. Snap displacement of peatland depths from drillhole lithology defined the mesh which increased confidence channelized geometry and areas without GPR data (Figure 4.23).

The mesh was clipped to the peatland-upland contact that was generated using topographic roughness to define the surficial extent of the peatland against the uplands (Figure 4.24). Without this clipping feature, resulting surface meshes would extend beyond peatland extents; therefore, clipping was an essential process to force the mesh to not spill over into the uplands. Snap displacement is generally used in resource mining modelling that forces geological models to consider drillhole data as priority surrounding fault meshes and other structural geology meshes. Using snap displacement with surficial topography for mesh clipping is uncommon, however this proved as an invaluable method to ensure that peatland meshes did not extend beyond logical boundaries into the uplands.

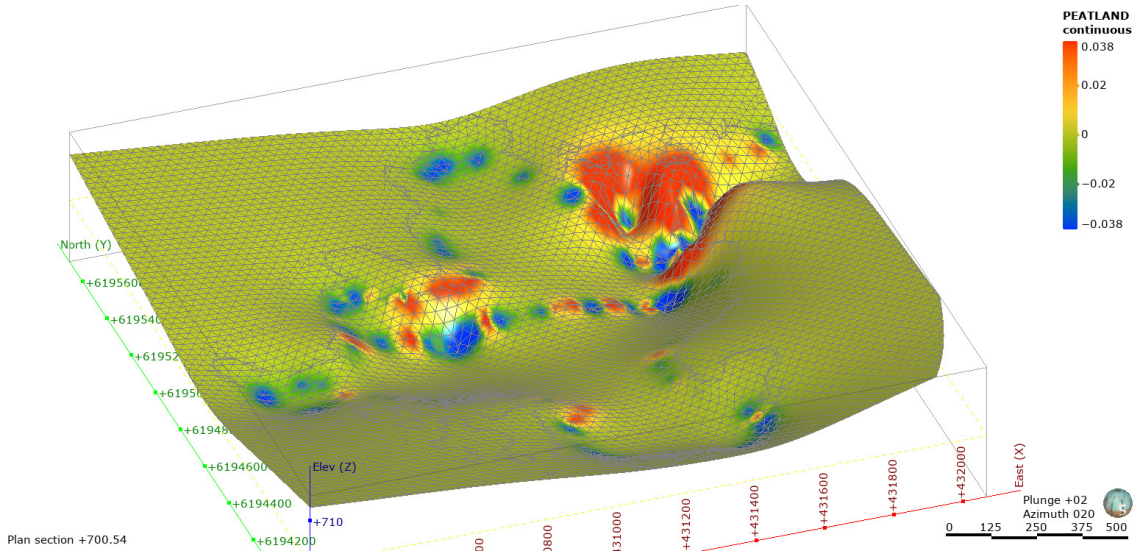

Figure 4.23 Peatland surface chronology displayed with snap displacement without clipping.

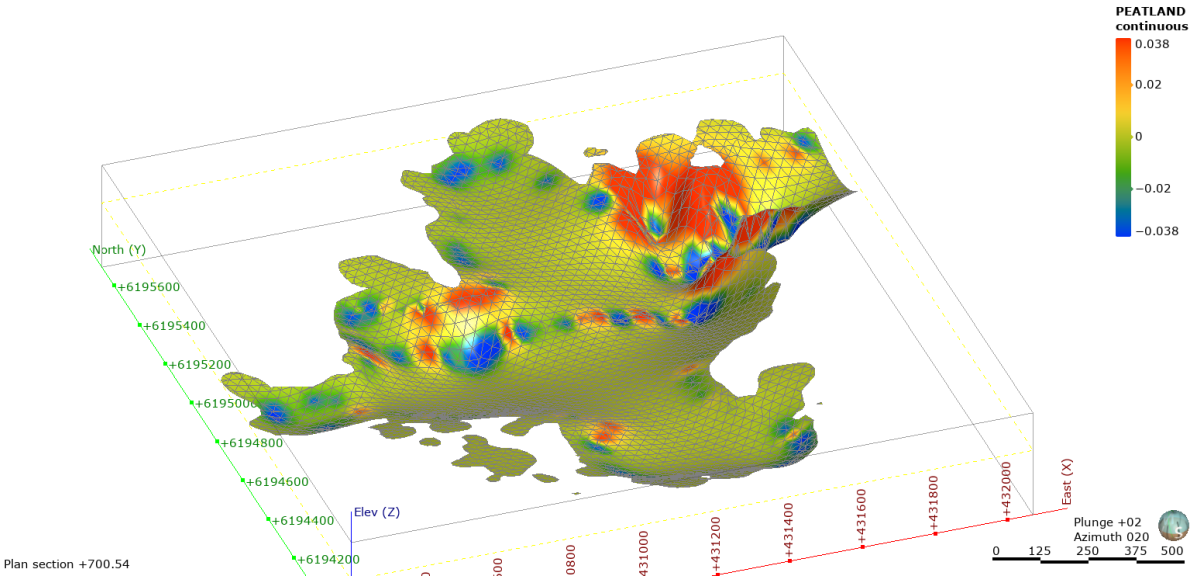

Figure 4.24 Peatland surface chronology displayed with snap displacement with clipping to determine extent to the uplands.

Output Volumes

Volumes are prime resulting output from geological modelling in *LeapFrogGeo* rather than input data. Resulting volumes cannot be changed after they are created, rather changes to structural and lithological data may result in changes once the model is re-run to create the volumes. This modelling technique, known as implicit modelling, is very powerful since changes in data result in updates to output volumes when new data becomes available.

Output volumes are 3D geometrical representations of lithological units or other geological surfaces and are named according to the defined chronology of the lithology. The peatland was modelled in one large continuous volume for use in geochemical numeric models (Figure 4.25) and in multiple parts (Figure 4.26 and Figure 4.27). Results from the geological modelling returned volumes for several peat horizons and estimated alluvium at the base of the fens (Figure 4.28 Figure 4.29, Figure 4.30, Figure 4.31, and Figure 4.32). Table 4.2 provides basic statistics on the peatland and alluvium volumes resulting from the geologic modelling.

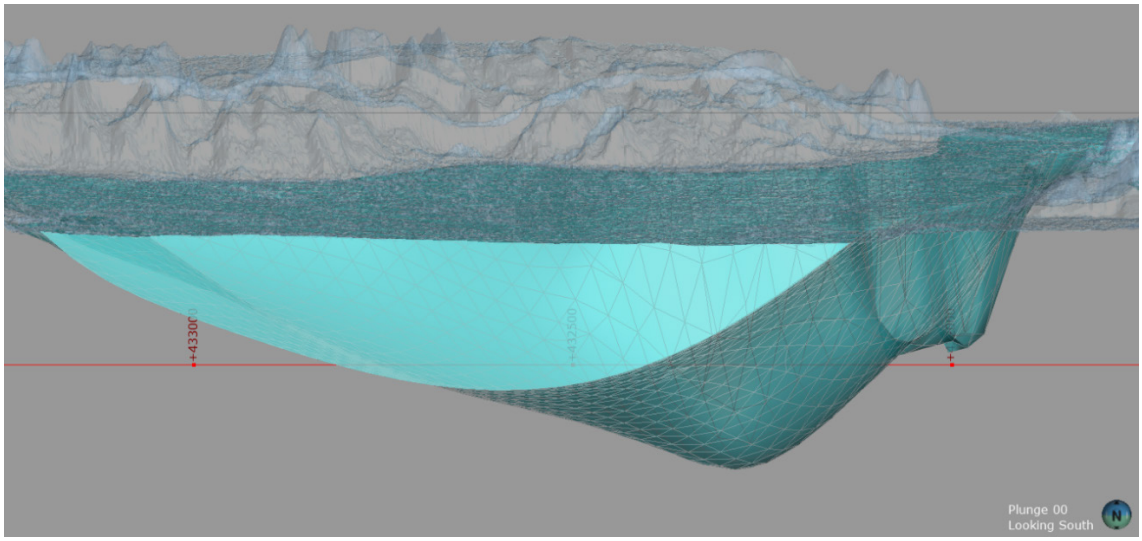

Figure 4.25 Aggregated peatland volume to provide constraint boundaries for geochemical interpolation.

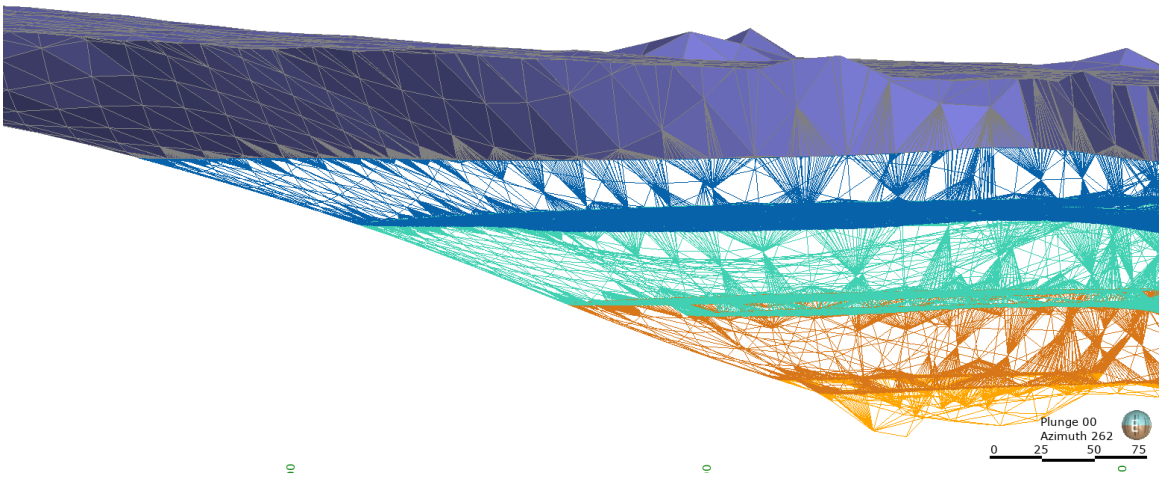

Figure 4.26 Wireframe of peatland volumes resultant from geological modelling

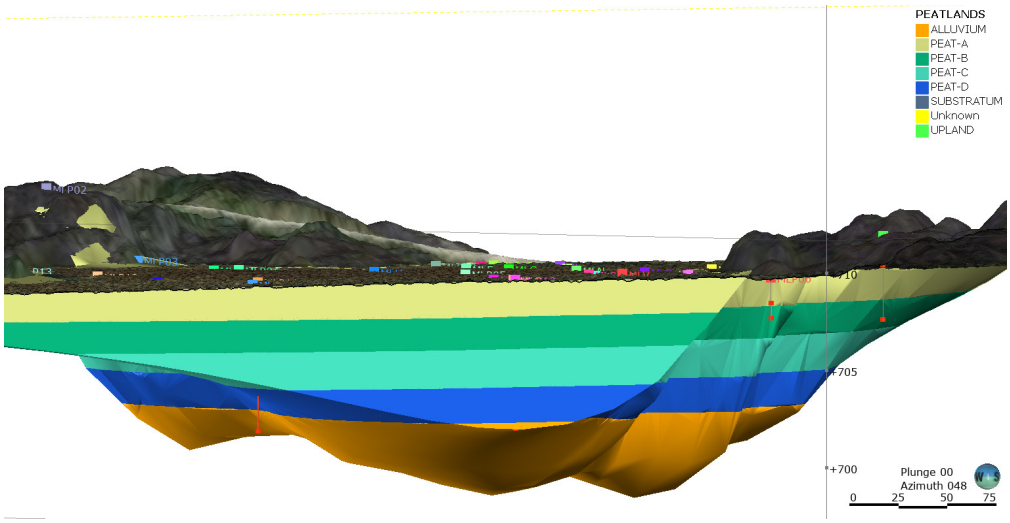

Figure 4.27 Peatland volumes with faces filling the wireframe.

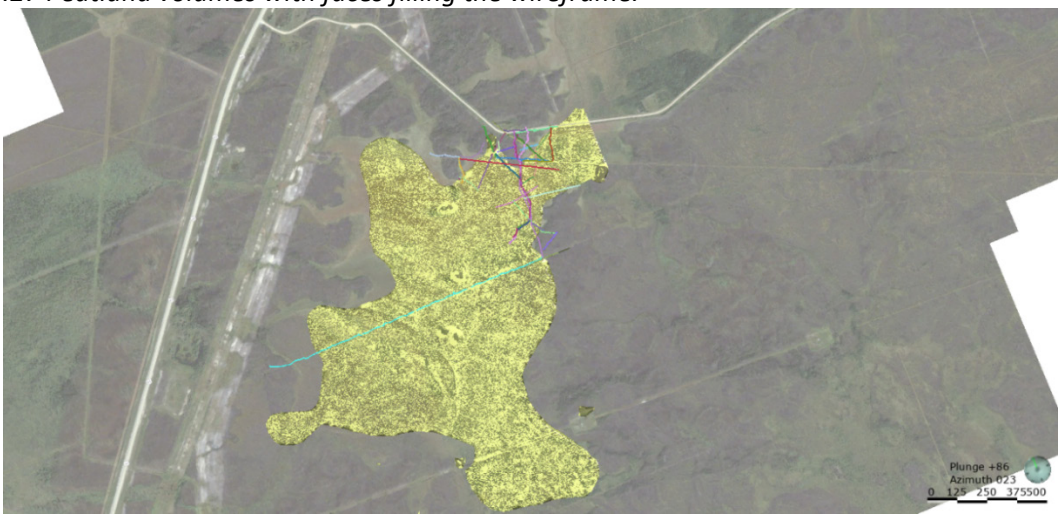

Figure 4.28 Plan view extent of geological volume - Peat A

Figure 4.29 Plan view extent of geological volume - Peat B

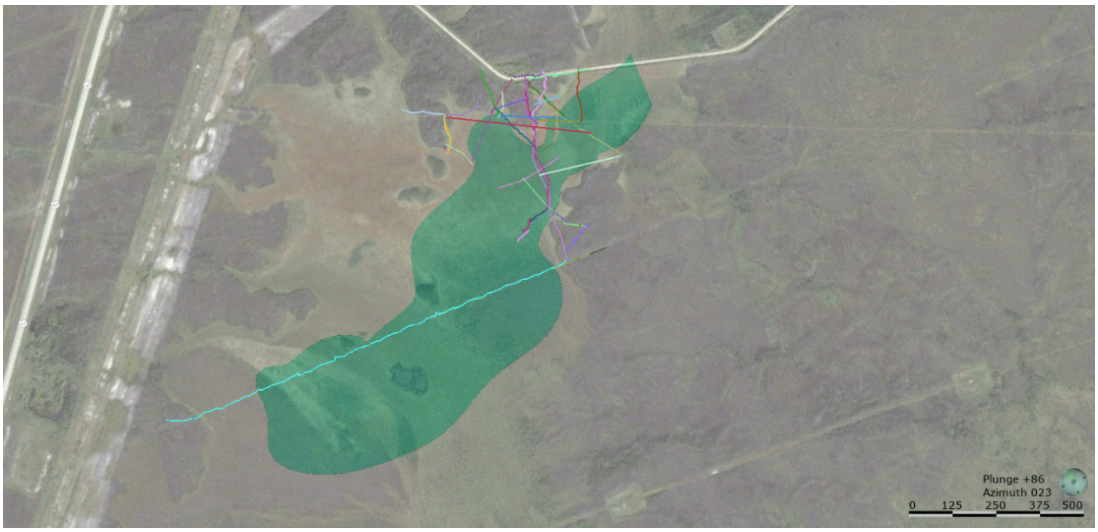

Figure 4.30 Plan view extent of geological volume - Peat C

Figure 4.31 Plan view extent of geological volume - Peat D

Figure 4.32 Plan view extent of geological volume – Alluvium

Table 4.2 Geological Model Peatland and Alluvium statistics

Item	Peat A	Peat B	Peat C	Peat D	Alluvium
Vertices	118,380	187,210	106,326	49,948	16,089
Triangles	236,736	374,412	212,648	99,884	32,166
Volume (m^3)	1,719,300	1,075,800	714,520	293,490	131,790
Area (m^2)	2,363,800	1,537,400	958,250	431,980	194,040
Volume/Area	0.73	0.70	0.75	0.68	0.68
Parts	6	2	1	3	3
Closed	TRUE	TRUE	TRUE	TRUE	TRUE
Consistent	TRUE	TRUE	TRUE	TRUE	TRUE
Manifold	TRUE	TRUE	TRUE	TRUE	TRUE

4.10 Numeric Geochemical Modelling

Numeric modelling in *LeapFrogGeo* interpolates between data using radial basis function (RBF) method. RBF was used with aqueous geochemistry data to estimate subsurface volumes between known data points. The interpolation was bound to peatland volumes calculated in the geological model. Geochemistry modelling was supported by an extension module called *ioGAS*, which allows easy data transfer of filtered geochemical datasets into *LeapFrogGeo*. Importing groundwater geochemical parameters into ioGAS allowed for data filtering, averaging, and statistical analysis. Averaging from multiple years of data for each location interval was completed for numerical modelling.

Data sourced from the ioGAS database were interpolated within the peatland boundary constraints using numeric modelling. A linear interpolant method with a constant drift (averaging drift) specified the interpolation between points in a weighted average rather than a linear regression that when tested produced negative values. Five geochemical parameters of interest were interpolated using average concentrations from sampling events from 2011-2014 from all available locations within the peatland. These included dissolved ammonium (Figure 4.33 and Figure 4.34), dissolved inorganic carbon (Figure 4.35 and Figure 4.36), dissolved organic carbon (Figure 4.37 and Figure 4.38), dissolved Total Kjeldahl Nitrogen, tritium, and electrical conductivity (Figure 4.39).

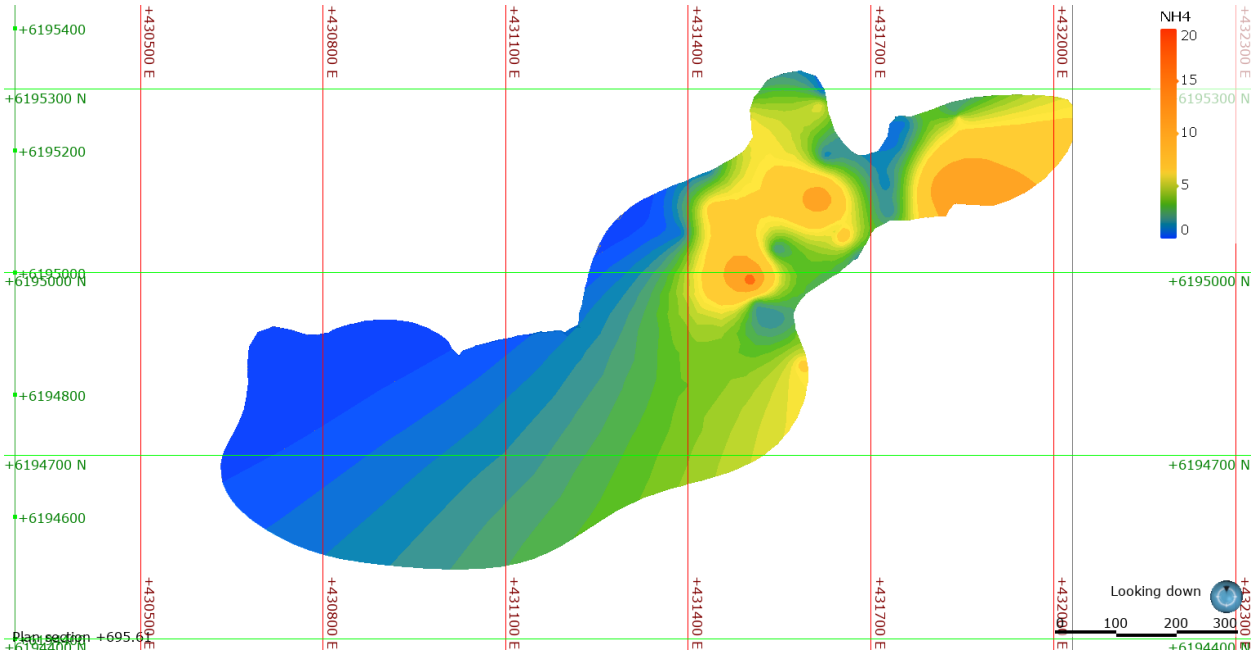

Figure 4.33 Plan view of numeric interpolation of high concentrations of ammonium (mg/L) in the Peat-D horizon.

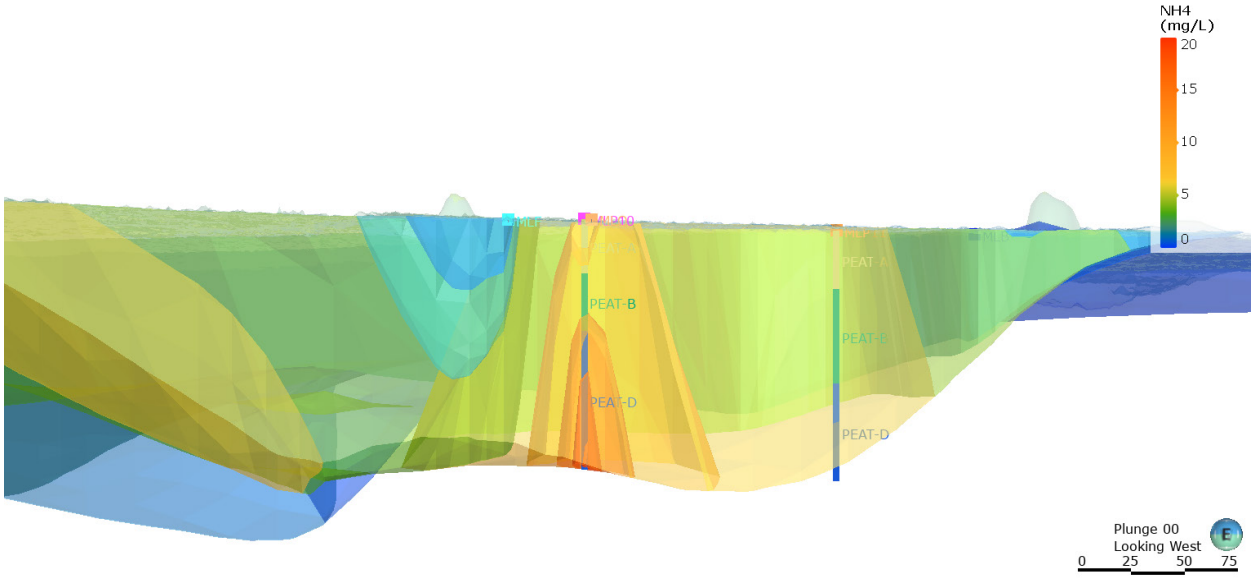

Figure 4.34 3D view of numeric interpolation of concentrations of ammonium (mg/L) in the study area showing high concentrations in lower reaches of the wet fen and lower concentrations in the bog areas.

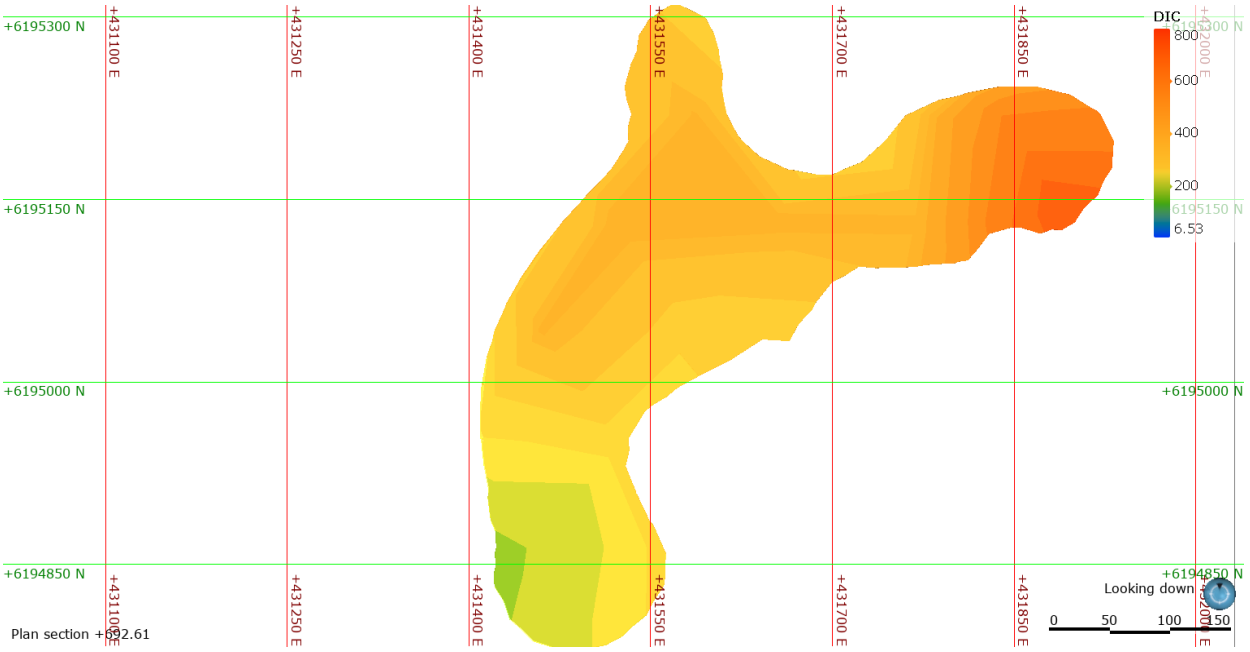

Figure 4.35 Numerical model interpolation of dissolved inorganic carbon (DIC) concentrations (mg/L) in the peatlands of the study area.

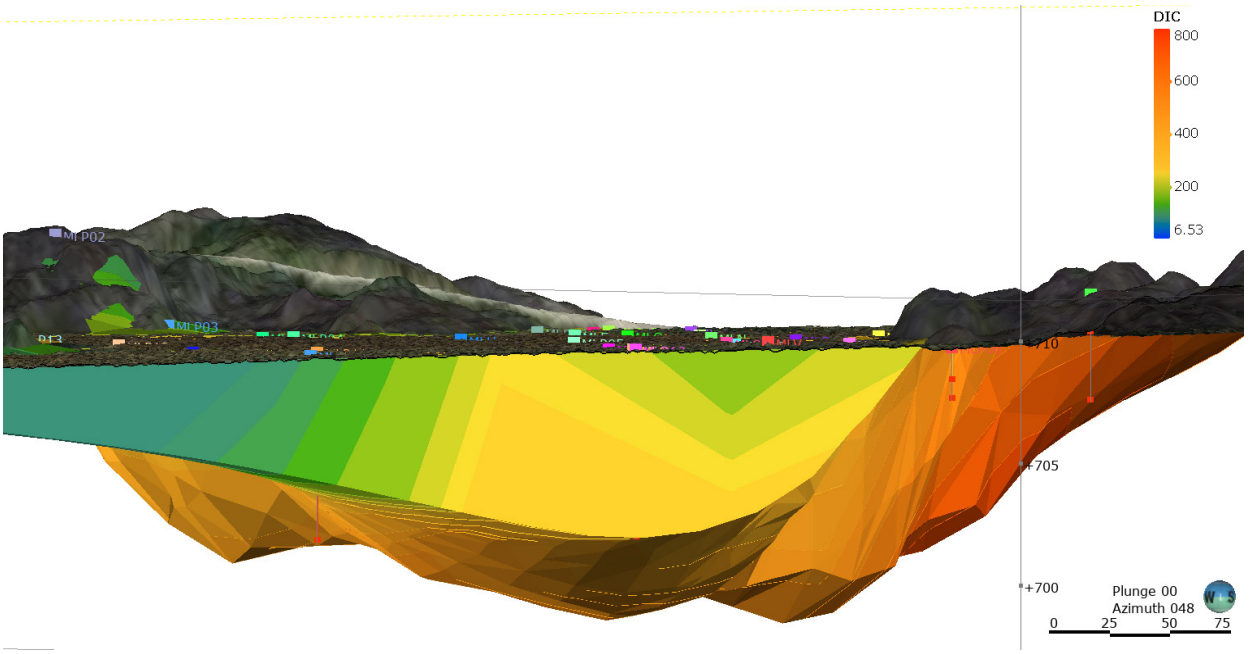

Figure 4.36 Numerical model interpolation of dissolved inorganic carbon (DIC) concentrations (mg/L) in the peatlands of the study area.

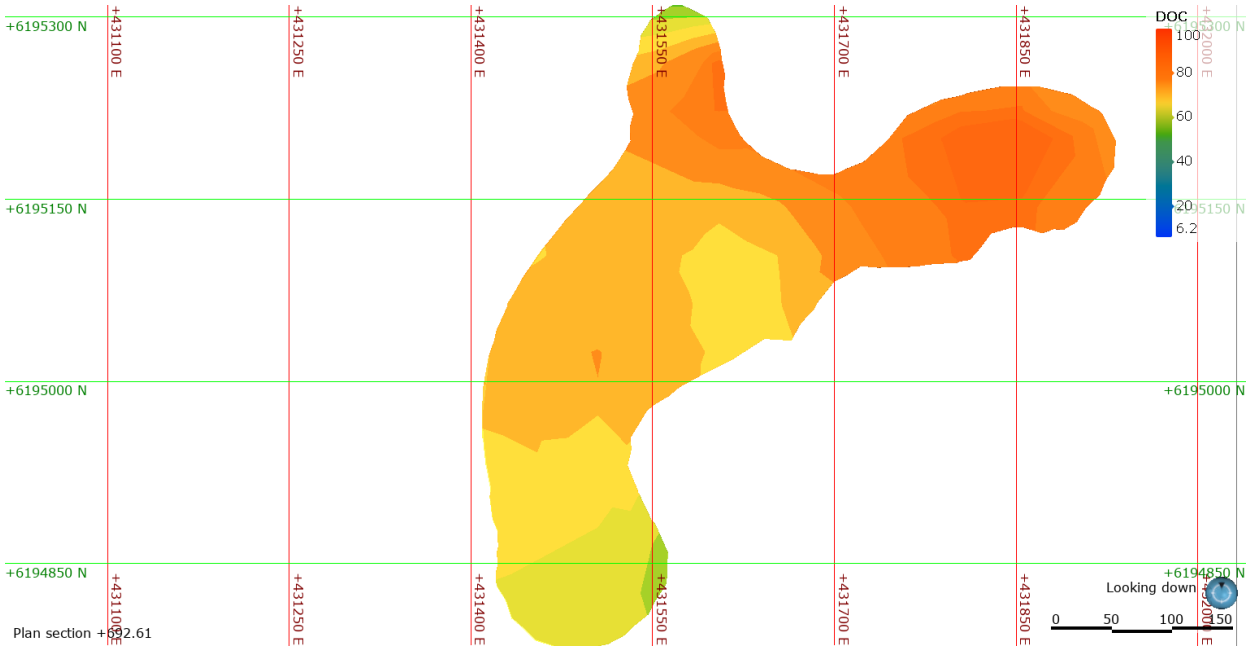

Figure 4.37 Numerical model interpolation of dissolved organic carbon (DOC) concentrations (mg/L) in the peatlands of the study area.

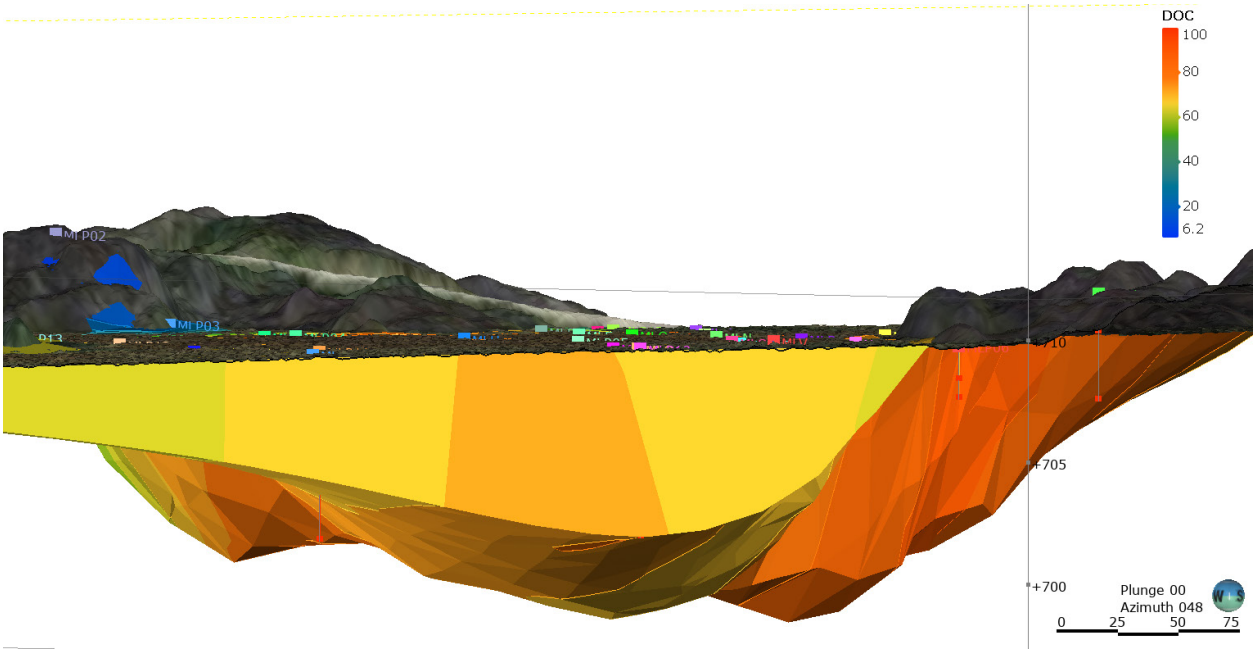

Figure 4.38 Numerical model interpolation of dissolved organic carbon (DOC) concentrations (mg/L) in the peatlands of the study area.

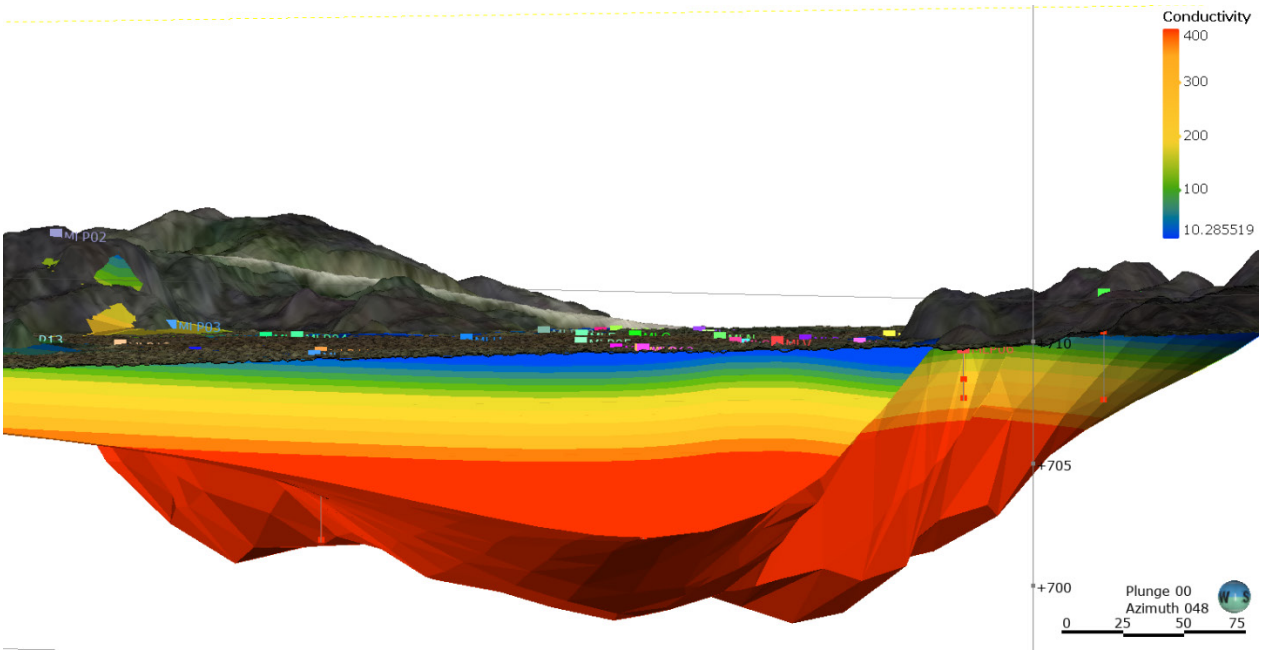

Figure 4.39 Numerical model interpolation of electrical conductivity (EC) concentrations (microsemens per centimetre) in the peatlands of the study area.

4.11 Combined Models

Combined models facilitate the combination of many volumes to create a cohesive model. This project did not use this method but rather took a different approach by creating a model within a model. A large undifferentiated peatland model was defined by general extents. A smaller model using GRP-derived structural data extents were created using the larger undifferentiated model as a modelling boundary. Figure 4.40 shows the initial conceptualization geologic model that extended to the entire peatland basin. Since the northern half of this undifferentiated model did not have associated GPR or hydrological data, the boundary for the smaller geological model was constrained near the access road delineating the northern extent of the detailed model.

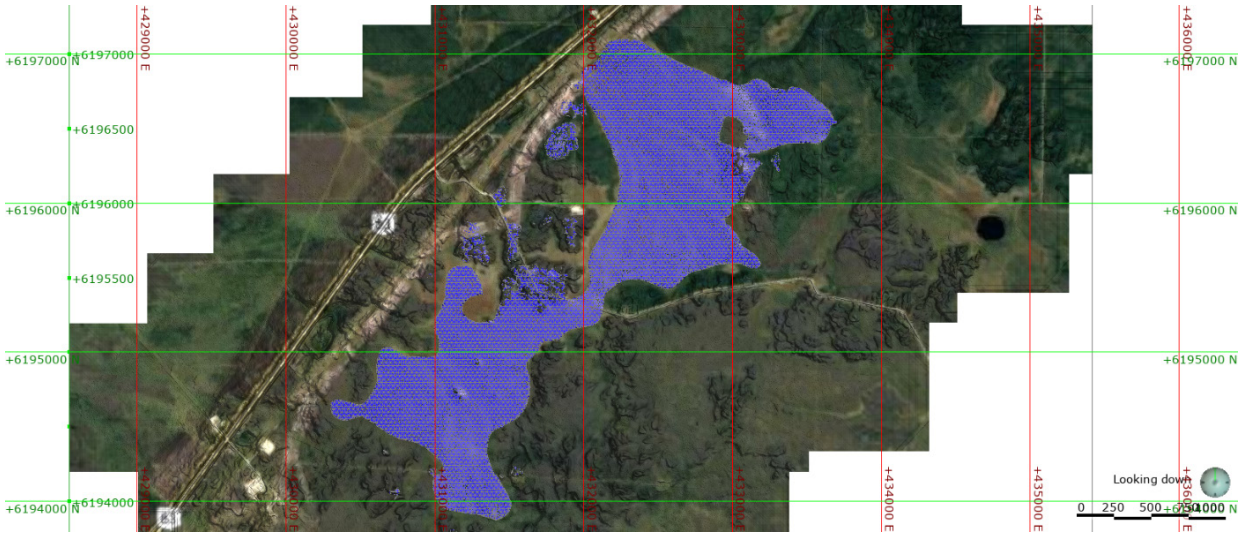

Figure 4.40 Large conceptual, undifferentiated peatland geological model.

4.12 Hydrogeology

Groundwater flow direction was calculated using existing groundwater elevation data in the shallow peatland (acrotelm, <1.5 mBGL, Spring 2014, Figure 4.41) and deeper peatland (catotelm, >3.0 mBGL, Spring 2014, Figure 4.42) using three-point problem method (US Environmental Protection Agency, 2014). The horizontal gradient in the acrotelm was 0.005 m/m and in the catotelm was 0.006 m/m. There was sluggish downward vertical flow within the peatland reported by Vallarino (2014) with a seepage flux in the bog from $1x10^{-8}$ m/s and $1x10^{-9}$ m/s in the fen. From Vallarino (2014), the geometric mean of the hydraulic conductivity in the acrotelm was $5.5x10^{-8}$ m/s or approximately 2 m per year and the catotelm was slower at $1x10^{-8}$ m/s or approximately 0.3 m per year compared to the uplands from $1x10^{-6}$ m/s to $1x10^{-7}$ m/s (30 to 3 m/year) . The peatland cross-sectional area discharging to the north was approximately 200 m wide by approximately 2 m depth in the acrotelm and approximately 5 m depth of the catotelm resulting in Darcy discharge of approximately 3.5 m^3 per year and 2 m^3 per year, respectively.

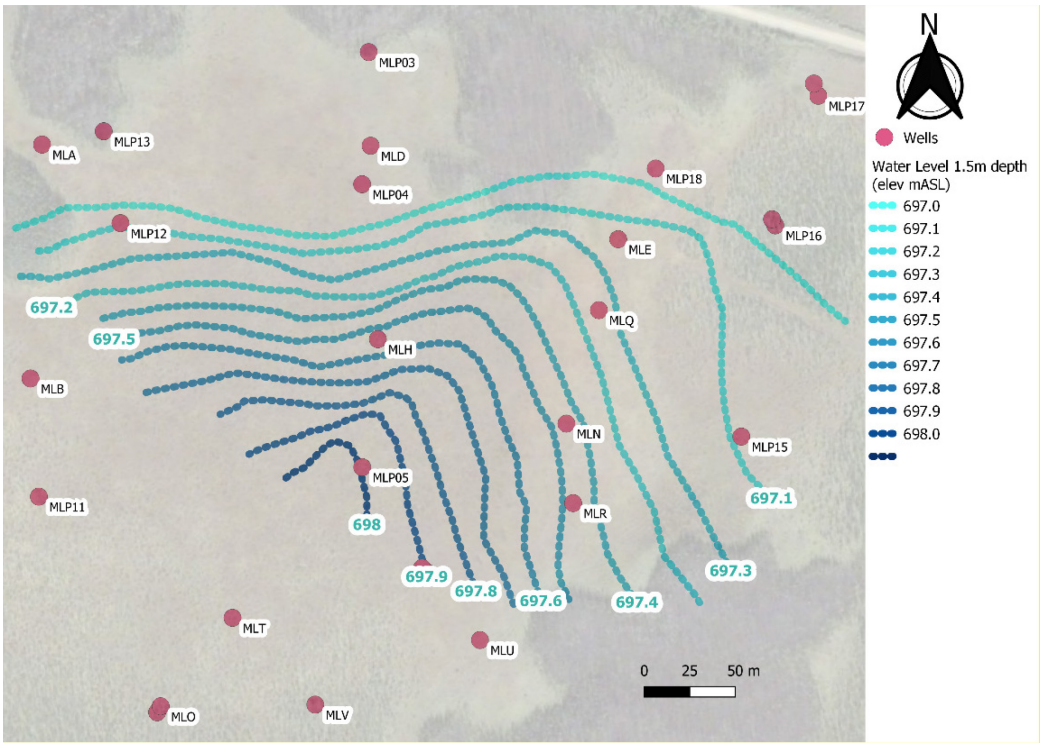

Figure 4.41 Groundwater hydrostatic pressure labelled in m ASL and flow direction in the acrotelm layer (<1.5 mBGL) calculated based on sampling data from spring 2014.

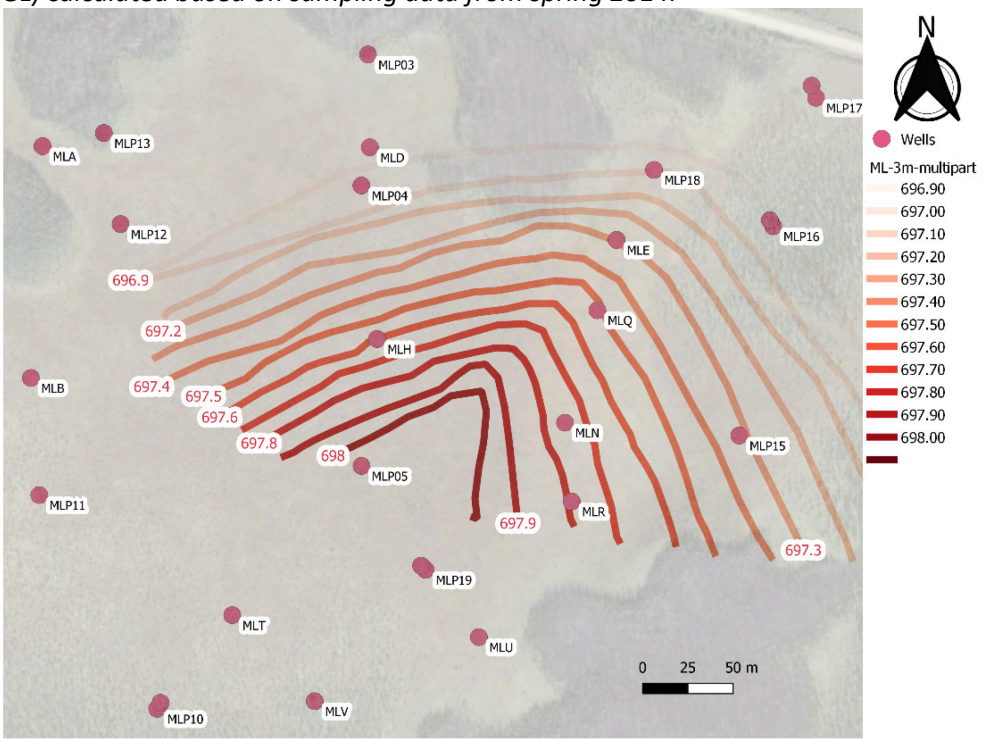

Figure 4.42 Groundwater hydrostatic pressure and flow direction in the catotelm layer (>3.0 mBGL) calculated based on sampling data from spring 2014.

4.13 Scenes and Movies

A scene is used to preserve the scene viewer and all associated shape list and element settings to recall. This allows for quick re-integration into the details of a workflow, to display as a rendered image, and to visualize the model in unique ways. Essentially a saved scene is a bookmark of the model. All of the figures produced in this thesis from *LeapFrogGeo* were from re-calling specific scenes that preserved the display of desired elements of the model, the legend, camera orientation, colour pallets, lithology tables, and scene lighting. Since a scene is not a static saved copy of the model, it dynamically changes as the model morphs through the modelling process updating figures in real time. A scene was easily called up as data was updated to re-rendered figures to reflect those data changes. *LeapFrogGeo* models can be represented in a movie; where saved scenes act as chapters in storyboard. Changes to the saved scenes are updated dynamically in the storyboard and will change with the project until a movie file is rendered. Movies were useful in saving interim modelling outcomes by rendering saved scenes to disc. Like a notebook, they provided a record of the reflected changes on modelling process.

4.14 Cross Sections and Contours

One of the essential processes in this project was the import of non-georeferenced GPR radargram cross-sections exported from RadExplorer into *LeapFrogGeo*. GPR bitmap image radargram cross-sections were inputted by providing x, y, z values for three markers on the 2D section. GPR sections were generally long and shallow and the vertical exaggeration of GPR lines differed across the site (perhaps a processing oversight). To overcome this challenge, georeferenced data for the markers were directly selected from the model and attributed to two horizontal endpoints of the GRP radargram cross-section. Figure 4.43 and Figure 4.44 demonstrate the topographical trace of the GPR 0118 marker (yellow square and green circle) on the digital elevation surface mesh to collate x, y, coordinates from the GPR-GPS and elevation (z) attributes from LiDAR derived DEM to the GPR cross-section image. Contours were created from the non-differentiated peatland volume , with a spacing of 0.5 m and no offset. Contact contours were used as an inspection tool for determining issues in surface meshes when and to identify areas of the model where the surfaces were not closing.

Figure 4.43 Plan view selecting location markers for import of GPR cross-section.

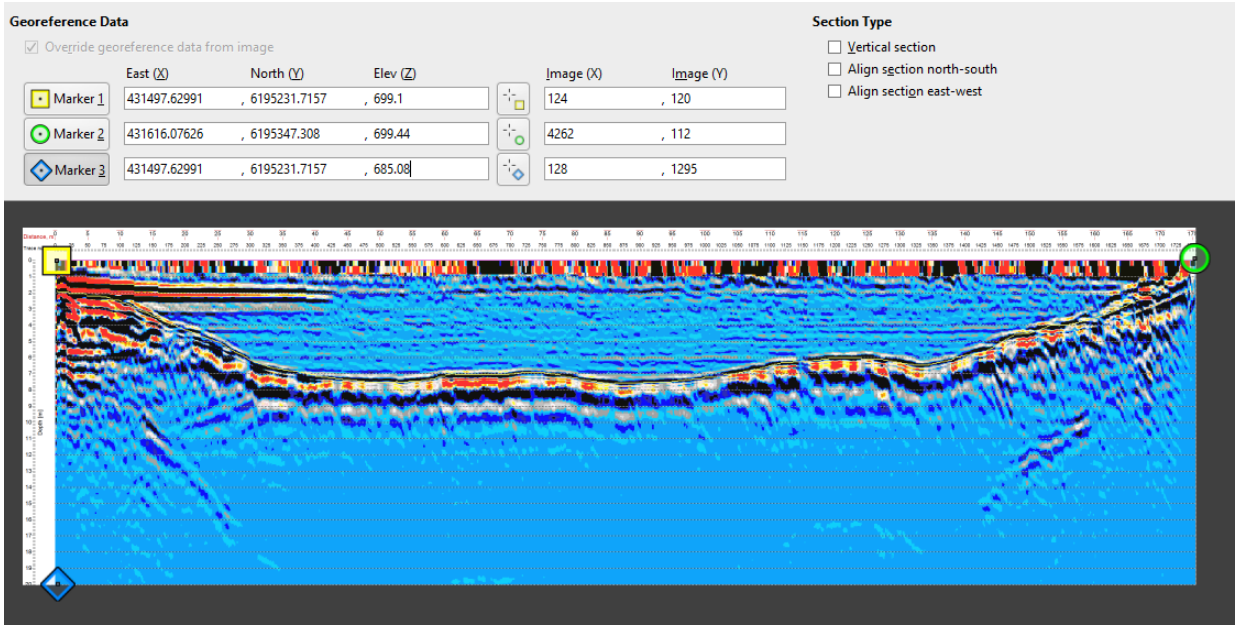

Figure 4.44 Processing GPR radargram bitmap image cross-sections in LeapFrogGeo using coordinate markers to assign spatial georeferenced and depth

4.15 Colourmaps and Colour Gradients

Colourmaps are one of the more important visual parameters of the modelling process and many were developed for a variety of purposes. Single colour displays were used to classify one colour to a particular element. For example, peat volumes were given discrete intervals of one colour that were assigned to a lithological code colour. For more complex classifications like elevation, intervals were determined by several modes including quantile, equal spacing, progressive, and logarithmic. In most cases the quantile mode was used (Figure 4.45)

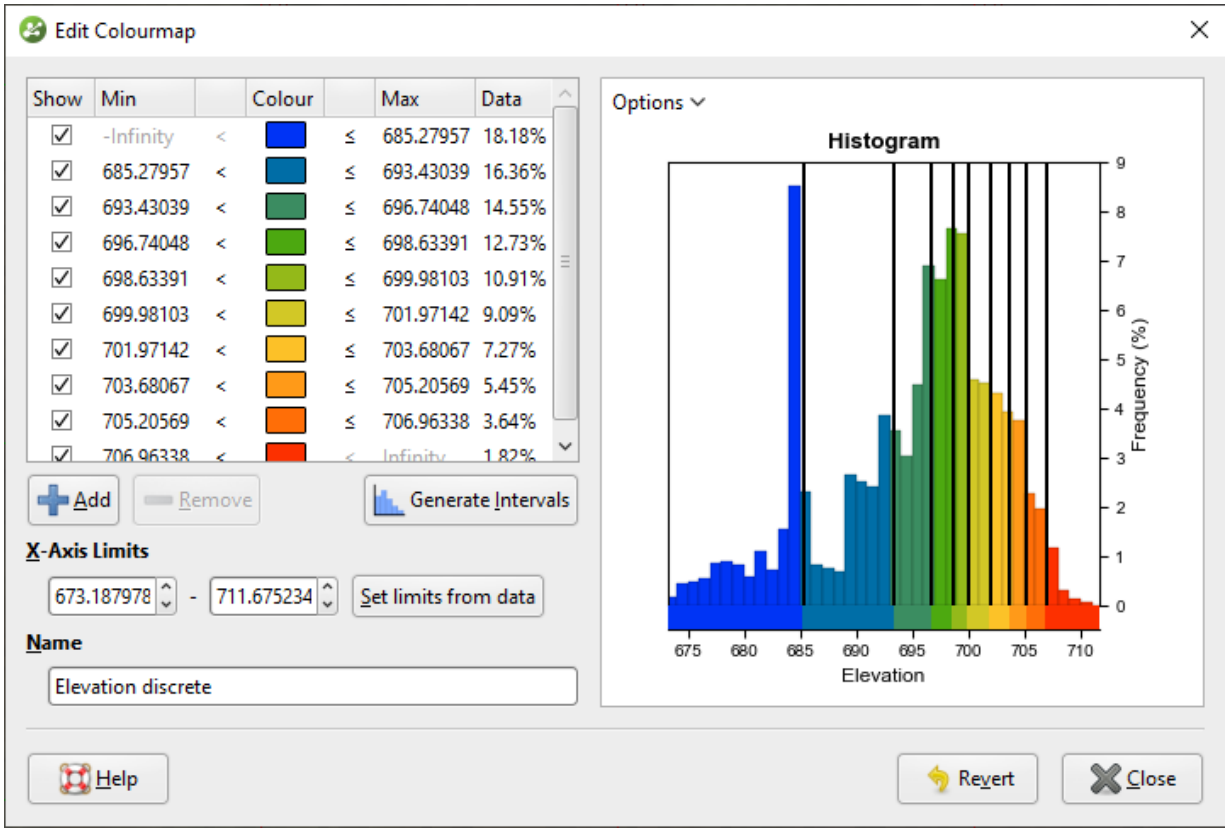

Figure 4.45 LeapFrogGeo Colourmap editor showing quantile mode.

5. DISCUSSION

Investigation of aquifers and groundwater dependent ecosystems have long been contingent on conceptualization as a precursor to numerical calculation (Robins et al., 2005, Figure 4.1). In this study, conceptualizations were developed considering existing methodologies that utilized 3D hydrogeological frameworks as a coherent integration of multiple datasets (Chen et al., 2012). Paradoxically, the determination of 3D models depends on one-dimensional and two-dimensional representations of the natural world that are subject to limitations (Flesch et al., 2018) and exhibit inherent spatial distortions (Kawakita et al., 2008). However, Robins (2003) states that these issues can be overcome and evaluated within a 3D visualization model with iterative assumptions to inform model development. This project followed that logic and developed implicit modelling techniques in *LeapFrogGeo* that created several conceptualizations of peatland depth and geometry from structural data estimations from GPR radargrams, LiDAR-derived digital elevation, and hydrogeological data.

Implicit modelling uses computer algorithms and machine learning from input data in a predictable framework to create scientific models with dynamic and intelligent interpolation to automate formation of surfaces and volumes (Barthel & Banzhaf, 2016; Bizhanimanzar et al., 2018; Frei & Gilfedder, 2015; Wijesekara et al., 2014). Implicit models are non-destructive representations that evolve with data updates in a reiterative process. The main benefit of implicit modelling is the ability to dynamically compare models, update models with emerging data, test conceptualizations quickly, and perform multiple life-cycle analyses (Fallis, 2013). *Explicit modelling* is a traditional gridded method of modelling defining features and structures from cell to cell within a static wireframe (Murphy et al., 2007). Similar to an engineering drawing process, explicit modelling characterizes data with the intention to create one instance of the conception. Static deliverables are limited in determining dynamic geoscience environments with influxes of updated data and evolving knowledge of the system. This project used explicit modelling to create a downscaled topographic grid in Golden Surfer software, however the majority of the modelling in this project was implicit in *LeapFrogGeo*.

Implicit modelling was helpful in satisfying oddities from geological constraints and topographic complexities by learning from the entire data framework and adapting in near real-time to additions of new data. This facilitated an iterative process by placing a few selected structural data points on key locations onto the GPR radargram cross-sections to develop a basic block-type conceptualization. Model definition and accuracy was increased as structural data points were modified and new ones added to refine the peatland geometry between GPR radargrams. Implicit models tend to be generalized and lacking detail in comparison to explicit models; however, increasing diversity and resolution of input data improves implicit modelling efficacy. Existing geological and geomorphological data from the Alberta Geological Survey and project-specific physical and ecological data from previous research, part of the Cumulative Environmental Management Association, was integrated into the hydrogeological framework and was used for model calibration (Poggio et al., 2020; Robins et al., 2005; Velasco et al., 2013).

Hydrogeological data from intrusive subsurface investigation of the study area, such as drive-point piezometer installation, peat coring, and borehole drilling, provided essential 3D data for modelling. These methods were time consuming, costly, and potentially produced some damage to the sensitive peatlands. LiDAR and GPR data were used to interpret the gaps between point-source hydrogeological data in the model. It was determined that the number of drive-point piezometers were over-represented for the purposes of calibrating lithological units to horizons in the GPR radargrams. Spatial distribution of drive-point piezometers was appropriate for the purposes of numeric geochemical modelling, however, expanded coverage is likely to improve the understanding of geochemical transport and hydrological flow dynamics in the peatland.

One of the primary difficulties in conceptualizing geographical geometries is that 2D representations, such as lithological cross sections, geophysical traces, geospatial data, and historical maps, are needed to represent a 3D environment.

Historically it was difficult to integrate hydrogeological modelling processes with geological frameworks and significant effort has been made to develop an integrated three-dimensional hydrogeological framework for conceptualizing, numerical modelling, and geovisualization (MacCormack et al., 2019). Assigning structural horizons is difficult due to an inherent 3D paradox of cross-cutting low-angle structures (Collettini, 2011). This project had many low-angle subsurface geological structures such as buried channels under wet fens that were cross-cut with single GPR radargrams (Figure 4.9). Due to unknown oblique angles and orientation of these features, dip angle and orientation of structural data were estimated and refined through the iterative modelling process. This paradox is one of the most significant challenges in geological geovisualization and is often overcome by increasing cross-sectional or drillhole data across obliquely dipping features to triangulate its trend in 3D (Flesch et al., 2018; MacCormack et al., 2019; Zou et al., 2013).

It was determined that the amount of GPR lines were too few for this project and the effectiveness of long-continuous GPR radargrams was underestimated in the ability to address complex structural modelling challenges. The longest GPR radargram that was collected was over 800 metres in length and took a considerable amount of time to collect. In hindsight these long-GPR lines were more suited for geological modelling and for understanding the subsurface geography of the peatland. Future considerations for GPR data collection are to integrate shorter radargrams for analysis in complex geomorphology that are cross-cut with long-regional ones.

GPR and LiDAR data independently provided useful information on the ecology of the peatland (Figure 5.1). LiDAR-derived first reflections digital elevation model mesh differentiated fens, bogs and uplands from microtopographic texture from the vegetation that inhabited them. Elevation differences of the crowns of large vascular plants, tamarack, spruce, and shrubs of the bogs and uplands generate unique microtopographic texture used to differentiate between wetland and uplands. Flow-lines, streams, rills, pools, and other peatland hydrology can be gleaned from first reflections LiDAR data, allowing for efficient regional analysis using remote sensing technique.

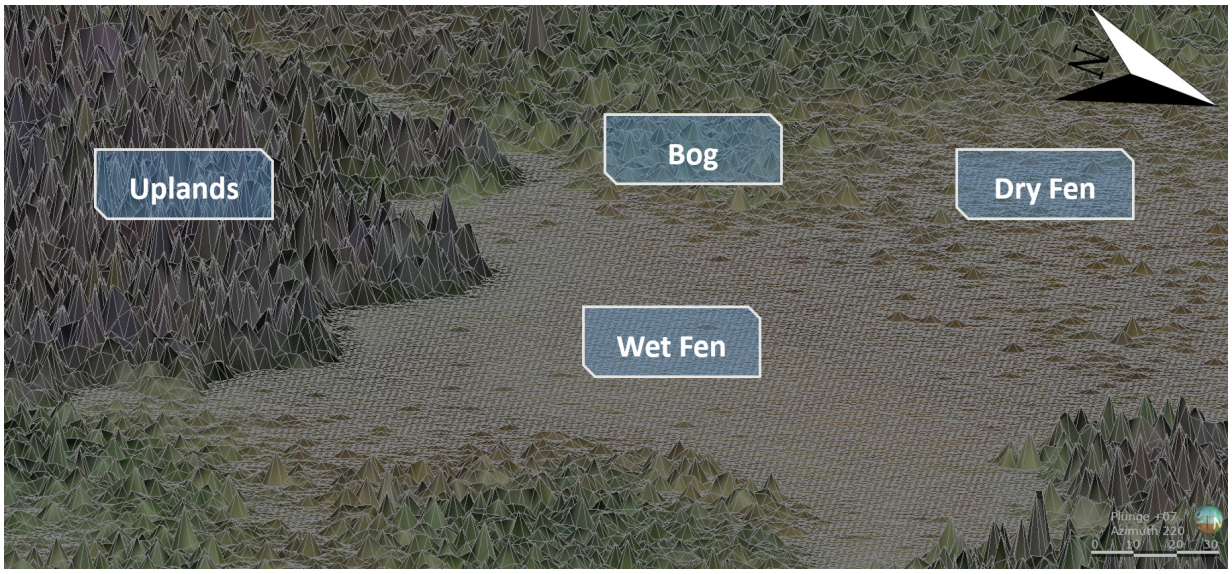

Figure 5.1 First reflection DEM mesh with triangulation showing ecological units from microtopographic texture

Water quality sampling data collected by Küsel (2014), Vallarino (2014), and Cherry (2015) were interpolated in 3D space using the undifferentiated peatland geological volume as a modelling boundary. Numeric modeling resulted in interval volumes generated for concentrations of chemical constituents that filled the peatland volume. These volumes were factored by an estimated porosity assumption of 90% from previous research (Turchenek, 1990) to calculate volumetric masses of dissolved inorganic carbon (DIC), dissolved organic carbon (DOC), ammonium (NH_4) and Total Kjeldahl Nitrogen (TKN) for the entire peatland area. The overall average concentration for NH_4 in the peatland was found to be 2.76 grams per cubic meter (g/m^3) of peat, 4.83 g/m^3 of TKN, 57.7 g/m^3 of DOC, and 182.5 g/m^3 of DIC.

The initial hydrological conceptualization that uplands hold a significant role in contributing source water to the peatlands from surface runoff was not proven although a hydrodynamic relationship between quaternary aquifers outcropping into the peatland may be significant. Geochemical investigations showed that nutrient movement within the peatland was stagnant and concentrated in deeper regions of the peatland (Figure 4.35).

The uniformity of electronic conductivity and other physical parameters in the acrotelm (Figure 4.40) generally supported that shallow peatland horizons mainly received water from direct precipitation. Evapotranspiration rates in fens are significantly high during the growing seasons (Bridgham et al., 1999; Sonnentag et al., 2009) and the majority of precipitation in the region is deposited in the summer creating water-limited ecosystems (Figure 2.6). Due to the highly stratified nature of peatlands there is minimal percolation of precipitation to deeper horizons. This concept was supported by comparison of the hydrostatic pressures of the shallower acrotelm that were lower in pressure than the deeper catotelm suggesting that there is an overall upward gradient of groundwater movement (Figure 5.2).

Early conceptualisations (Figure 1.1) created from hydraulic conductivities reported by Vallarino (2014) suggested that a moderate conductive upland aquifer contributes groundwater to the peat. As shown in Figure 5.3 the hydrostatic pressure surface intersects the peatland-upland interface at approximately 3 m below ground level which geologically supports the hypothesis that uplands hydrostatically connected to the peatland however discharge volumes is not quantified. Field inspections of the edges of the peatland along the uplands showed evidence of channelized water flow. This may indicate localized vertical movement of water from these shallow aquifers intersecting the sides of the peatland. Due to pressures within the peat and sluggish hydraulic conductivity stronger vertical gradients may exist at the peatland margins.

Another consideration is that stagnant peatland groundwater has less kinetic energy compared to more lotic upland sandy aquifers with higher hydraulic conductivity. Discharge of upland aquifer groundwater at the margins of peatlands may melt discontinuous permafrost during winter months creating preferential pathways for greater vertical groundwater movement than other areas in the peatland.

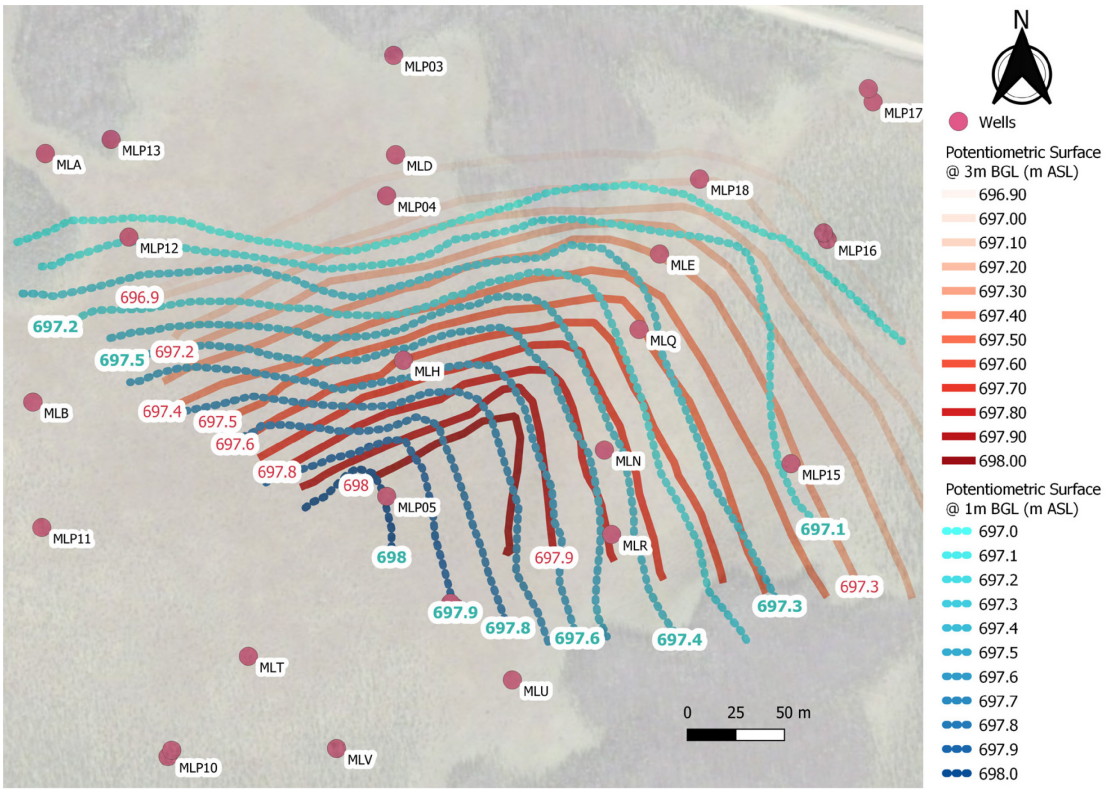

Figure 5.2 Groundwater flow across the study area with the catotelm in red hydrostatic pressure contours and the acrotelm in the blue, expressed in metres above sea level.

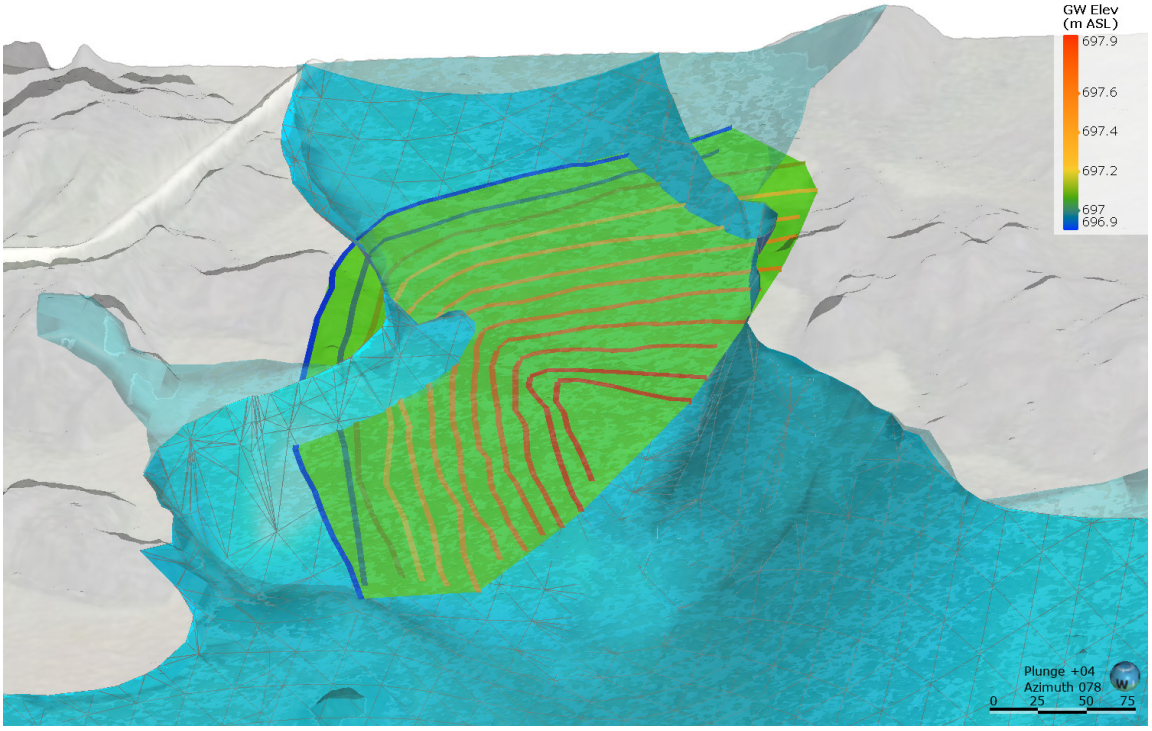

Figure 5.3 Catotelm hydrostatic surface mesh in green intersecting the edge of the peatland bottom mesh.

Ultimately the introduction of fresher and younger water either from precipitation or aquifer discharge to the peatland was depth-limited from analysis of tritium in the groundwater. Tritium is the only naturally occurring radioactive isotope of hydrogen containing two neutrons with a half-life of approximately 12.32 years. It is anthropogenically created in thermonuclear reactions and atmospheric atomic weapons testing (Happell et al., 2004). Prior to the proliferation of atmospheric atomic weapons testing in the 1950s and 1960s atmospheric concentrations of tritium were low, approximately 4 kg globally. Following the cease of atmospheric atomic weapons testing from the international *Limited Test-Ban Treaty* in 1963, it was estimated that hundreds of kilograms of tritium were left in the atmosphere from the tests (Michel et al., 2015). Since, tritium has been entering the water cycle and groundwater systems in significant amounts through precipitation, therefore waters with tritium concentrations are 50 years or younger (Gleeson et al., 2016).

Cherry (2015) described tritium distribution in the study area from project-specific geochemical sampling. Those data were interpolated in three-dimensions to relate to the groundwater flow of the peatland in this project. Figure 5.4 shows tritium concentrations and the relationship to the hydrostatic pressure of the catotelm. This demonstrates that groundwater at depth is older than 50 years and is most likely stagnant. It is likely that groundwater flow in the acrotelm and percolation of precipitation is not contributing significant volumes of younger water to depth. The distribution of low concentrations of tritium were limited due to the expense of sampling by avoiding problematic drive-point piezometers with questionable construction integrity. Negative tritium tests were found in several wells identifying older groundwater that was interpolated in 3D in the peatland (Figure 5.5). Generally, areas with low tritium concentrations correlated to areas of high geochemical accumulation in ecological zones identified at the surface as fen. From analysis of peatland architecture with electrical conductivity, alkalinity, and hydraulic conductivity, it is likely groundwater flow in fens is stable and transcends surface water divides to provide an essential hydrological service defining fens as groundwater-dependant ecosystems.

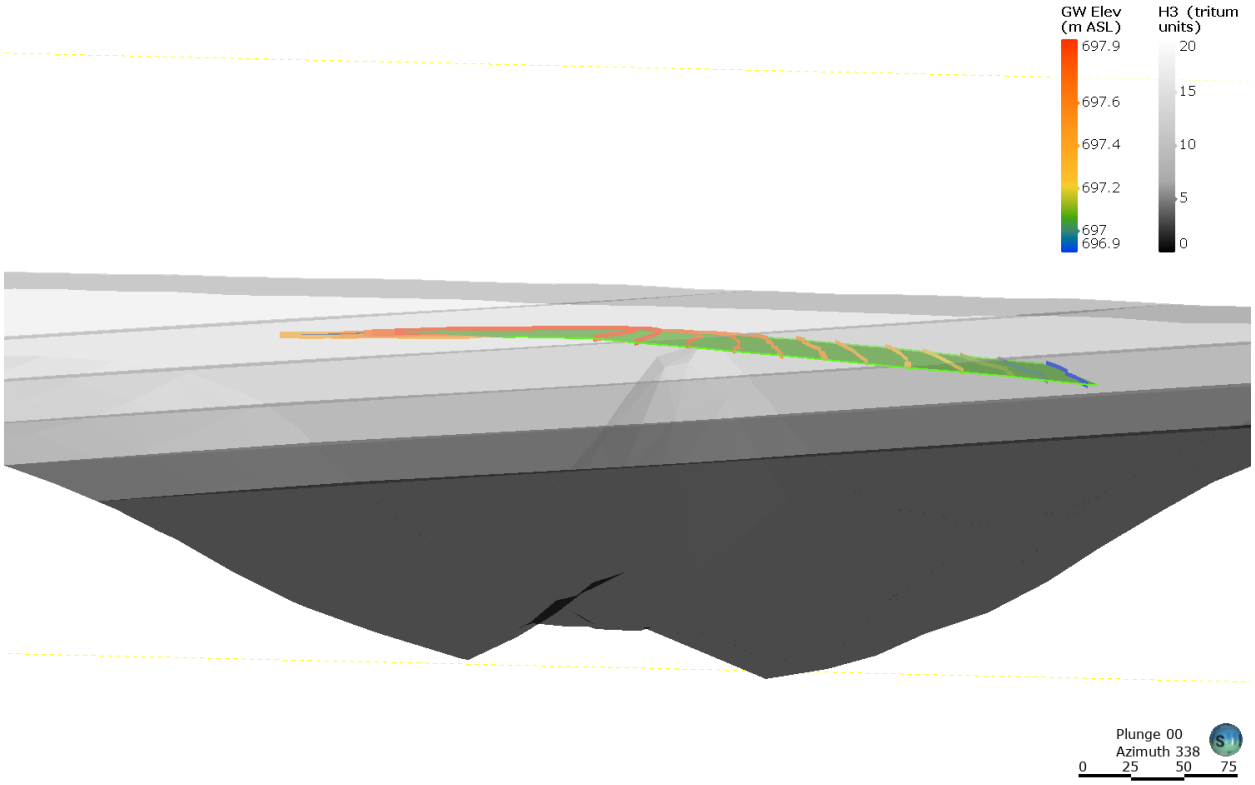

Figure 5.4 Relationship between tritium concentrations to groundwater flow in the catotelm

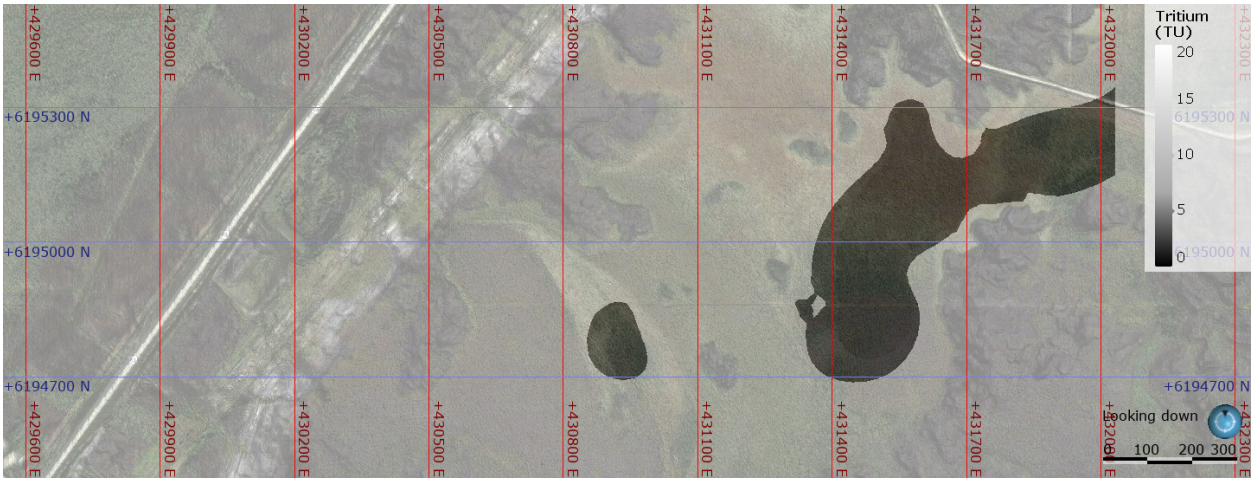

Figure 5.5 Plan view of tritium distribution where the darkest shades demonstrate low to no levels of tritium, indicating groundwater that is older than 70 years.

6. CONCLUSIONS AND FUTURE WORK

There is an identified need to develop scientific communication tools to further understand peatland evolution, geomorphology, hydrology, ecology, and geochemistry. The intention of this research was to develop a novel approach to digitally geovisualize a wetland complex near Mariana Lakes in the Athabasca Oilsands Region of Alberta using LiDAR and GPR as a communication and analytical research tool.

The main analytical objectives of this thesis were to:

v. integrate existing in-situ hydrological and geochemical data with geo-spatial data in a 3D hydrogeological framework,
vi. improve upon early conceptualizations of peatland architecture (Figure 1.1).
vii. investigate peatland groundwater hydrology with respect to tritium concentrations, and
viii. determine volumetric amounts of stored carbon and nitrogen.

A 3D hydrogeological data framework was developed in Seequent *LeapFrogGeo*, a geological modelling software, using available geo-spatial data, existing in-situ hydrogeological data from drive-point piezometers, a 23 square kilometre LiDAR dataset, and 17 GPR radargrams collected using a MALÅ Rough Terrain Antenna. *LeapFrogGeo* is a popular scientific software used in the mining industry and select water resource applications, however its use in peatland analysis and wetland conservation is uncommon. 3D geovisualization in *LeapFrogGeo* proved to be a valuable tool for peatland visualization and analysis of geospatial, geologic, and geophysical data. Non-intrusive remote sensing methods, including LiDAR and GPR were instrumental in determining peatland depth and architecture without installing an overabundance of intrusive piezometers or peat cores across the site. The peatland was assessed as a significant carbon and nutrient sink with average ammonium concentration of 3 grams per cubic meter (g/m^3) of peat, Total Kjeldahl Nitrogen 5 g/m^3, dissolved organic carbon 60 g/m^3, and dissolved inorganic carbon 200 g/m^3.

Prior to the proliferation of atmospheric atomic weapons testing in the 1950s and 1960s atmospheric concentrations of tritium were low. Following the cease of atmospheric atomic weapons testing from the international *Limited Test-Ban Treaty* in 1963 tritium has been entering the water cycle and groundwater systems in significant amounts through precipitation. Sampling revealed the absence of tritium concentrations in anaerobic peat layers greater than 3 metres, therefore detecting palaeowater older than 50 years (Figure 6.1).

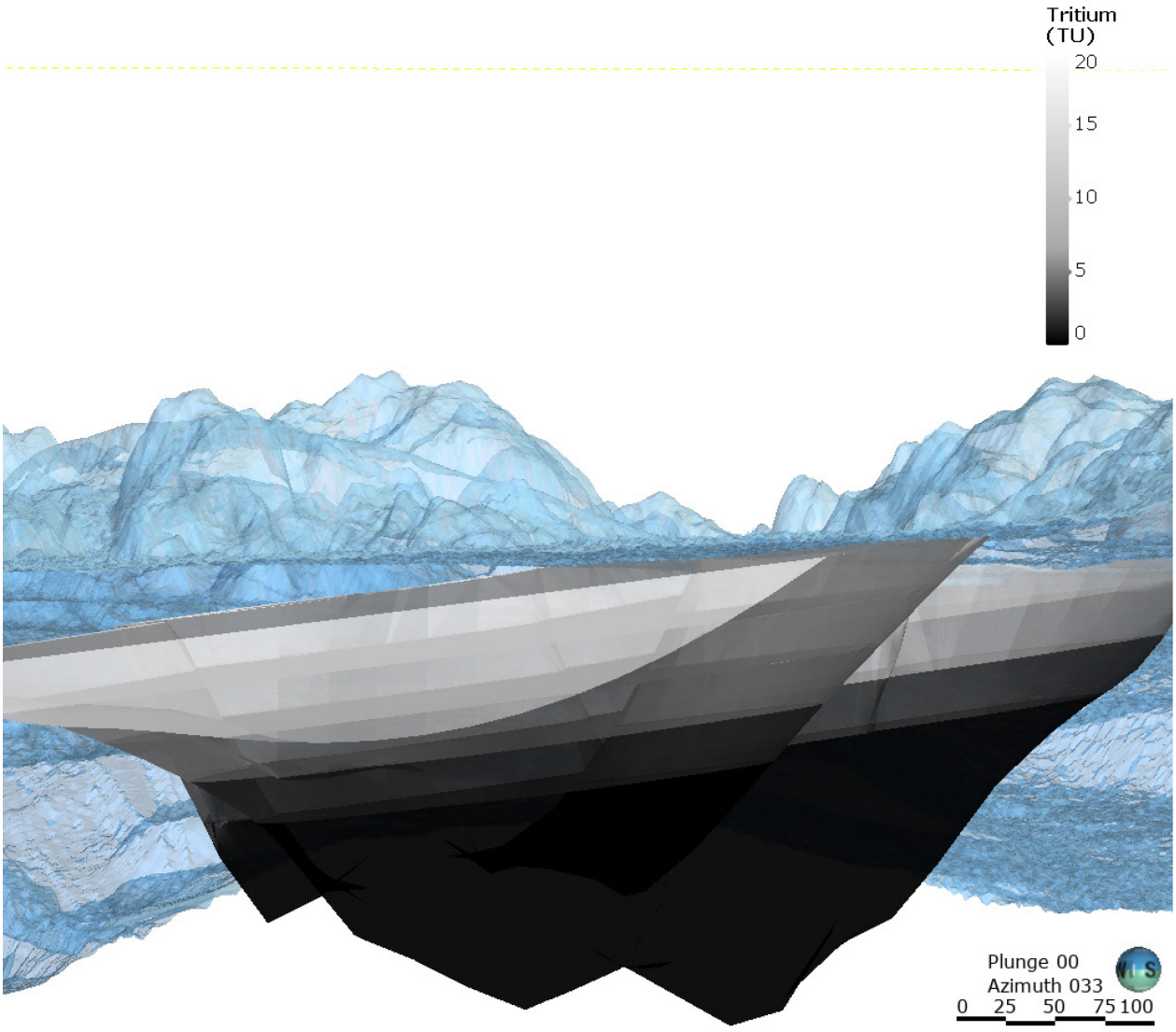

Figure 6.1 Tritium distribution where the darkest shades demonstrate low to no levels of tritium, indicating groundwater that is older than 50 years.

It is likely that groundwater in deeper reaches of the peatland is much older than that estimated by analysis of tritium values. Peatland development reconstructions from other stable isotopes and peat core analysis demonstrated that peat age is approximately 1000 years per 1 m of peat (Nicholson & Vitt, 1990; Yu et al., 2014). It is probable that water in the deepest parts of the peatland was deposited during early paludification (organic accumulation) and due to sluggish hydraulic conductivity and hydraulic traps from established gravity driven flow (Tóth, 2013; 2009; 1963) can be considered several thousands of years old. Large quantities of nutrients and carbon stored at these depths are likely of similar age. Future studies analysing other water soluble stable isotopes would refine the age of groundwater and determine the age of dissolved carbon and nutrient. Future research using the *LeapFrogGeo* geological model with hydrogeological modelling suites like MODFLOW or FEFLOW could assist in understanding of water balance and detailed fate and transport of groundwater in the peatland. LiDAR acquisition was in 2011; therefore, a new LiDAR dataset could provide a ten-year analysis of microtopography. Since the collection of analog-style GPR data in 2016 there has been significant advances in the technology such as high-dynamic-range GPR antennas with unmanned aerial vehicle deployment (Appendix A). The success of the GPR *Frequency-and-Time-Domain Signal Processing Modified Method* (Appendix C) developed for this project encourages future study. The release of LeapFrog 2021.1 allows for direct import of GPR data which can be compared to this thesis methodology.

Development of the Athabasca Oil Sands Region is raising concerns over the increasing impact on boreal peatland ecosystems from land-use practices, wildfire, water extraction, and anthropogenic atmospheric nitrogen deposition. It was determined by this project and others as part of the Cumulative Environmental Management Association nitrogen-amendment study that peatland ecosystems are highly sensitive to land-use practices, atmospheric contamination, and climatic change (Aherne & Shaw, 2010; Cherry, 2015; Küsel, 2014; Vallarino, 2014; Wieder et al., 2019). This project specifically demonstrates that preservation of healthy fens should be paramount in wetland conservation planning and be included as a priority mitigating measure in industrial environmental impact assessments in the boreal forest.

7. CLOSURE

This thesis and associated *LeapFrogGeo* model are available for use for non-commercial purposes under a creative commons attribution license (CC BY-NC 4.0).

Creative Commons public licenses provide a standard set of terms and conditions that creators and other rights holders may use to share original works of authorship and other material subject to copyright and certain other rights specified in the public license below. The following considerations are for informational purposes only, are not exhaustive, and do not form part of our licenses. The license for this thesis and associated *LeapFrogGeo* model allows a researcher to copy and redistribute the material in any medium or format and adapt to remix, transform, and build up the material. However, this license requires attribution, therefore, the user of this research must give appropriate credit, provide a link to the license, and indicate if changes were made. The user may do so in any reasonable manner, but not in any way that suggests the licensor endorses the use.

This thesis was based on the conditions which existed within the study area at the time of investigations and relied on information provided by other persons from academia, industry, and government. While the author of this thesis endeavoured to verify the accuracy of such information, the author accepts no responsibility for the accuracy or the reliability of such information when used for other purposes.

This research was conducted in a manner consistent with the level of skill ordinarily exercised by members of the Engineering and Geoscience profession. If you have any questions please contact the author at shulba@uvic.ca.

8. BIBLIOGRAPHY

Aherne, J., & Shaw, D. P. (2010). Impacts of sulphur and nitrogen deposition in western Canada. *Journal of Limnology*, *69*(SUPPL. 1), 1–3. https://doi.org/10.3274/JL10-69-S1-01

Alberta Environment and Parks (AEP). (2017). *Reclamation Criteria for Wellsites and Associated Facilities for Peatlands*. http://aep.alberta.ca/land/programs-and-services/reclamation-and-remediation/upstream-oil-and-gas-reclamation-and-remediation-program/documents/ReclamationCriteriaPeatlands-Mar2017.pdf

Alberta Environment and Sustainable Resource Development. (2015). *Alberta Wetland Classification System*.

Andraishek, L. D. (2003). Quaternary Geological Setting of the Athabasca Oil Sands (In Situ) Area, Northeast Alberta. In *Alberta Geological Survey*.

Andrienko, G., Andrienko, N., Dykes, J., Fabrikant, S. I., & Wachowicz, M. (2008). Geovisualization of dynamics, movement and change: Key issues and developing approaches in visualization research. *Information Visualization*, *7*(3–4), 173–180. https://doi.org/10.1057/ivs.2008.23

Attig, J. W., Mickelson, D. M., & Clayton, L. (1989). Late Wisconsin landform distribution and glacier-bed conditions in Wisconsin. *Sedimentary Geology*, *62*(2–4), 399–405. https://doi.org/10.1016/0037-0738(89)90128-0

Barthel, R., & Banzhaf, S. (2016). Groundwater and Surface Water Interaction at the Regional-scale – A Review with Focus on Regional Integrated Models. *Water Resources Management*, *30*(1), 1–32. https://doi.org/10.1007/s11269-015-1163-z

Bayer, P., Huggenberger, P., Renard, P., & Comunian, A. (2011). Three-dimensional high resolution fluvio-glacial aquifer analog: Part 1: Field study. *Journal of Hydrology*, *405*(1–2), 1–9. https://doi.org/10.1016/j.jhydrol.2011.03.038

Birks, J., Fennell, J., Yi, Y., Gibson, J., & Moncur, M. (2017). *Regional Geochemistry Study for the Southern Athabasca Oil Sands (SAOS) Area*. *May*, 63.

Bizhanimanzar, M., Leconte, R., & Nuth, M. (2018). Modelling of shallow water table dynamics using conceptual and physically based integrated surface water-groundwater hydrologic models. *Hydrology and Earth System Sciences Discussions*, 1–25.

https://doi.org/10.5194/hess-2018-359

Bridgham, S. D., Pastor, J., Updegraff, K., Malterer, T. J., Johnson, K., Harth, C., & Chen, J. (1999). Ecosystem control over temperature and energy flux in northern peatlands. *Ecological Applications*, *9*(4), 1345–1358. https://doi.org/10.1890/1051-0761(1999)009[1345:ECOTAE]2.0.CO;2

Bubier, J., Crill, P., Mosedale, A., Frolking, S., & Linder, E. (2003). Peatland responses to varying interannual moisture conditions as measured by automatic CO2 chambers. *Global Biogeochemical Cycles*, *17*(2). https://doi.org/10.1029/2002gb001946

Chasmer, L., Mahoney, C., Millard, K., Nelson, K., Peters, D., Merchant, M., Hopkinson, C., Brisco, B., Niemann, O., Montgomery, J., Devito, K., & Cobbaert, D. (2020). Remote sensing of boreal wetlands 2: Methods for evaluating boreal wetland ecosystem state and drivers of change. *Remote Sensing*, *12*(8). https://doi.org/10.3390/RS12081321

Chen, Y., Khan, S., Rana, T., Abbas, A., & Buettikofer, H. (2012). Three Dimensional Conceptualisation of Hydrogeological Environment to Underpin Groundwater Management in Irrigation Area. *Water Resources Management*, *26*(11), 3077–3093. https://doi.org/10.1007/s11269-012-0095-0

Chernokalov, A. G., Chubinsky, N., & Krampuls, A. (2000). Method of amplitude and phase correction of GPR system transient response. *Eighth International Conference on Ground Penetrating Radar*, *4084*(April 2000), 324–328. https://doi.org/10.1117/12.383585

Cherry, M. (2015). *Nitrogen Transport and Connectivity in two Wetland-Rich Boreal sites in the Athabasca Oil Sands Region, Canada*. https://doi.org/10.1017/CBO9781107415324.004

Cheskey, E., Wells, J., Casey-lefkowitz, S., Ballin, P., Butterworth, E., Chagnon, M., Childs, D., Darveau, M., Davidson, I., Dudouet, A., Donaldson, G., Drolet, C., Finney, G., Goffredi, L., Kerry, M., Labrecque, M., Mccrummen, L., Mclaughlin, J., Neville, J., … Sutton, C. (2011). Birds at Risk: The Importance of Canada's Boreal Wetlands and Waterways. In *Natural Resources Defense Council* (Issue October).

Clymo, R. S. (1992). *Models of Peat Growth* (pp. 127–136).

Collettini, C. (2011). The mechanical paradox of low-angle normal faults: Current understanding

and open questions. *Tectonophysics*, *510*(3–4), 253–268. https://doi.org/10.1016/j.tecto.2011.07.015

Comas, X., Slater, L., & Reeve, A. (2005). Stratigraphic controls on pool formation in a domed bog inferred from ground penetrating radar (GPR). *Journal of Hydrology*, *315*(1–4), 40–51. https://doi.org/10.1016/j.jhydrol.2005.04.020

Comas, X., Terry, N., Hribljan, J. A., Lilleskov, E. A., Suarez, E., Chimner, R. A., & Kolka, R. K. (2017). Estimating belowground carbon stocks in peatlands of the Ecuadorian páramo using ground-penetrating radar (GPR). *Journal of Geophysical Research: Biogeosciences*, *122*(2), 370–386. https://doi.org/10.1002/2016JG003550

Constible, J. M., Gregory, P. T., & Anholt, B. R. (2001). Patterns of distribution, relative abundance, and microhabitat use of anurans in a boreal landscape influenced by fire and timber harvest. *Ecoscience*, *8*(4), 462–470. https://doi.org/10.1080/11956860.2001.11682676

Corradini, E., Wilken, D., Zanon, M., Groß, D., Lübke, H., Panning, D., Dörfler, W., Rusch, K., Mecking, R., Erkul, E., Pickartz, N., Feeser, I., & Rabbel, W. (2020). Reconstructing the palaeoenvironment at the early Mesolithic site of Lake Duvensee: Ground-penetrating radar and geoarchaeology for 3D facies mapping. *Holocene*, *30*(6), 820–833. https://doi.org/10.1177/0959683620902234

Dallaire, P., & Garneau, M. (2008). The use of a ground-penetrating radar (GPR) to characterize peat stratigraphy and estimate the carbon pool in a boreal peatland, Eastmain region, James Bay, Québec, Canada. *12th International Conference on Ground Penetrating Rador*, *C*. http://declique.uqam.ca/upload/files/conference/Dallaire_etal GPR2008.pdf

Danielle, K. H., Boutt, D. F., Clement, W. P., Hatch, C. E., Davenport, G., & Hackman, A. (2017). Hydrogeological controls on spatial patterns of groundwater discharge in peatlands. *Hydrology and Earth System Sciences*, *21*(12), 6031–6048. https://doi.org/10.5194/hess-21-6031-2017

Danielopol, D. A. N. L., & Griebler, C. (1918). Incorporation of Groundwater Ecology in Environmental Policy. *Policy*, 671–689. https://doi.org/10.1039/9781847558039

Devito, K. J., Hill, A. R., & Roulet, N. (1996). Groundwater-surface water interactions in headwater

forested wetlands of the Canadian Shield. *Journal of Hydrology*, *181*(1–4), 127–147. https://doi.org/10.1016/0022-1694(95)02912-5

Di Girolamo, P., Behrendt, A., & Wulfmeyer, V. (2018). Space-borne profiling of atmospheric thermodynamic variables with raman lidar. *EPJ Web of Conferences*, *176*(7), 8125–8161. https://doi.org/10.1051/epjconf/201817602002

Drexler, J. Z., Knifong, D., Tuil, J., Flint, L. E., & Flint, A. L. (2013). Fens as whole-ecosystem gauges of groundwater recharge under climate change. *Journal of Hydrology*, *481*, 22–34. https://doi.org/10.1016/j.jhydrol.2012.11.056

Dyke, A. S., Prest, V. K., Dyke, A. S., Prest, V. K., Survey, G., Street, B., & Ka, O. (2019). *Géographie physique et Quaternaire Évolution de la calotte glaciale laurentidienne au Wisconsinien LATE WISCONSINAN AND HOLOCENE HISTORY OF THE LAURENTIDE ICE SHEET **.

Fallis, A. . (2013). Conceptualizing Water Movement in the Boreal Plains. *Journal of Chemical Information and Modeling*, *53*(9), 1689–1699. https://doi.org/10.1017/CBO9781107415324.004

Fenton, M. M., Pawlowicz, J. G., Paulen, R. C., Prior, G. J., & Olson, R. A. (2003). Quaternary geology of northern Alberta: Implications for kimberlite exploration. *Proceedings of the 8th International Kimberlite Conference Long Abstract*, 1–5.

Flesch, L., Bendick, R., & Bischoff, S. (2018). Limitations on Inferring 3D Architecture and Dynamics From Surface Velocities in the India-Eurasia Collision Zone. *Geophysical Research Letters*, *45*(3), 1379–1386. https://doi.org/10.1002/2017GL076503

Francke, J. (2010). *GPR Rough Terrain Antenna Applications in Mineral and Groundwater Prospecting*. 1–3. http://www.malagpr.com.au/uploads/3/7/9/4/37942849/francke_-_rta_-_nltechnote_rta-white-paper_v5.pdf

Frei, S., & Gilfedder, B. S. (2015). FINIFLUX: An implicit finite element model for quantification of groundwater fluxes and hyporheic exchange in streams and rivers using radon. *Water Resources Research*, *51*, 6776–6786. https://doi.org/10.1002/2015WR017212.Received

Gatis, N., Luscombe, D. J., Carless, D., Parry, L. E., Fyfe, R. M., Harrod, T. R., Brazier, R. E., & Anderson, K. (2019). Mapping upland peat depth using airborne radiometric and lidar survey

data. *Geoderma*, *335*(July 2018), 78–87. https://doi.org/10.1016/j.geoderma.2018.07.041

Gatziolis, D., & Andersen, H. E. (2008). A guide to LIDAR data acquisition and processing for the forests of the pacific northwest. *USDA Forest Service - General Technical Report PNW-GTR*, *768*, 1–32. https://doi.org/10.2737/PNW-GTR-768

Gibson, J. J., Birks, S. J., & Moncur, M. (2019). Mapping water yield distribution across the South Athabasca Oil Sands (SAOS) area: Baseline surveys applying isotope mass balance of lakes. *Journal of Hydrology: Regional Studies*, *21*(November 2018), 1–13. https://doi.org/10.1016/j.ejrh.2018.11.001

Gibson, J. J., Birks, S. J., Yi, Y., & Vitt, D. H. (2015). Runoff to boreal lakes linked to land cover, watershed morphology and permafrost thaw: A 9-year isotope mass balance assessment. *Hydrological Processes*, *29*(18), 3848–3861. https://doi.org/10.1002/hyp.10502

Gleeson, T., Befus, K. M., Jasechko, S., Luijendijk, E., & Cardenas, M. B. (2016). The global volume and distribution of modern groundwater. *Nature Geoscience*, *9*(2), 161–164. https://doi.org/10.1038/ngeo2590

Gorham, E., Lehman, C., Dyke, A., Clymo, D., & Janssens, J. (2012). Long-term carbon sequestration in North American peatlands. *Quaternary Science Reviews*, *58*, 77–82. https://doi.org/10.1016/j.quascirev.2012.09.018

Gorham, E., Lehman, C., Dyke, A., Janssens, J., & Dyke, L. (2007). Temporal and spatial aspects of peatland initiation following deglaciation in North America. *Quaternary Science Reviews*, *26*(3–4), 300–311. https://doi.org/10.1016/j.quascirev.2006.08.008

Government of BC Ministry of Environment. (2009). *Manual of British Columbia hydrometric standards*. 204. http://www.ilmb.gov.bc.ca/risc

Grayson, R., Holden, J., Jones, R. R., Carle, J. A., & Lloyd, A. R. (2012). Improving particulate carbon loss estimates in eroding peatlands through the use of terrestrial laser scanning. *Geomorphology*, *179*, 240–248. https://doi.org/10.1016/j.geomorph.2012.08.015

Halsey, L. A., Vitt, D. H., & Gignac, L. D. (2000). Sphagnum -dominated Peatlands in North America Since the Last Glacial Maximum: Their Occurrence and Extent . *The Bryologist*, *103*(2), 334–352. https://doi.org/10.1639/0007-2745(2000)103[0334:sdpina]2.0.co;2

Hama, A. M., A. Sansone, Seitz, M., & Stötter, J. (2000). Environmental Role of Wetlands in Headwaters. In *Environmental Role of Wetlands in Headwaters*.

Happell, J. D., Östlund, G., & Mason, A. S. (2004). A history of atmospheric tritium gas (HT) 1950–2002. *Tellus B: Chemical and Physical Meteorology*, *56*(3), 183–193. https://doi.org/10.3402/tellusb.v56i3.16422

Horota, R. K., Aires, A. S., Marques, A., Rossa, P., De Souza, E. M., De Souza, E. M., Gonzaga, L., & Veronez, M. R. (2020). Printgrammetry-3-D Model Acquisition Methodology from Google Earth Imagery Data. *IEEE Journal of Selected Topics in Applied Earth Observations and Remote Sensing*, *13*, 2819–2830. https://doi.org/10.1109/JSTARS.2020.2997239

Hurtley, S. M. (2018). Optical Astronomy: The resolution revolution. *Science*, *360*(6386), 282. https://doi.org/10.1126/science.360.6386.280-k

Hutton, M. J., Macdonald, G. M., & Mott, R. J. (1994). Postglacial vegetation history of the Mariana Lake region, Alberta. *Canadian Journal of Earth Sciences*, *31*(2), 418–425. https://doi.org/10.1139/e94-038

Hyvönen, N. P., Huttunen, J. T., Shurpali, N. J., Lind, S. E., Marushchak, M. E., Heitto, L., & Martikainen, P. J. (2013). The role of drainage ditches in greenhouse gas emissions and surface leaching losses from a cutaway peatland cultivated with a perennial bioenergy crop. *Boreal Environment Research*, *18*(2), 109–126.

Johnson, M. D., Fredin, O., Ojala, A. E. K., & Peterson, G. (2015). Unraveling Scandinavian geomorphology: the LiDAR revolution. *Gff*, *137*(4), 245–251. https://doi.org/10.1080/11035897.2015.1111410

Johnston, C. A. (2017). Beavers: Boreal ecosystem engineers. In *Beavers: Boreal Ecosystem Engineers*. https://doi.org/10.1007/978-3-319-61533-2

Jol, H. M., & Smith, D. G. (1995). Ground penetrating radar surveys of peatlands for oilfield pipelines in Canada. *Journal of Applied Geophysics*, *34*(2), 109–123. https://doi.org/10.1016/0926-9851(95)00018-6

Joosten, H., & Clarke, D. (2002). Wise Use of Mires and Peatlands. In *International Mire Conservation Group and International Peat Society, Helsinki* (Issue June).

https://doi.org/10.1016/s0925-8574(98)00046-9

Joppe, M., D'Imprima, E., Salustros, N., Paithankar, K. S., Vonck, J., Grininger, M., & Kuhlbrandt, W. (2020). The resolution revolution in cryoEM requires high-quality sample preparation: A rapid pipeline to a high-resolution map of yeast fatty acid synthase. *IUCrJ*, *7*, 220–227. https://doi.org/10.1107/S2052252519017366

Jung, J. K. (2015). Code clouds: Qualitative geovisualization of geotweets. *Canadian Geographer*, *59*(1), 52–68. https://doi.org/10.1111/cag.12133

Kaifler, B., Rempel, D., Roßi, P., Büdenbender, C., Kaifler, N., & Baturkin, V. (2020). A technical description of the Balloon Lidar Experiment (BOLIDE). *Atmospheric Measurement Techniques*, *13*(10), 5681–5695. https://doi.org/10.5194/amt-13-5681-2020

Kawakita, M., Sasaki, H., Arai, J., Okano, F., Suehiro, K., Haino, Y., Yoshimura, M., & Sato, M. (2008). Geometric analysis of spatial distortion in projection-type integral imaging. *Optics Letters*, *33*(7), 684. https://doi.org/10.1364/ol.33.000684

Kenady, S. L., Lowe, K. M., Ridd, P. V., & Ulm, S. (2018). Creating volume estimates for buried shell deposits: A comparative experimental case study using ground-penetrating radar (GPR) and electrical resistivity under varying soil conditions. *Archaeological Prospection*, *25*(2), 121–136. https://doi.org/10.1002/arp.1594

Kennedy, C. D., Wilderotter, S., Payne, M., Buda, A. R., Kleinman, P. J. A., & Bryant, R. B. (2018). A geospatial model to quantify mean thickness of peat in cranberry bogs. *Geoderma*, *319*(September 2017), 122–131. https://doi.org/10.1016/j.geoderma.2017.12.032

Koyan, P., & Tronicke, J. (2020). 3D modeling of ground-penetrating radar data across a realistic sedimentary model. *Computers and Geosciences*, *137*(June 2019), 104422. https://doi.org/10.1016/j.cageo.2020.104422

Kraak, M. J. (2003). Geovisualization illustrated. *ISPRS Journal of Photogrammetry and Remote Sensing*, *57*(5–6), 390–399. https://doi.org/10.1016/S0924-2716(02)00167-3

Krasowski, C. (2019). On the Modelling of Solar Radiation in Urban Environments – Applications of Geomatics and Climatology Towards Climate Action in Victoria. In *Master of Science*.

Kubíček, P., Šašinka, Č., Stachoň, Z., Herman, L., Juřík, V., Urbánek, T., & Chmelík, J. (2019).

Identification of altitude profiles in 3D geovisualizations: the role of interaction and spatial abilities. *International Journal of Digital Earth*, *12*(2), 156–172. https://doi.org/10.1080/17538947.2017.1382581

Kurz, W. A., Shaw, C. H., Boisvenue, C., Stinson, G., Metsaranta, J., Leckie, D., Dyk, A., Smyth, C., & Neilson, E. T. (2013). Carbon in Canada's boreal forest — A synthesis. *Environmental Reviews*, *21*(4), 260–292. https://link.gale.com/apps/doc/A357035386/CPI?u=uvictoria&sid=CPI&xid=19e9ea8a

Küsel, C. (2014). *Baseline hydrogeochemistry and connectivity among landscape units of two wetland-rich Boreal sites in the Athabasca Oils Sands Region, Alberta*. University of Victoria.

Kwan, M. P. (2000). Interactive geovisualization of activity-travel patterns using three-dimensional geographical information systems: A methodological exploration with a large data set. *Transportation Research Part C: Emerging Technologies*, *8*(1–6), 185–203. https://doi.org/10.1016/S0968-090X(00)00017-6

Li, Y., & Vitt, D. H. (1997). Patterns of retention and utilization of aerially deposited nitrogen in boreal peatlands. *Ecoscience*, *4*(1), 106–116. https://doi.org/10.1080/11956860.1997.11682384

Lucas, T. W., David Kelton, W., Sánchez, P. J., Sanchez, S. M., & Anderson, B. L. (2015). Changing the paradigm: Simulation, now a method of first resort. *Naval Research Logistics*, *62*(4), 293–303. https://doi.org/10.1002/nav.21628

Luscombe, D. J., Anderson, K., Gatis, N., Grand-Clement, E., & Brazier, R. E. (2015). Using airborne thermal imaging data to measure near-surface hydrology in upland ecosystems. *Hydrological Processes*, *29*(6), 1656–1668. https://doi.org/10.1002/hyp.10285

MacCormack, K. E., Berg, R. C., Kessler, H., Russell, H. A. J., & Thorleifson, L. H. (2019). 2019 Synopsis of Current Three-Dimensional Geological Mapping and Modelling in Geological Survey Organizations. In *Alberta Energy Regulator / Alberta Geological Survey, AER/AGS Special Report 112*. https://ags.aer.ca/publications/SPE_112.html#summary

MacEachren, A. M., & Kraak, M.-J. (2001). Research Challenges in Geovisualization. *Cartography and Geographic Information Science*, *28*(1), 3–12.

https://doi.org/10.1559/152304001782173970

Maxa, M., & Bolstad, P. (2009). Mapping northern wetlands with high resolution satellite images and LiDAR. *Wetlands*, *29*(1), 248–260. https://doi.org/10.1672/08-91.1

Michel, R. L., Aggarwal, P., Araguas-Araguas, L., Kurttas, T., Newman, B. D., & Vitvar, T. (2015). A simplified approach to analysing historical and recent tritium data in surface waters. *Hydrological Processes*, *29*(4), 572–578. https://doi.org/10.1002/hyp.10174

Minasny, B., Berglund, Ö., Connolly, J., Hedley, C., de Vries, F., Gimona, A., Kempen, B., Kidd, D., Lilja, H., Malone, B., McBratney, A., Roudier, P., O'Rourke, S., Rudiyanto, Padarian, J., Poggio, L., ten Caten, A., Thompson, D., Tuve, C., & Widyatmanti, W. (2019). Digital mapping of peatlands – A critical review. *Earth-Science Reviews*, *196*(June 2018), 102870. https://doi.org/10.1016/j.earscirev.2019.05.014

Mitsch, W. J., & Gosselink, J. G. (2015). *Wetlands* (5th ed.). John Wiley & Sons, Incorporated.

Mitsova, D., Wissinger, F., Esnard, A. M., Shankar, R., & Gies, P. (2013). A collaborative geospatial shoreline inventory tool to guide coastal development and habitat conservation. *ISPRS International Journal of Geo-Information*, *2*(2), 385–404. https://doi.org/10.3390/ijgi2020385

Mossa, J., Chen, Y. H., & Wu, C. Y. (2019). Geovisualization geoscience of large river floodplains. *Journal of Maps*, *15*(3), 75–91. https://doi.org/10.1080/17445647.2019.1584129

Murphy, P. N. C., Ogilvie, J., Connor, K., & Arp, P. A. (2007). Mapping wetlands: A comparison of two different approaches for New Brunswick, Canada. *Wetlands*, *27*(4), 846–854. https://doi.org/10.1672/0277-5212(2007)27[846:MWACOT]2.0.CO;2

National Academies of Sciences Engineering and Medicine. (2017). Communicating science effectively: A research agenda. In *Communicating Science Effectively: A Research Agenda*. https://doi.org/10.17226/23674

Natural Resources Canada. (2017). Geospatial Data Extraction. *Government of Canada*. http://geogratis.gc.ca/site/eng/extraction

Nicholson, B. J. (1989). Peat chemistry of a continental mire complex in western Canada. *Canadian Journal of Botany*, *67*(3), 763–775. https://doi.org/10.1139/b89-103

Nicholson, Barbara J. (1987). *Peatland Paleoecology and Peat Chemistry at Mariana Lakes, Alberta*. University of Alberta.

Nicholson, Barbara J., & Vitt, D. H. (1990). The paleoecology of a peatland complex in continental western Canada. *Canadian Journal of Botany*, *68*(1), 121–138. https://doi.org/10.1139/b90-017

Nielsen, A., Bolding, K., Hu, F., & Trolle, D. (2017). An open source QGIS-based workflow for model application and experimentation with aquatic ecosystems. *Environmental Modelling and Software*, *95*, 358–364. https://doi.org/10.1016/j.envsoft.2017.06.032

Paulen, R. C., & McClenaghan, M. B. (2014). Late wisconsin ice-flow history in the buffalo head hills kimberlite field, north-central alberta. *Canadian Journal of Earth Sciences*, *52*(1), 51–67. https://doi.org/10.1139/cjes-2014-0109

Philibert, A., Prairie, Y. T., & Carcaillet, C. (2003). 1200 Years of fire impact on biogeochemistry as inferred from high resolution diatom analysis in a kettle lake from the Picea mariana-moss domain (Quebec, Canada). *Journal of Paleolimnology*, *30*(2), 167–181. https://doi.org/10.1023/A:1025526200880

Poggio, L., Gimona, A., Aalders, I., Morrice, J., & Hough, R. (2020). Legacy data for 3D modelling of peat properties with uncertainty estimation in Dava bog - Scotland. *Geoderma Regional*, *22*, e00288. https://doi.org/10.1016/j.geodrs.2020.e00288

Price, J. S., Heathwaite, A. L., & Baird, A. (2003). Hydrological processes in abandoned and restored peatlands. *Wetlands and Ecological Management*, *11*, 65–83.

Proulx-McInnis, S., St-Hilaire, A., Rousseau, A. N., & Jutras, S. (2013). A review of ground-penetrating radar studies related to peatland stratigraphy with a case study on the determination of peat thickness in a northern boreal fen in Quebec, Canada. *Progress in Physical Geography*, *37*(6), 767–786. https://doi.org/10.1177/0309133313501106

Robins, N. S., Rutter, H. K., Dumpleton, S., & Peach, D. W. (2005). The role of 3D visualisation as an analytical tool preparatory to numerical modelling. *Journal of Hydrology*, *301*(1–4), 287–295. https://doi.org/10.1016/j.jhydrol.2004.05.004

Russell, M., Eitel, J. U. H., Maguire, A. J., & Link, T. E. (2020). Toward a novel laser-based approach

for estimating snow interception. *Remote Sensing*, *12*(7), 1–11. https://doi.org/10.3390/rs12071146

Saari, P., Saarnio, S., Heinonen, J., & Alm, J. (2013). Emissions and dynamics of N2O in a buffer wetland receiving water flows from a forested peatland. *Boreal Environment Research*, *18*(2), 164–180.

Schultz, J. J., & Martin, M. M. (2011). Controlled GPR grave research: Comparison of reflection profiles between 500 and 250MHz antennae. *Forensic Science International*, *209*(1–3), 64–69. https://doi.org/10.1016/j.forsciint.2010.12.012

Seaber, P. R., Kapinos, F. P., & Knapp, G. L. (1987). *Hydrologic Unit Maps*. United States Geological Survey.

Seequent Limited. (2020). Leapfrog3D Geo Ver 5.1 Manual. In *Seequent Limited* (Vol. 3304, Issue January).

Signals and Communication Technology. (2019). *3D Visual Content Creation, Coding and Delivery*. http://link.springer.com/10.1007/978-3-319-77842-6

Silvius, M. (2007). *Global assessment on peatlands biodiversity and climate change* (Issue December).

Sonnentag, O., Van Der KAMP, G., Barr, a. G., & Chen, J. M. (2009). On the relationship between water table depth and water vapor and carbon dioxide fluxes in a minerotrophic fen. *Global Change Biology*, *16*(6), 1762–1776. https://doi.org/10.1111/j.1365-2486.2009.02032.x

Stephenson, P. J., Ntiamoa-Baidu, Y., & Simaika, J. P. (2020). The Use of Traditional and Modern Tools for Monitoring Wetlands Biodiversity in Africa: Challenges and Opportunities. *Frontiers in Environmental Science*, *8*(June), 1–12. https://doi.org/10.3389/fenvs.2020.00061

Stovall, A. E. L., Diamond, J. S., Slesak, R. A., McLaughlin, D. L., & Shugart, H. (2019). Quantifying wetland microtopography with terrestrial laser scanning. *Remote Sensing of Environment*, *232*(June), 111271. https://doi.org/10.1016/j.rse.2019.111271

Stuart, J. E. M., Wieder, R. K., & Vile, M. A. (2018). Net nitrogen mineralization in Alberta bog peat is insensitive to experimentally increased nitrogen deposition and time since wildfire. *Biogeochemistry*, *138*(2), 155–170. https://doi.org/10.1007/s10533-018-0437-y

Tattrie, K. (2011). *Groundwater surface water interactions in a wetland rich, low relief Boreal environment*. University of Victoria.

Theimer, B. D., Nobes, D. C., & Warner, B. G. (1994). A study of the geoelectrical properties of peatlands and their influence on ground-penetrating radar surveying. *Geophysical Prospecting*, *42*(3), 179–209. https://doi.org/10.1111/j.1365-2478.1994.tb00205.x

Tóth, J. (1999). Groundwater as a geologic agent: An overview of the causes, processes, and manifestations. In *Hydrogeology Journal* (Vol. 7, Issue 1, pp. 1–14). https://doi.org/10.1007/s100400050176

Tóth, J. (2009). Gravitational systems of groundwater flow. In *Gravitational Systems of Groundwater Flow* (Vol. 9780521886). https://doi.org/10.1017/CBO9780511576546

Toth, Jozef. (2013). Gravitational Systems of Groundwater Flow. In *Journal of Chemical Information and Modeling* (Vol. 53, Issue 9). https://doi.org/10.1017/CBO9781107415324.004

Toth, József. (1963). A Theoretical Analysis of Groundwater Flow in Small Drainage Basins 1 of phe - low order stream and having similar t he outlet of lowest impounded body of a relatively. *Journal of Geophysical Research*, *68*(16), 4795–4812. https://doi.org/10.1029/JZ068i016p04795

Tuittila, E. S., Vasander, H., & Laine, J. (2004). Sensitivity of C sequestration in reintroduced Sphagnum to water-level variation in a cutaway peatland. *Restoration Ecology*, *12*(4), 483–493. https://doi.org/10.1111/j.1061-2971.2004.00280.x

Turchenek, L. W. (1990). Present and potential effects of anthropogenic activities on waters associated with peatland in Alberta. *Environmental Research and Engineering Department, Alberta Research Council.*, *April*.

US Environmental Protection Agency. (2014). *3PE : A Tool for Estimating Groundwater Flow Vectors*. *September*, 60. https://cfpub.epa.gov/si/si_public_record_report.cfm?dirEntryId=287064

Vallarino, A. (2014). *Implications of shallow groundwater and surface water connections for nitrogen movement in typical Boreal Plain landscapes*.

https://doi.org/10.1017/CBO9781107415324.004

Valois, R., Schaffer, N., Figueroa, R., Maldonado, A., Yáñez, E., Hevia, A., Carrizo, G. Y., & MacDonell, S. (2020). Characterizing the water storage capacity and hydrological role of mountain peatlands in the arid andes of North-Central Chile. *Water (Switzerland)*, *12*(4). https://doi.org/10.3390/W12041071

Van Bellen, S., Dallaire, P. L., Garneau, M., & Bergeron, Y. (2011). Quantifying spatial and temporal Holocene carbon accumulation in ombrotrophic peatlands of the Eastmain region, Quebec, Canada. *Global Biogeochemical Cycles*, *25*(2), 1–15. https://doi.org/10.1029/2010GB003877

Velasco, V., Gogu, R., Vázquez-Suñè, E., Garriga, A., Ramos, E., Riera, J., & Alcaraz, M. (2013). The use of GIS-based 3D geological tools to improve hydrogeological models of sedimentary media in an urban environment. *Environmental Earth Sciences*, *68*(8), 2145–2162. https://doi.org/10.1007/s12665-012-1898-2

Vitt, D. H., & Bhatti, J. S. (2012). *Restoration and Reclaimation Boreal Ecosystems*.

Volik, O., Elmes, M., Petrone, R., Kessel, E., Green, A., Cobbaert, D., & Price, J. (2020). Wetlands in the Athabasca Oil Sands Region: the nexus between wetland hydrological function and resource extraction. *Environmental Reviews*, *28*(3), 246–261. https://doi.org/10.1139/er-2019-0040

Walker, I. J., Eamer, J. B. R., & Darke, I. B. (2013). Assessing significant geomorphic changes and effectiveness of dynamic restoration in a coastal dune ecosystem. *Geomorphology*, *199*, 192–204. https://doi.org/10.1016/j.geomorph.2013.04.023

Westbrook, C. J., Devito, K. J., & Allan, C. J. (2006). Soil N cycling in harvested and pristine Boreal forests and peatlands. *Forest Ecology and Management*, *234*(1–3), 227–237. https://doi.org/10.1016/j.foreco.2006.07.004

Wieder, R. K., & Vitt, D. H. (2006). Boreal Peatland Ecosystems. In *Journal of Chemical Information and Modeling* (Vol. 53, Issue 9). https://doi.org/10.1017/CBO9781107415324.004

Wieder, R. K., Vitt, D. H., Vile, M. A., Graham, J. A., Hartsock, J. A., Fillingim, H., House, M., Quinn, J. C., Scott, K. D., Petix, M., & McMillen, K. J. (2019). Experimental nitrogen addition alters

structure and function of a boreal bog: critical load and thresholds revealed. *Ecological Monographs*, *89*(3), 1–35. https://doi.org/10.1002/ecm.1371

Wijesekara, G. N., Farjad, B., Gupta, A., Qiao, Y., Delaney, P., & Marceau, D. J. (2014). A comprehensive land-use/hydrological modeling system for scenario simulations in the Elbow River watershed, Alberta, Canada. *Environmental Management*, *53*(2), 357–381. https://doi.org/10.1007/s00267-013-0220-8

Yu, Z., Vitt, D. H., & Wieder, R. K. (2014). Continental fens in western Canada as effective carbon sinks during the Holocene. *Holocene*, *24*(9), 1090–1104. https://doi.org/10.1177/0959683614538075

Zou, M., Ju, T., & Carr, N. (2013). An algorithm for triangulating multiple 3D polygons. *Symposium on Geometry Processing 2013, SGP 2013*, 157–166. https://doi.org/10.1111/cgf.12182

9. APPENDICES

9.1 Appendix A: MALÅ Rough Terrain Antenna System

GPR investigations in geoscience applications generally require low frequency antennas that are long and requires a crew of three or more to deploy which has made deployment of GPR in mining and groundwater applications limited due to the cost and the time needed to complete the investigations (Francke, 2010). There has been a trillion-fold increase in computing power since the wide-spread introduction of analogue-GPR for shallow geophysical assessment in the 1970s (Lucas et al., 2015); therefore advancements in sensor and antenna technology has evolved to promote use of GPR in more challenging terrain and applications.

Traditional GPR deployment used bistatic antennas in a parallel configuration which requires two or more operators (Figure 9.1). This study used the MALÅ Rough Terrain Antenna (RTA) portable GPR antenna system that has a unique all-in-one design in a co-linear configuration (Figure 9.2). There are several frequencies of RTA to choose from and the frequency of antenna chosen for this project was the 50 MHz antenna, commonly used in geological and geotechnical investigations. The lower limit of object target size is approximately 0.5 m and a range of 5-20 m depth. The antenna is approximately 9.25 m long with a separation distance between the transmitter (Tx) and the receiver (Rx) of 4 metres. The weight of the antenna is 7.0 kg and is intrinsically shockproof and is waterproof.

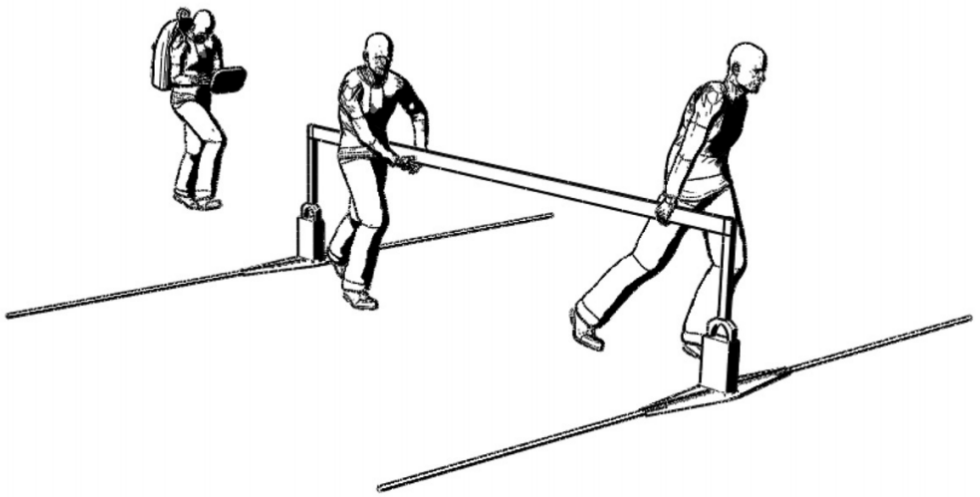

Figure 9.1 Traditional low-frequency GPR in parallel configuration (adapted from Radarteam)

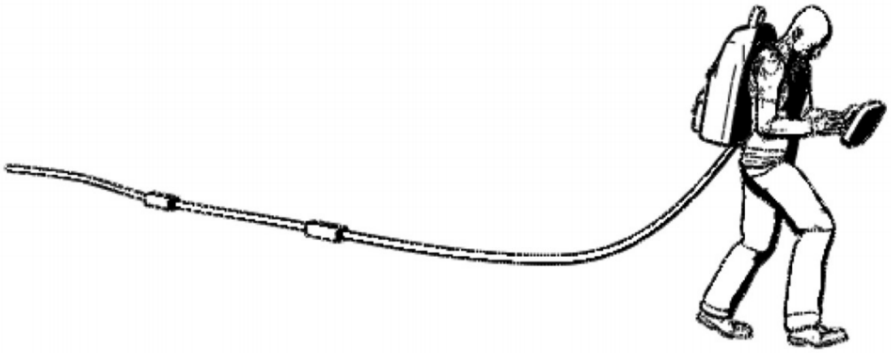

Figure 9.2 MALÅ Rough Terrain Antenna in Co-linear Model (adapted from Radarteam)

Deployment of the RTA system was mostly hands free (Figure 9.3), affording concentration on the pace of collection and avoiding obstacles. The RTA has built in transmitter and receiver electronics that communicates to a control unit using fibre optic cables that are reinforced with flexible Kevlar™ and stainless steel cable and ceramic connectors making up the nearly 10-meter-long instrument snake (Figure 9.4). The RTA system is malleable to most ground conditions, obstacles, and microtopography. The RTA was deployed across the site in various types of challenging terrain and did not require extensive trail clearing, although trail development was provided by *Pacific Northwest Tree Stewards*.

Figure 9.3 MALÅ RTA Antenna at a Sedimentary Sequence near Oyster River on Vancouver Island.

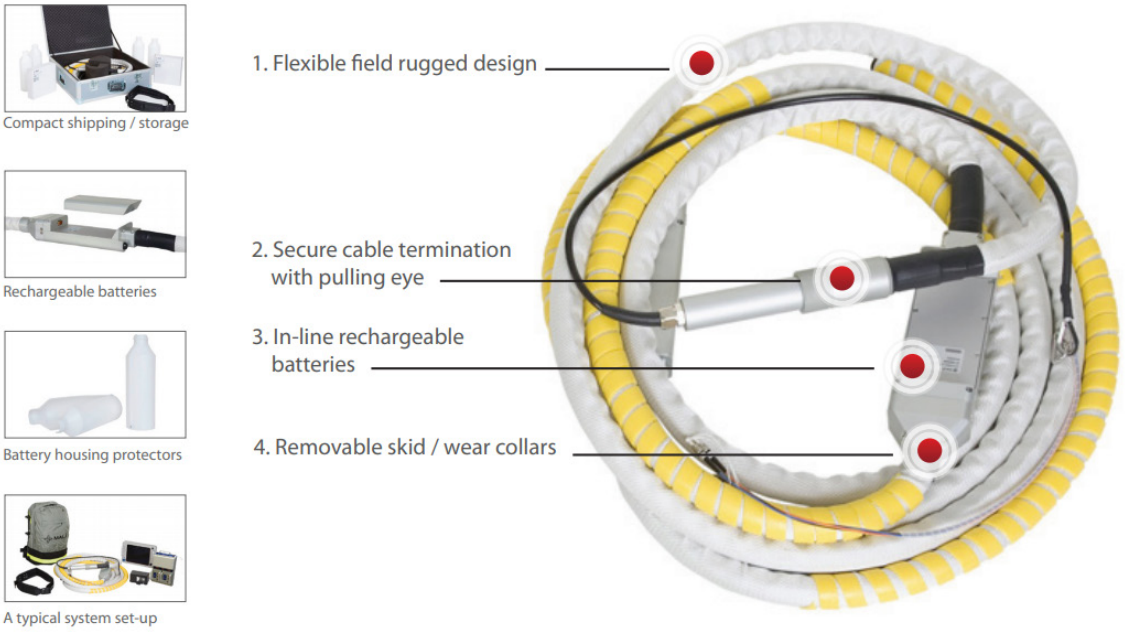

Figure 9.4 Components of MALÅ RTA Antenna (taken from MALÅ RTA specifications brochure)

Figure 9.5 MALÅ XV11 RAMAC Monitor (taken from MALÅ XV11 specifications brochure)

The RTA was connected to the MALÅ ProEx control unit, a modular controller to provide data acquisition signal and electromagnetic signal control (Figure 9.6). For this study MALÅ ProEx contained one optical module to be used in a single channel system with the RTA antenna. The MALÅ ProEx power supply is a lithium-ion 12V battery with a nominal operating time of approximately 5 hours, has an operating temperature -20° to +50° Celsius, is IP65 environmentally certified, was set to a pulse repetition frequency of 100 KHz to drive the RTA antennas at 16-bit data resolution (Figure 9.5). The MALÅ ProEx has a maximum number of samples per GPR trace of 2048 and a stacking of traces from 1 – over 30,000.

Figure 9.6 MALÅ ProEx System with Optical Module, photo by Wm.Shulba

The data was displayed and processed using the user interface, MALÅ XV11, a linux based low-powered proprietary computer with a full transreflective thin-film-transistor (TFT) colour screen that has a wide operating range to be deployed for geoscience applications connected to the MALÅ ProEx via CAT5 Ethernet cable at a communication speed of approximately 100 mbit/s (Figure 8.6). The MALÅXV meets IP67 environmental protection specifications, has an operational temperature of -20° to +50° Celsius, and the system can be operated with gloves as the only user input device is a rotary encoder. It was powered by the 12 V battery pack on the MALÅ ProEx system. System testing over the first several days of data acquisition defined the system collection parameters listed in (Table 9.1). 34 GPR lines were successfully collected over a two-day data acquisition campaign.

Table 9.1 MALÅ RTA 50 GPR Deployment Specifications

Parameter	**Value**	**Unit**
Sampling Frequency	500	KHz
Sample rate	512	samples/second
Frequency Steps	82	Steps
Antenna Separation	4.2	M
Time Window	1024	Ns
Stacks	2-8	Stacks
Stacking Time	0.01	seconds
Velocity	50	metres / millisecond
Trace Density	1000	Traces / meter
Acquisition Mode	Wheel	-
Wheel Type	Hip Chain	-
Point Interval for distance encoding	0.1	m

Electromagnetic Noise and the MALÅ High Dynamic Range Antenna System

Noise is a considerable influence in GPR acquisition. Noise is electromagnetic signals that interact with transmitter and receiver devices of GPR systems that are of similar electromagnetic spectrum. Coherent noise is a predictable, yet difficult to minimize, type of noise that is internal to GPR electronic circuitry and resonant frequencies that occur in the instrument materials. GPR manufactures have been striving to address coherent noise by evolving sensor technology and materials engineering to lower front-end noise.

External noise in the same electromagnetic bandwidth as GRP from radio stations, mobile phones, Global Positioning Devices (GPS) devices, and industrial machinery are the greatest challenge for GPR acquisition. GPR systems lower noise by increasing a process called stacking which is an averaging of repeated GPR signals. Stacking reduces noise by the square root of the number of stacks, which requires fast response times by the GPR antennas, computer controller, visualizer, and data storage media. Modern digital GPR systems can facilitate several hundred to several thousand stacks (Figure 9.7).

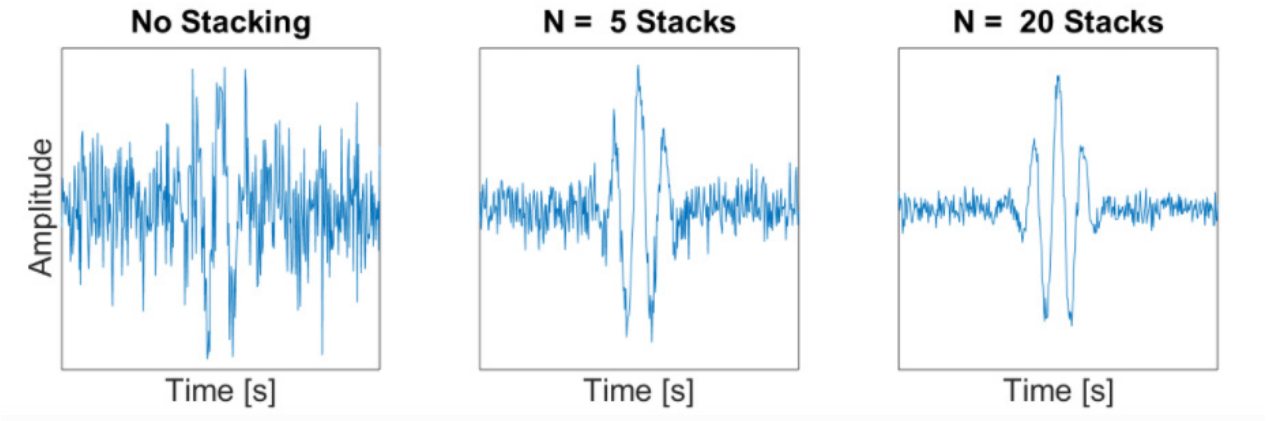

Figure 9.7 Example of stacking to improve GPR signal where increasing in the amount of stacks (N=5, N=20) increase the resolution of the stongest signal which is the desired reflector. (Adapted from http://geosci.xyz)

The use of high-dynamic range (HDR) antennas is one way to address noise through real time sampling techniques, which has appeared on more recent GPR-instrumentation. High dynamic range antennas produces real time radargrams with dynamic ranges of over 100dB, more than 16-bit. Post-processing visualization is usually in 16 or 32-bit, therefore the collection of information at these bit levels assist in SNR and bandpass filtering. Modern HDR antennas can collect data low frequency GPR at higher sampling rates that allows for increase of acquisition speeds. The MALÅ GeoDrone80 was developed in partnership with the United States Geological Survey where the HRD antenna can be carried by an Unmanned Aerial Vehicle (UAV), which would be a good fit for complex terrain assessment like peatlands, river valleys, and geohazards.

9.2 Appendix B: GSSI Subecho40 Antenna System

The Geophysical Survey Systems Inc. (GSSI) is a respected corporation known for technological advancements in the geophysical, archaeological, forensics, infrastructure, public works and transportation industries. Radarteam in Sweden developed the Subecho Antenna that integrates with the GSSI instrument ecosystem. The Subecho40 is an acrylonitrile butadiene styrene (ABS) unshielded, resistivity loaded, butterfly shaped, folded ground penetrating dipole antenna capable of monostatic or bistatic modes. The GSSI Subecho40 Antenna System was rented from Northwest Geophysics in Carnation, Washington in the winter of 2014 for this project.

Subecho40 was deployed in monostatic mode using the Geoscanners Transceiver: Model TR501 with an output voltage of 240 V and a radio frequency bandwidth of 962 MHz. The Subecho40 has a peak frequency of 55 MHz with a centre frequency of 60 MHz from an operating bandwidth of 15 – 105 MHz. The direct current resistance at the terminals is 387 Ohms. Typical depth ranges in bistatic mode is up to 70 m depth where the monostatic penetration is less at approximately up to 40 m. The vertical resolution was 0.41 m (Figure 9.2).The antenna weighs 5.0 kg. Deployment of the Subecho40 antenna was attached to a *GT Snowracer™ a*nd was pulled across the peatland using a field made harness with snowshoes (Figure 9.8).

The Subecho40 antenna was controlled using the GSSI 3000 portable single-channel GPR controller with a colour Super Video Graphics Array (SVGA) video screen to view data in real time or playback (Figure B.9). The screen was difficult to see in direct sunlight and a sunshade was made in the field using cardboard and duct tape. A *Garmin eTrex Vista™* GPS unit was connected to the GSSI 3000 via a serial port interface cable.

Table 9.2 GSSI SubEcho40 GPR Deployment Specifications

Parameter	Value	Unit
Antenna transmission rate	40	KHz
Data Collection Mode	Distance	
Sampling Resolution	512	samples / per scan
Sampling Format	16	Bit
Sampling range	60	nanoseconds
Dielectric Constant	10.00	dimensionless
Scanning Resolution	18.00	scans/trace
Scanning Rate	100	
Scan Stacking	3	
Gain Points	-10,15,25	dB
Low Pass Filter	10	MHz
High Pass Filter	80	MHz

Encoding the distance travelled down a GPR tract is essential in determining the location of each GPR scan. There was no distance encoder such as a rotary wheel encoder available for the GSSI 3000 at the time for the snowy conditions. The error of GPS data is always not appropriate for data collection of multiple traces per metre, as was the case with this study, therefore continuous data "Distance Mode" was chosen with a scanning frequency of 32 scans per second. The GPR tracts were predetermined and 20 m markers were premeasured using a nylon measuring tape. When snowshoeing past the markers a waypoint was created in the GSSI 3000. This position was triple checked with GPS measurements at the time of marking with the *Bad Elf™ Surveyor Pro+* , during the GPR collection with the integrated *Garmin eTrex Vista™,* and then again using the *Bad Elf™ Surveyor Pro+* resulting in a final horizontal resolution of approximately 1 m radius. The GPR scans x,y coordinates were estimated using timestamps and x, y coordinates waypoints to determine the horizontal velocity of acquisition via snowshoes. In most cases continuous velocity was consistent and within 10% variable change.

Unfortunately, due to using the Subecho40 in monostatic mode; the gain setting on the antenna were too aggressive and created a strong frequency harmonic in the transceiver. The majority of signal collection was noise with the exception of the strongest reflector at the bottom of the peatland at the substratum interface in some locations of the peatland. This was moderately successful, however the deepest regions of the peatland did not return a reflection and often when returned the reflection was very faint (Figure 9.10).

Figure 9.8 GSSI Subecho40 antenna with GTSnoracer™

Figure 9.9 GSSI 3000 Controller with Subecho40 GPR Antenna

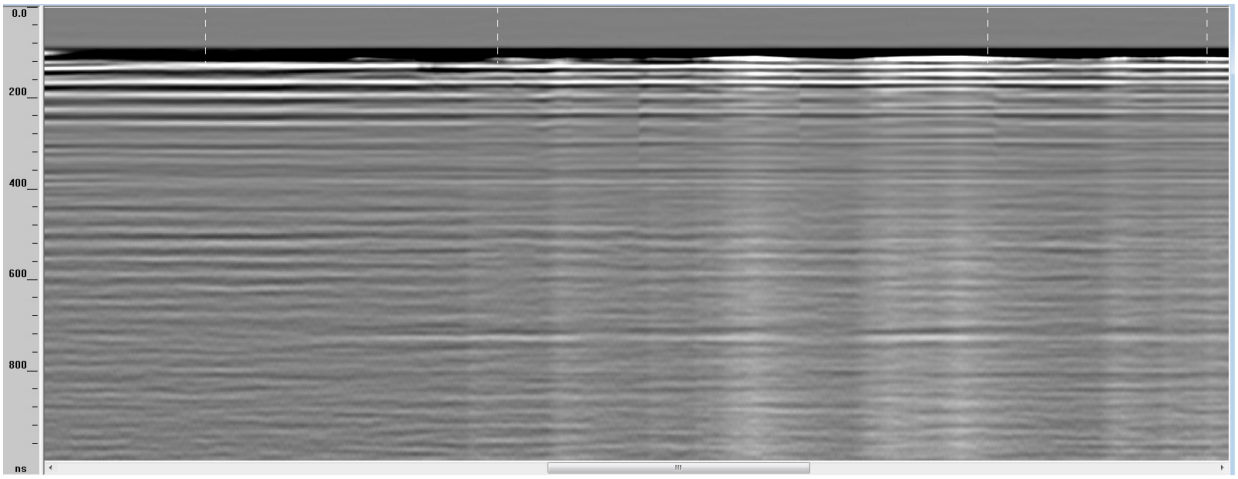

Figure 9.10 Example of Noisy GSSI GPR Data

9.3 Appendix C: Frequency-and-Time-Domain Signal Processing Modified Method

As the GPR radiowave signal propagates through the subsurface it is distorted as a result of the electromagnetic characteristics of the host medium. To have some correct estimation of the accuracy of the interpretation of GPR, some elements of the host medium needs to be identified. Lithological material, chemical composition, water content, porosity, and mineralogy interact with and attenuate the GPR signal. Drive-point piezometers were used to identify depth of peat in discrete locations that were then used to calibrate GPR signals at those locations. This calibration was essential to ensure that estimates of GPR signal velocity from existing peatland research in other regions of the boreal were consistent with the study area. Estimates of GPR velocity were based on previous peatland GPR investigations (Dallaire & Garneau, 2008; Van Bellen et al., 2011) estimated at 0.05 m per nanosecond. Where subsurface electromagnetic properties change abruptly, like at the interface of the peatland and underlying glacial till, GPR signals reflect and/or refract.

The modelling process for the acquired data with MALÅ RTA was completed in MALÅ RadExplorer. The processing steps are summarized in this section. Data are input into the *RadExplorer* by uploading raw GPR data in .rad file format directly from the MALÅ XV11. When a .rad file is selected an inspection of the length and traces is identified. For example, DAT_0118 was 175.6 m with 1750 traces, equating to 10 traces per meter.

Once inputted into the *RadExplorer*, a workflow can be applied to the GPR data. Workflows were batch applied to each GPR dataset for consistency in processing (Figure 9.11). Elements of the GPR processing workflow are known as routine modules. The modules in *RadExplorer* run in series and each module that follows in influenced by the prior. This research used a modified method of frequency-and-time-domain signal processing to increase the detection of reflective surfaces with weak contrast. The resulting output is a vertical two-dimensional cross-section *radargram*, that has length of the profile along the horizontal axis and the y-axis in depth.

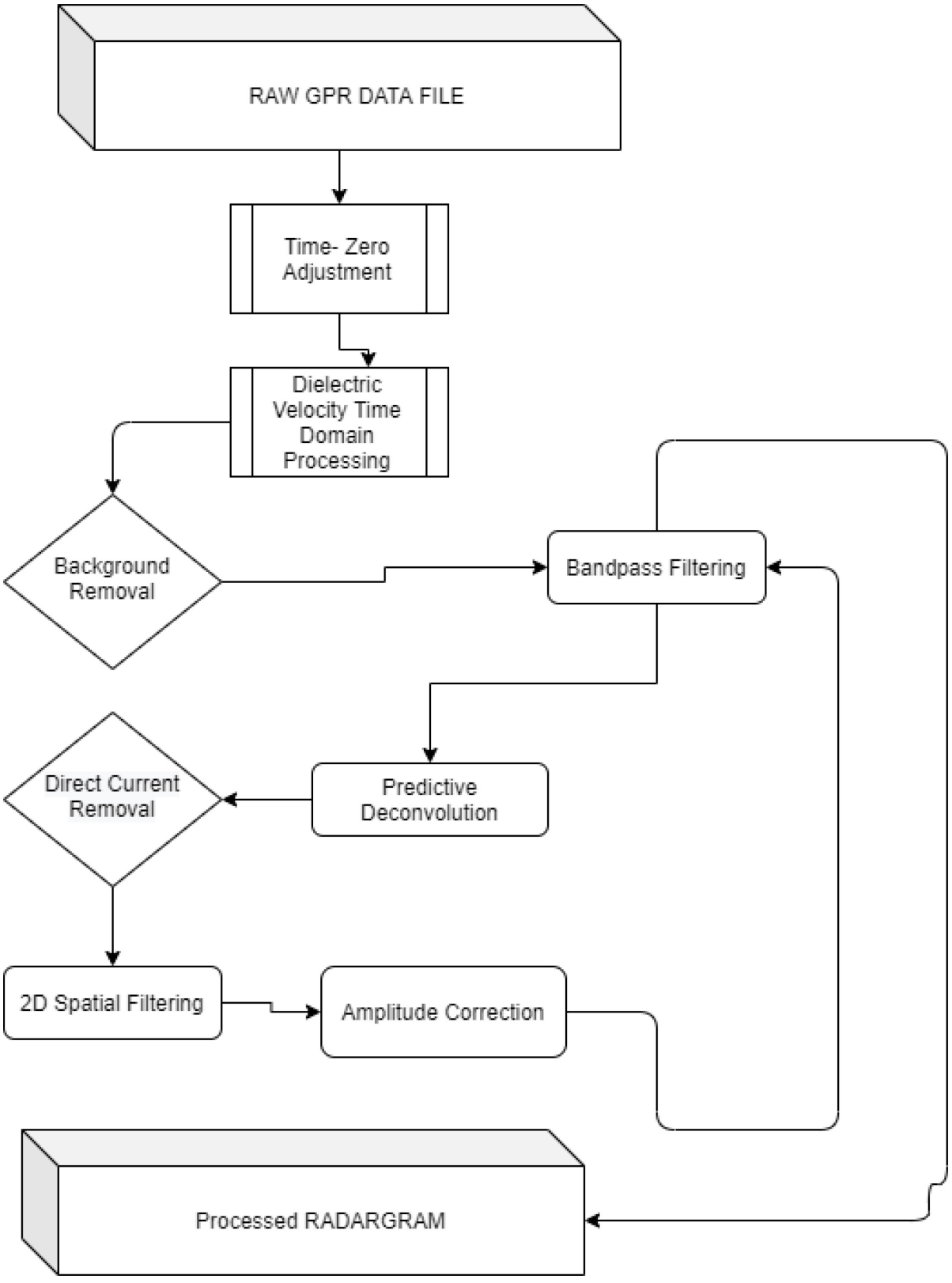

Figure 9.11 *RadExplorer workflow diagram for processing GPR radargram*

Background Removal

During GPR collection the most prominent signal that arrives at the receiving antenna is the direct wave from the transmitting antenna, known as the direct wave. In addition to the direct wave, there are other noise sources that may cloud the desired signal. The background removal technique in the *RadExplorer* attempts to remove noise and direct waves from the trace in a set time-domain using a subtractive technique. A weak background removal setting results in a wide time window and strong background removal setting results in a small time window. The setting in this project was set to slightly higher than normal at 70%.

Bandpass Processing

Signal to noise ratio (SNR) is a significant component of GPR processing and interpretation. Bandpass filtering is used to increase the SNR by setting a low cut, low pass, high cut, and high pass settings in a trapeziform zero-phase bandpass filter. This is similar to filtering techniques utilized in audio synthesis. Bandpass setting for the data processing were set to 4 MHz, 61 MHz, 64 MHz, and 112 MHz for low cut, low pass, high cut, and high pass respectively, creating a symmetrical histogram frequency envelope centred around approximately 60 MHz. Traditionally it is suggested that bandpass filtering to occur following many of the routine modules. In this case light bandpass filtering was placed early in the processing train following background removal due to the intention of strongly defining the strongest reflector. A second bandpass filter was applied following the modules routine to remove artefact of processing.

Direct Current Shift Removal

The GPR receiving antenna collects data prior to transmission and the resulting trace can be shifted off of baseline. This shift can be represented in positive or negative amplitude voltage which is only a small percentage of the overall GPR trace. This “time-zero” offset can estimate the direct current coming from the original analogue signal or from imperfections in the analogue to digital converters. This module is time dependent yet the entire time domain was selected.

Predictive Deconvolution

Deconvolution is a filtering technique that shapes repeating signals into a primary, not repeating signal by supressing multiple reflections to increase resulting resolution of the scan by altering the spectrum (Figure 9.12). The predictive component of deconvolution is to estimate and then remove predictable parts of the seismic trace, typically multiples of the original signal. By altering the amplitude of the wavelets, the resolution of the strongest wavelet is increased and presence of the multiples is decreased. This routine module is very important in subsurface environments with significant amounts of attenuation and absorption. Since radar is greatly attenuated by saturated media, like peatlands, the role of deconvolution is significant, and is enhanced from significant bandpass filtering. The module was applied across the entire time-domain of the scanning window. The prediction gap which refers to the compression rate of wavelets was set to 81.9 which is considered very high. The deconvolution operator length sets the maximum delay value of autocorrelation was set to 142. This is considered to be a lower value to filter multiple reflections and antenna reverberation. The final parameter is the white noise level which is a predictive stabilizing parameter, which has a subtle effect on the routine; however, when pushed to extreme values (6.69), the amount of resulting background noise was significantly decreased in the scanning window.

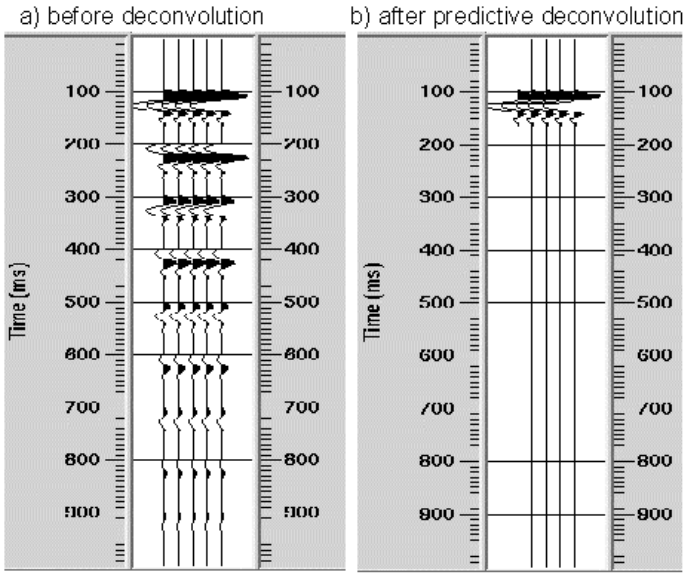

Figure 9.12 Deconvolution filtering example (from xsgeo.com)

2D Spatial Filtering

Two-dimensional spatial filtering can perform many different styles of filtering to address individual samples within a trace. The filter type used was “Alpha-trimmed Mean” with a rejection percentage of 100%, with a filter size of 3 traces that defined the width of the operator of the spatial filter and one sample that defined the height of the operator. Operating in normal filter mode; the samples in the centre of the operator were calculated with a mean value. This algorithm sorted samples and averaged the range of the values to cull samples that were beyond the bounds of the averages and smoothing the other samples. Setting the rejection percentage to 100% returned values of the median filter which increased resolution of the peatland-substratum reflector.

Zero-Time Adjustment

Since the MALÅ RTA antennas are unshielded, the data collection is omnidirectional and the “listening window” may begin prior to the transmission; therefore, an adjustment to the GPR data is needed to identify the moment when the transmitting wave leaves the emitting antenna. The zero-time adjustment first-arrival time in nanoseconds can be set to the direct wave that defines the first movement of the emitting wave. This can be precisely calculated by the distance of the transmission antenna to the receiving antenna. The direct-wave detection can be sensed at different times depending on the listening domain of the receiving antenna, antenna separation (4.2 m), and direct wave adjustment velocity (30 cm/ns or approximately 300,000,000 m /sec).

Amplitude Correction

To control transient signals, subsurface signal reverberation, and other quasi-harmonic oscillations that follow the signal path of the GPR; an amplitude correction can be undertaken (Chernokalov et al., 2000). The automatic gain control in *RadExplorer* automatically equalizes amplitudes in every signal trace in the GPR running window by calculating the arithmetical amplitude mean and dividing every signal value in the window. This module functions similar to compression in audio engineering.

There are three scalar applications where the gain control is applied: *centred* applies to the central sample, *trailing* applies to the last sample, and *leading* applies to the first sample in every running window. Leading was used for gain control in this project. Another element of this module is called trace equalization that is used for averaging amplitude variations from trace to trace. All traces were normalized to the arithmetic mean amplitude in the running window of each GPR line. Amplitude correction often increases the contrast of the radargram (Figure 9.13). In this workflow, the amplitude correction was effectively implemented to compliment bandpass filtering that increased reflection resolution above the main reflector and filtered out most noise and double reflection responses.

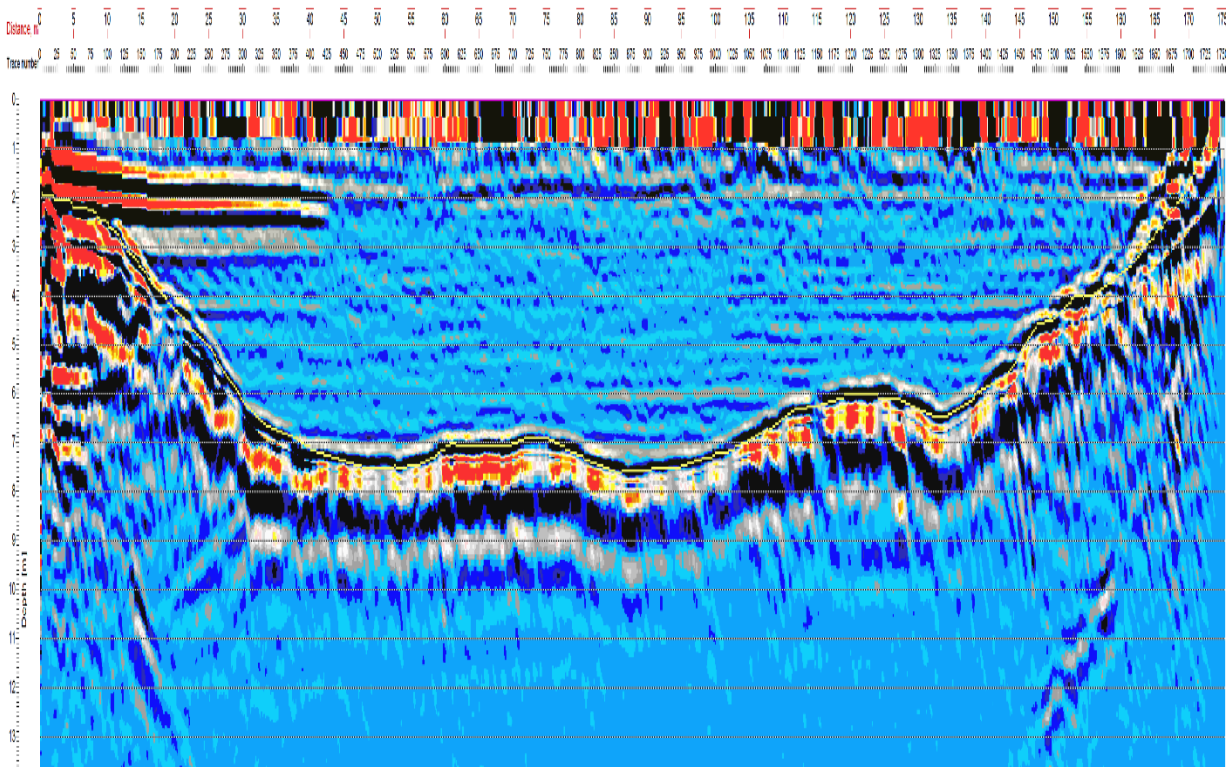

Figure 9.13 Radargram from GPR Line DAT_0118

9.4 Appendix D: Piezometer and Water Table Well Details

Table 9.3 Drive-point piezometer collar information and depth.

LOCATION	NORTHING	EASTING	GROUND ELEVATION (mASL)	MAX DEPTH (mBGL)
MLP01	431616.9	6195448	701	2.12
MLP02	431616.3	6195406	703.06	4.32
MLP03	431619.7	6195347	699.45	2.81
MLP04	431616.1	6195274	699.08	4.86
MLP05	431616.1	6195120	699.13	7.05
MLP06	431680.6	6194968	699.1	2.22
MLP07	431729.5	6194935	701.21	4.44
MLP08	431589.3	6194849	699.25	2.94
MLP09	431580.1	6194897	699.13	3.28
MLP10	431503.3	6194986	699.29	7.78
MLP11	431438.2	6195104	699.09	7.79
MLP12	431483.1	6195253	699.04	3.54
MLP13	431473.9	6195303	699.28	3.12
MLP14	431472	6195380	700.78	2.21
MLP15	431824.7	6195136	698.97	7.63
MLP16	431843.4	6195252	698.78	7.1
MLP17	431867	6195323	698.79	4.9
MLP18	431777.6	6195283	698.96	5.04
MLP19	431651.5	6195062	699.08	3.94

Table 9.4 Lithological Depths at each drive-point piezometer location.

Location	Top (mBGL)	Bottom (mBGL)	Lithology	Location	Top (mBGL)	Bottom (mBGL)	Lithology
MLP01	0.8	2.12	UPLAND	MLP11	4.74	7.79	PEAT-D
MLP01	0	0.8	UPLAND	MLP11	1.83	4.74	PEAT-B
MLP02	1.35	4.32	UPLAND	MLP11	0	1.83	PEAT-A
MLP02	0	1.35	UPLAND	MLP12	1.87	3.54	PEAT-B
MLP03	1.12	2.81	UPLAND	MLP12	0	1.87	PEAT-A
MLP03	0	1.12	UPLAND	MLP13	1.28	3.12	UPLAND
MLP04	2.79	4.86	PEAT-C	MLP13	0	1.28	UPLAND
MLP04	1.58	2.79	PEAT-B	MLP14	0.91	2.21	UPLAND
MLP04	0	1.58	PEAT-A	MLP14	0	0.91	UPLAND
MLP05	4.57	7.05	PEAT-D	MLP15	3.68	7.63	PEAT-D
MLP05	3.02	4.57	PEAT-C	MLP15	1.44	3.68	PEAT-B
MLP05	1.61	3.02	PEAT-B	MLP15	0	1.44	PEAT-A
MLP05	0	1.61	PEAT-A	MLP16	3.17	7.1	PEAT-D
MLP06	1.45	2.22	UPLAND	MLP16	1.6	3.17	PEAT-B
MLP06	0	1.45	UPLAND	MLP16	0	1.6	PEAT-A
MLP07	1.66	4.44	UPLAND	MLP17	2.5	4.9	PEAT-C
MLP07	0	1.66	UPLAND	MLP17	1.16	2.5	PEAT-B
MLP08	1.75	2.94	PEAT-B	MLP17	0	1.16	PEAT-A
MLP08	0	1.75	PEAT-A	MLP18	3	5.04	PEAT-C
MLP09	1.39	3.28	PEAT-B	MLP18	1.74	3	PEAT-B
MLP09	0	1.39	PEAT-A	MLP18	0	1.74	PEAT-A
MLP10	3.48	7.78	PEAT-D	MLP19	1.35	3.94	PEAT-B
MLP10	1.69	3.48	PEAT-B	MLP19	0	1.35	PEAT-A
MLP10	0	1.69	PEAT-A				

Table 9.5 Water-Table monitoring wells vegetation and location.

ID	Vegetation	Latitude	Longitude
MLA	Fen	55.8982300	-112.0964300
MLB	Fen	55.8970800	-112.0965000
MLC	Bog	55.8961400	-112.0971800
MLD	Fen	55.8982500	-112.0935400
MLE	Fen	55.8978100	-112.0913500
MLF	Bog	55.8951300	-112.0951900
MLG	Fen	55.8985900	-112.0896500
MLH	Fen	55.8973000	-112.0934500
MLM	Bog	55.8979200	-112.0900000
MLN	Fen	55.8969000	-112.0917800
MLO	Bog	55.8954800	-112.0953100
MLP	Bog	55.8949400	-112.0947000
MLQ	Fen	55.8974600	-112.0915100
MLR	Fen	55.8965100	-112.0917100
MLS	Fen	55.8961800	-112.0930300
MLT	Bog	55.8959200	-112.0946900
MLU	Fen	55.8958300	-112.0925100
MLV	Bog	55.8955000	-112.0939500

9.5 Appendix E: Peatland Geochemical Volume Analysis

Table 9.6 Numeric model summary statistics of DOC and DIC in peatland volumes

DOC Interval Concentration (mg/l)	Interval Volume (m3)	DOC Volumetric Mass at 90% porosity (Kg)	DIC Interval Concentration (mg/l)	Interval Volume (m3)	DIC Volumetric Mass at 90% porosity (Kg)
< 7.15	0.00	0.00	< 86.13	1021640.76	79194.52694
7.15-10.0	161.37	1.25	86.13-100.0	256931.81	21520.22291
10.0-15.0	630.46	7.09	100.0-120.0	279734.85	27693.75039
15.0-20.0	246.04	3.88	120.0-150.0	327175.17	39751.7832
20.0-25.0	433.40	8.78	150.0-200.0	555218.28	87446.87905
25.0-30.0	1716.16	42.47	200.0-230.0	304957.18	59009.21399
30.0-35.0	13474.32	394.12	230.0-250.0	163510.96	35318.36658
35.0-40.0	21139.32	713.45	250.0-300.0	228974.77	56671.25505
40.0-45.0	25090.84	959.72	300.0-350.0	192544.66	56319.31337
45.0-50.0	34232.83	1463.45	350.0-400.0	209657.66	70759.45956
50.0-55.0	171029.54	8081.15	400.0-420.0	76304.33	28156.29954
55.0-60.0	880961.54	45589.76	420.0-450.0	69265.02	27117.25664
60.0-65.0	1533165.13	86240.54	450.0-500.0	53526.87	22882.7373
65.0-70.0	453473.59	27548.52	500.0-550.0	42952.14	20294.88798
70.0-75.0	377627.19	24640.17	550.0-600.0	49724.02	25732.18262
75.0-80.0	145023.81	10115.41	600.0-650.0	61666.31	34687.2984
80.0-85.0	157528.79	11696.51	650.0-700.0	33377.12	20276.59976
85.0-90.0	71734.47	5649.09	700.0-750.0	7789.16	5082.426484
> 90.0	47282.28	3829.86	> 750.0	0.00	0
Total	3934951.08	226985.23	Total	3934951.08	717914.4598

Table 9.7 Numeric model summary statistics of NH4 and TKN in peatland volumes

NH4 Interval Concentration (mg/l)	Interval Volume (m3)	NH4 Volumetric Mass at 90% porosity (Kg)	TKN Interval Concentration (mg/l)	Interval Volume (m3)	TKN Volumetric Mass at 90% porosity (Kg)
< 0.0	634759.26	57.13	< 0.5	202170.35	90.98
0.0-0.5	317451.11	71.43	0.5-1.0	63513.20	42.87
0.5-1.0	300258.02	202.67	1.0-1.5	116593.09	131.17
1.0-1.5	264712.17	297.80	1.5-2.0	176724.55	278.34
1.5-2.0	236492.39	372.48	2.0-2.5	241192.55	488.41
2.0-2.5	225956.25	457.56	2.5-3.0	281672.18	697.14
2.5-3.0	231543.82	573.07	3.0-3.5	287207.31	840.08
3.0-3.5	262146.37	766.78	3.5-4.0	276314.60	932.56
3.5-4.0	282411.21	953.14	4.0-4.5	252200.19	964.67
4.0-4.5	245438.62	938.80	4.5-5.0	242062.92	1034.82
4.5-5.0	191024.51	816.63	5.0-5.5	235572.40	1113.08
5.0-5.5	146100.58	690.33	5.5-6.0	199553.73	1032.69
5.5-6.0	77267.85	399.86	6.0-6.5	177736.90	999.77
6.0-6.5	61944.69	348.44	6.5-7.0	207308.69	1259.40
6.5-10.0	312680.01	2251.30	7.0-7.5	186520.57	1217.05
10.0-15.0	133375.21	1500.47	7.5-8.0	210409.31	1467.60
15.0-20.0	10568.31	166.45	8.0-8.5	174209.93	1293.51
20.0-25.0	812.23	16.45	8.5-9.0	158878.93	1251.17
> 25.0	8.48	0.19	9.0-9.5	115362.96	960.40
			9.5-10.0	65920.92	578.46
			> 10.0	63825.78813	574.43
Total	3934951.08	10880.97	Total	3934951.08	17248.60

9.6 Appendix F: Ground Penetrating Radargrams

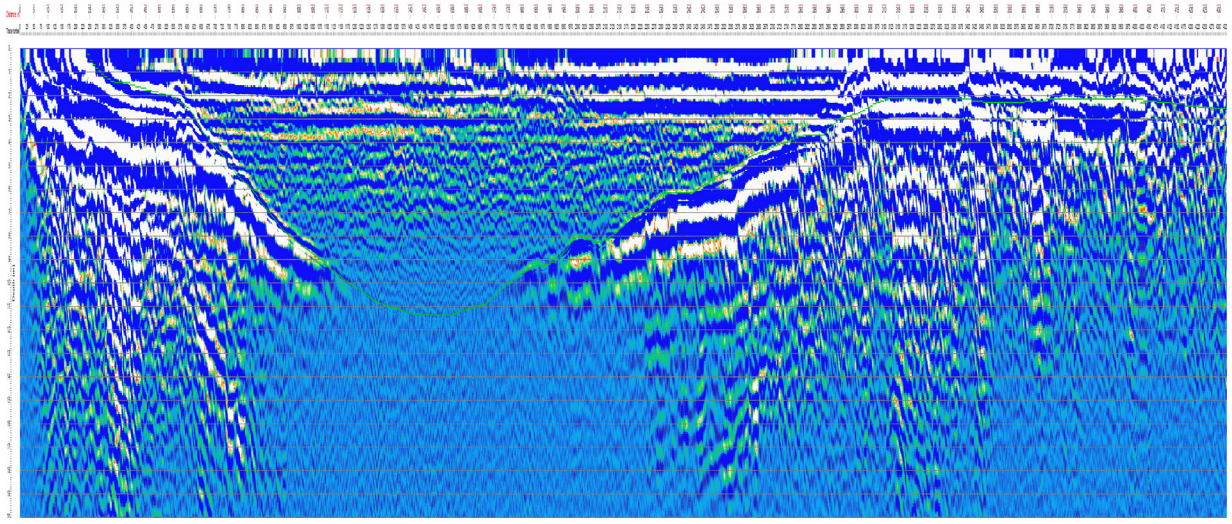

Figure 9.14 GPR Radargram: 0102

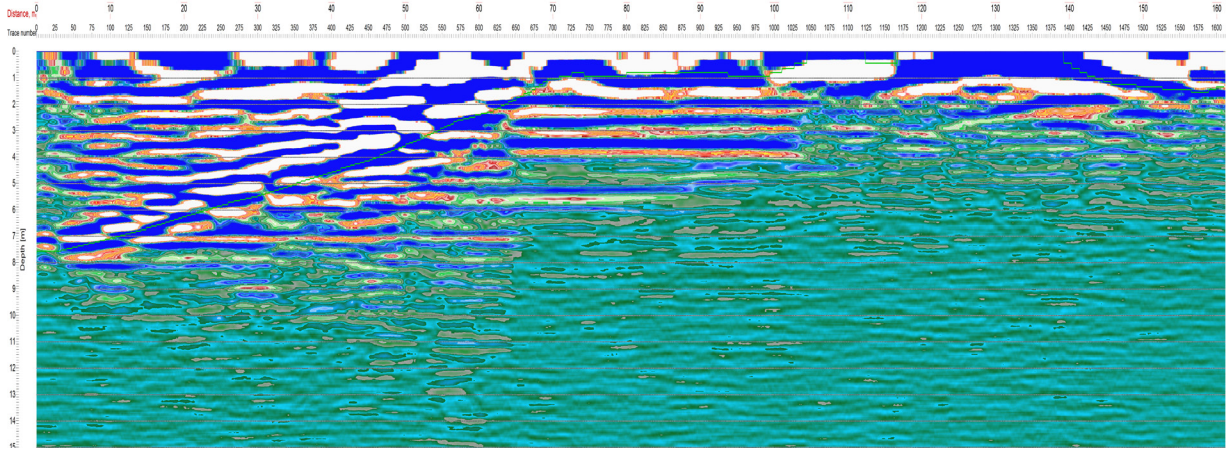

Figure 9.15 GPR Radargram: 0103

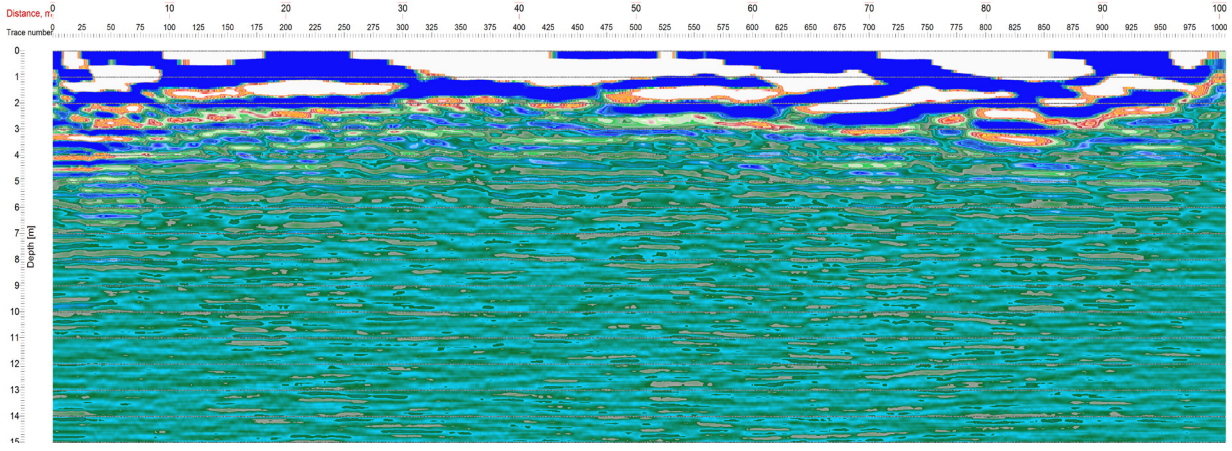

Figure 9.16 GPR Radargram: 0104

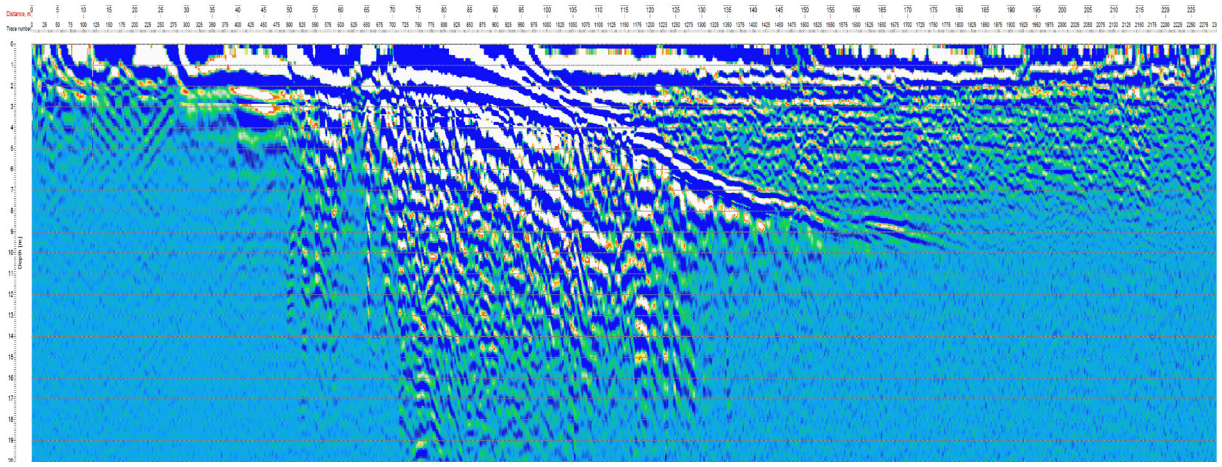

Figure 9.17 GPR Radargram: 0105

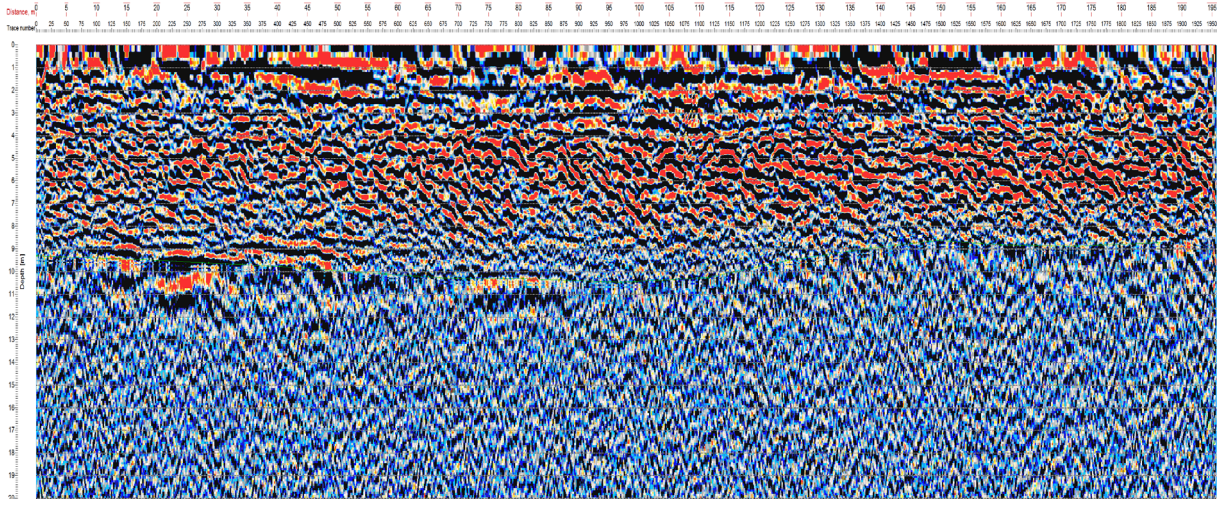

Figure 9.18 GPR Radargram: 0106

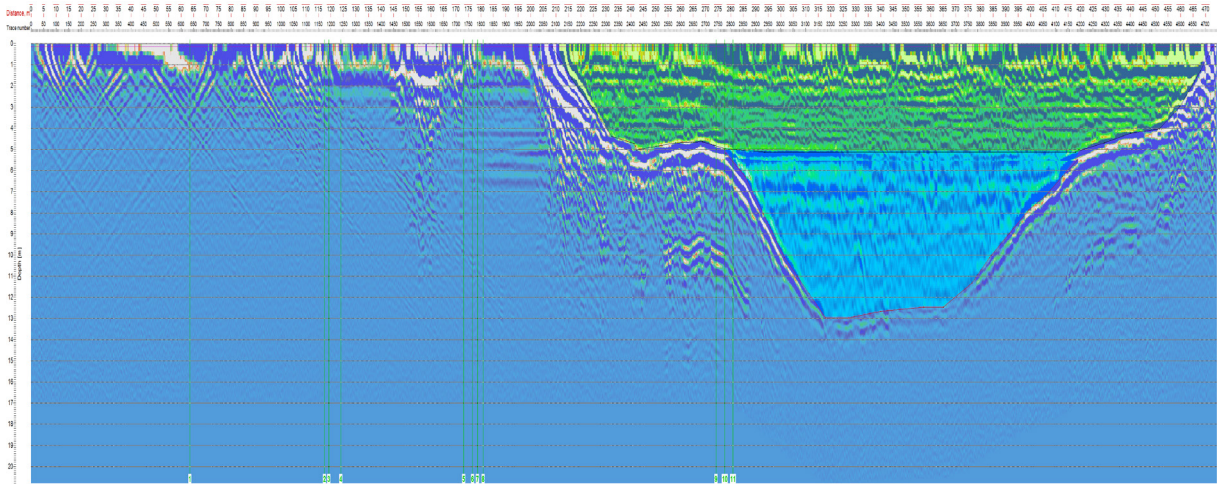

Figure 9.19 GPR Radargram: 0111

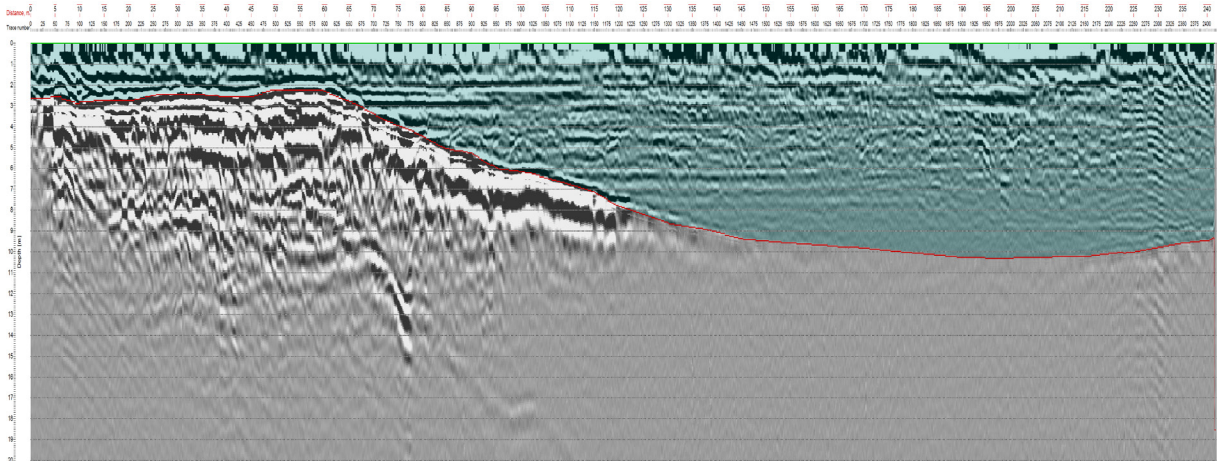

Figure 9.20 GPR Radargram: 0112

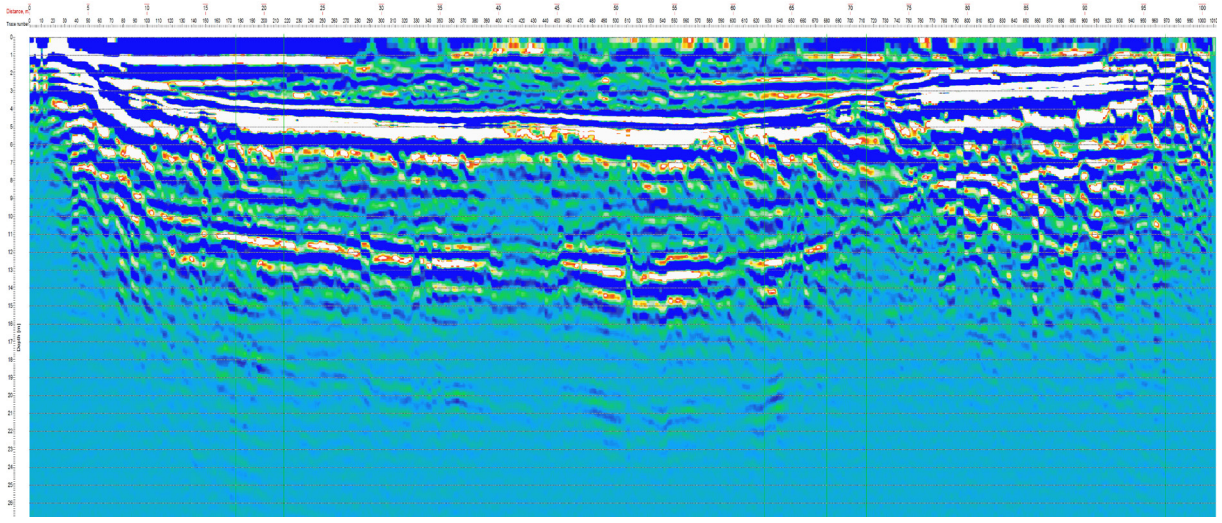

Figure 9.21 GPR Radargram: 0117

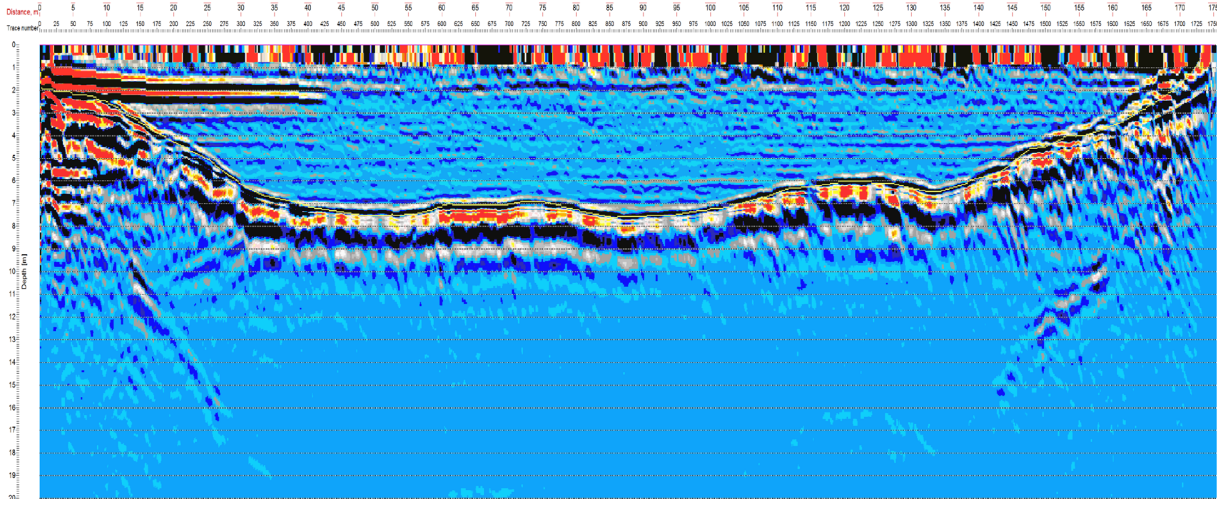

Figure 9.22 GPR Radargram: 0118

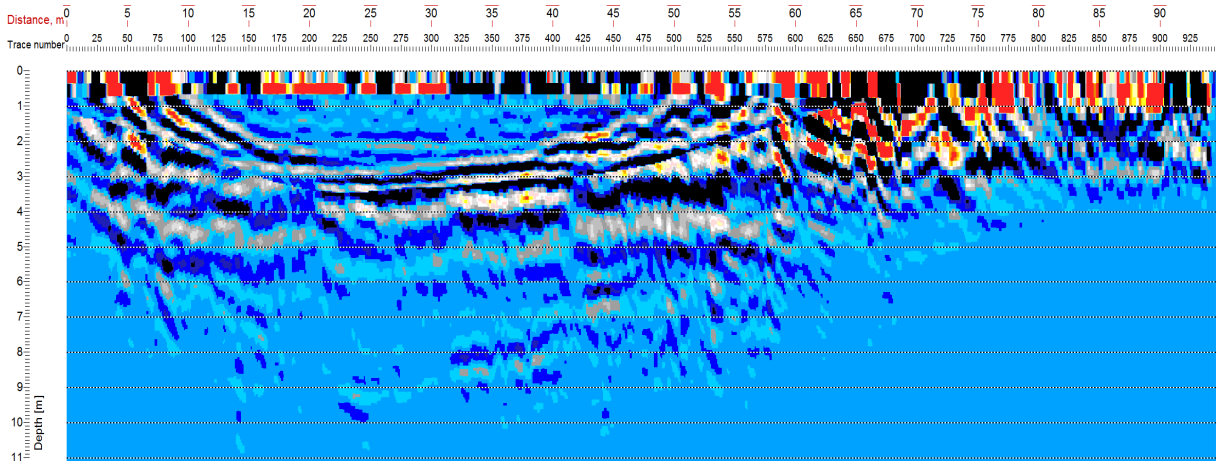

Figure 9.23 GPR Radargram: 0120

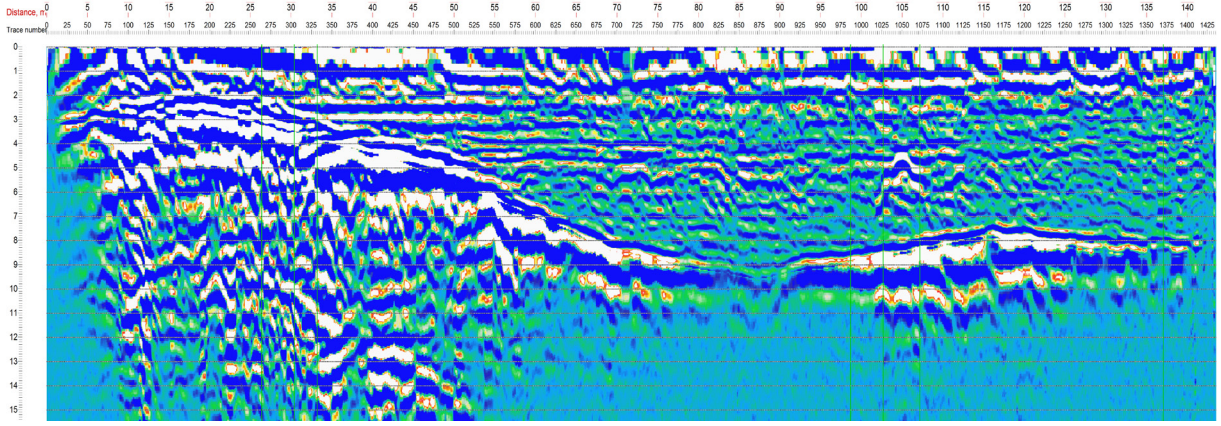

Figure 9.24 GPR Radargram: 0122

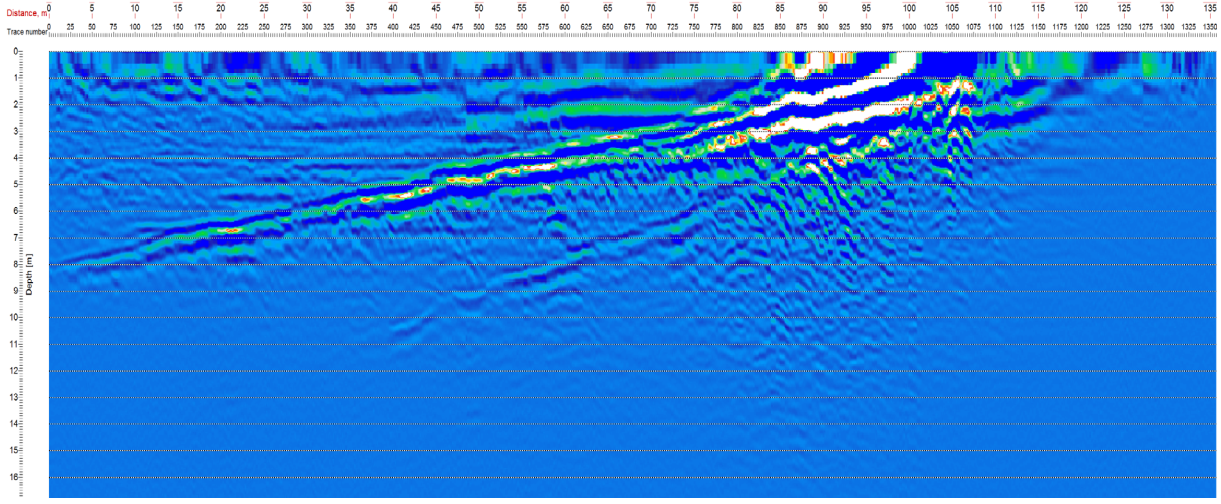

Figure 9.25 GPR Radargram: 0123

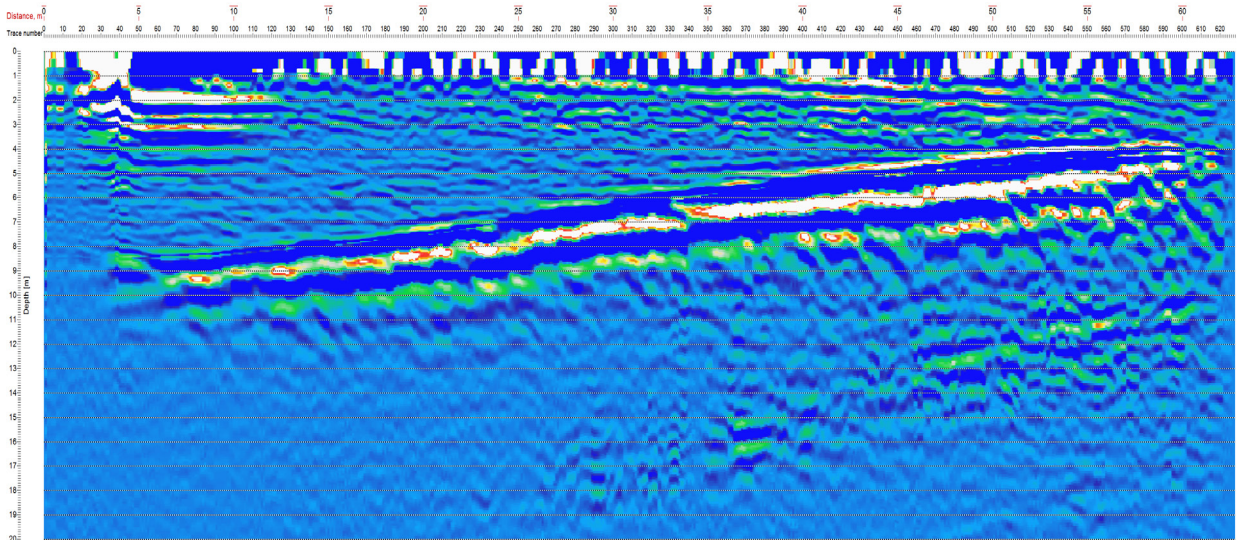

Figure 9.26 GPR Radargram: 0125

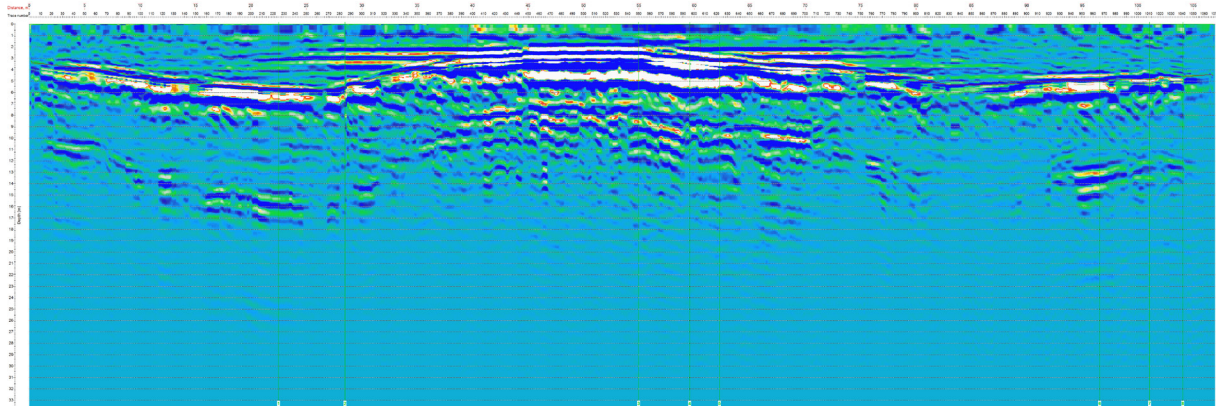

Figure 9.27 GPR Radargram: 0126

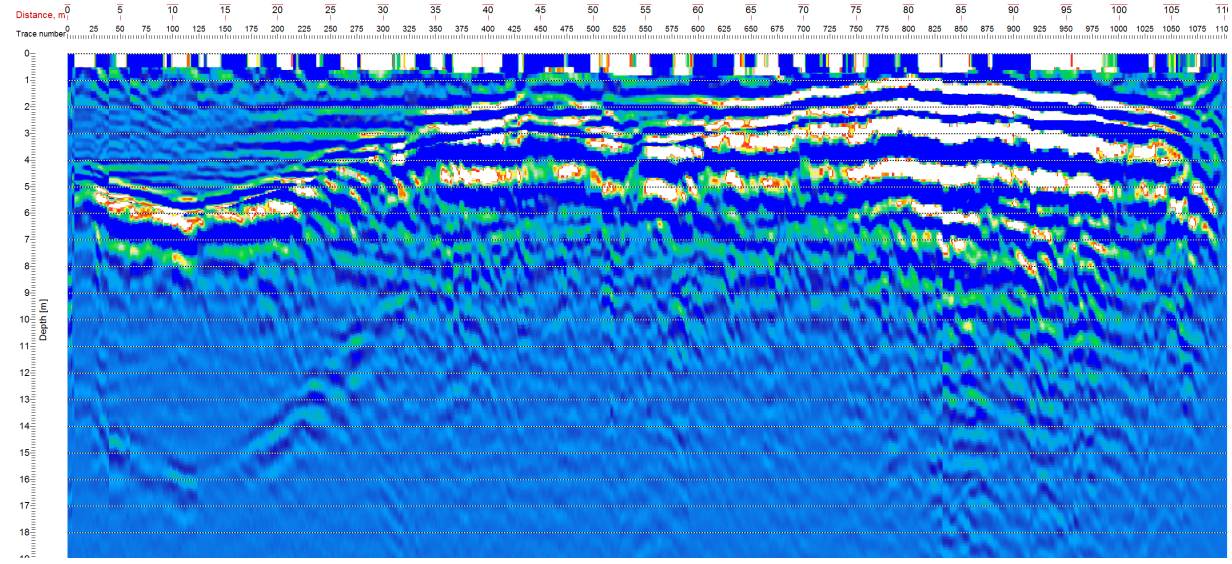

Figure 9.28 GPR Radargram: 0127

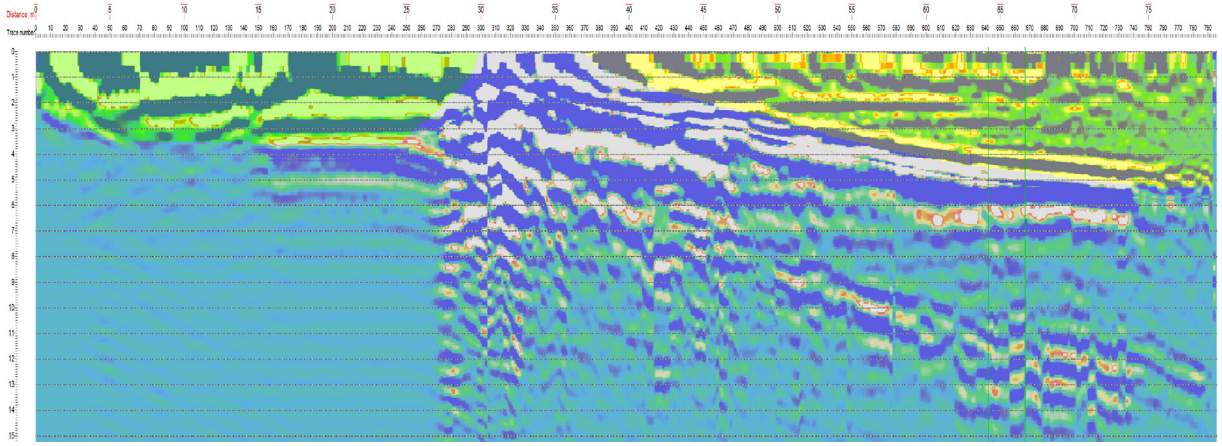

Figure 9.29 GPR Radargram: 0128

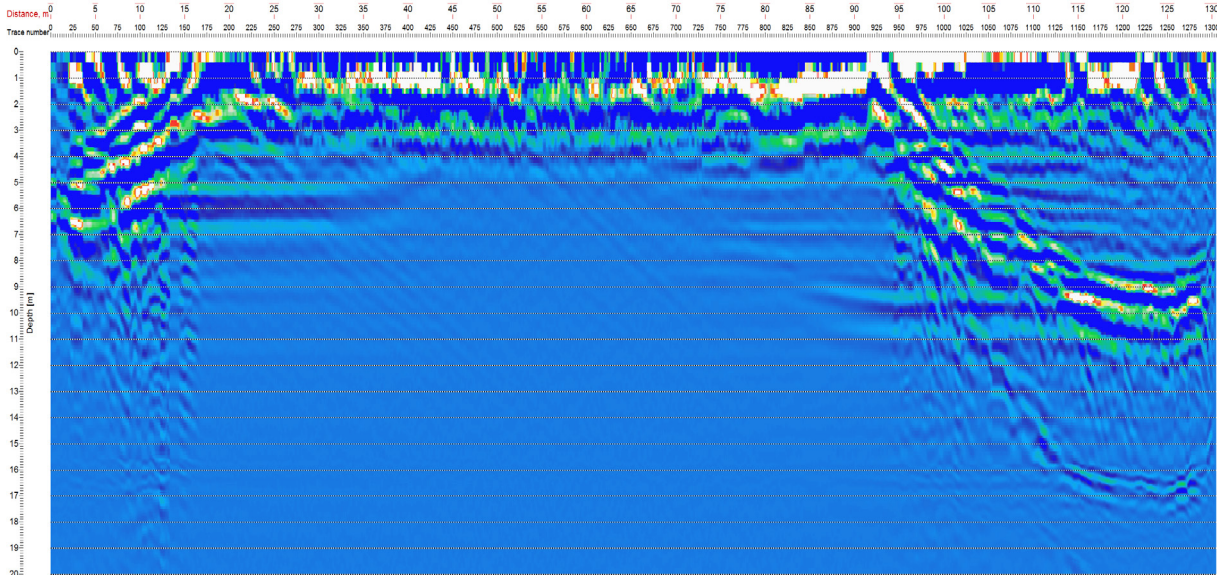

Figure 9.30 GPR Radargram: 0129